DESIGN, MODELING, AND CONTROL OF A NOVEL MULTIROTOR UAV WITH EMBEDDED 3D-PRINTED THRUST FORCE SENSOR

E.B. (Bernard) Prakken

MSC ASSIGNMENT

Committee:
A. Franchi, Ph.D HDR
ir. Q.L.G. Sablé
Y.A.L.A. Aboudorra, MSc
prof. dr. ir. G.J.M. Krijnen
dr. ir. D. Alveringh

February, 2022

009RaM2022
Robotics and Mechatronics
EEMathCS
University of Twente
P.O. Box 217
7500 AE Enschede
The Netherlands

Abstract

When simulating an Unmanned Aerial Vehicle (or UAV), the thrust force of the propellers is often seen as the input of the system to have an effect on the system states: the position and the orientation of the vehicle. However, the actual input that a multirotor control can have on the system is the rotor velocity. The resulting thrust generated by the rotor velocity is also dependent on factors like the air-density, malfunctions and whether there are objects or surfaces near the propeller.

In this research the implementation of strain gauges in a multirotor UAV is explored. These strain gauges are used to design a sensor that is implemented in the arms of a multirotor. The sensors measure the strain in the arms which is produced by the thrust of its associated propeller. However, this strain is coherent with deflection that the thrust force introduces, which is an unwanted effect in most aerial vehicles and especially in multirotors. Flexibility can cause unwanted vibrations and can lead to an uncontrollable system. This thesis goes into the consequences of flexibility in multirotor UAVs and discusses how the thrust can be measured under the influence of the UAV dynamics. A 2D UAV model has been used to analyse the elastic behaviour in the arms of the multirotor. Furthermore, it discusses the characteristics and the performance of the 3D printed sensor that has been designed and implemented for this application.

Acknowledgement

I would like to thank my committee for their continued support and encouragement throughout this assignment. Foremost, I would Prof. Antonio Franchi and Prof. Gijs Krijnen for giving me the opportunity to combine the knowledge of the Aerial-CORE project and the NIFTy group. Their intelligence, motivation and enthusiasm on the project have helped me to overcome multiple obstacles that I encountered throughout this thesis.

Furthermore I would like to thank Youssef Aboudorra and Quentin Sable for supervising me on a daily basis. I am intensely grateful that you took on the job of guiding me through this project, even though the solutions were not always at hand. Your insights and patients with me have helped to take the steps towards graduation.

A special thanks to Dennis Alverigh to be a part of my graduation committee.

At last I would also like to say thanks to Martijn Schouten, who helped me during the 3D-printing process even though he was not assigned to be my supervisor.

Contents

List of Tables

List of Figures

1 Introduction

1.1 Motivation

In recent years the development in Unmanned Aerial Vehicles, or UAVs, has increased significantly. Especially when it comes to multirotors. This type of UAV utilizes propellers to produce thrust and are often configured in a point-symmetrical structure. While the commercial multirotor market is already well established in cinematics (DJI) , there are a lot of applications for multirotor UAVs that have yet to be explored.An example of which is the use of multirotor UAVs for physical interactions (43)(26). This is also the case when it comes to the sensors that the multirotor embodies. This research will be focused specifically on a thrust sensor. The amount of thrust that each propeller produces is often empirically determined throughout the specifications of the propeller and the linked electric motor. Doing so, the amount of thrust is estimated either by a rough aerodynamic model or the angular velocity of the propeller. However, this does not take into account several external circumstances. Conditions like a communication loss of the Electronic speed controller; the presence of wind and ground effect; or damage to a propeller can all have a big impact on the actual produced thrust.

Next to the developments around multirotor UAVs, a lot of popularity has been vested around 3D printing. This is called Fused filament fabrication and is a type of fast prototyping where plastics are heated and extruded in specific places with the use of a 3 degrees of freedom (DOF) robotic setup.The filament is extruded in a structured layer-by-layer fashion 3D printing allows for a fast method to transform a computer-aided design (CAD) model to an actual product. This method is not only applicable for plastics, but also cement, steel and many other materials. Within the Robotics and Mechatronics group of the university of Twente, research has been carried out on PLA (polylactide) infused with carbon. This material has the property that it is conductive. When this material is deformed after it has been printed, the resistivity of the material changes, offering the opportunity to produce 3D printed sensors. Doing so, sensors can be immediately integrated into the part that it would normally be assembled and leaving a single part with a sensor already merged into the product. This could be an advantage in the way UAVs are designed in terms of weight, ease of assembly and production time.

This project will explore the combination of these two topics. Where the goal is to develop a fully actuated multirotor that has integrated 3D printed thrust sensors.

1.2 Context

This assignment is part of the Aerial-CORE project. Aerial-CORE is an encompassing project that focuses on novel aerial manipulating robotics, specifically for maintenance and inspections of large linear infrastructures. Furthermore, within the Aerial-CORE (Aerial-CORE) project a lot of development is done with respect to strict collaboration with human workers. The project is a consortium effort, coordinated by the University of Seville[1] (UTwente), but it has branches throughout the EU to several universities and companies.

In previous work (Shenoy) at the Robotics and Mechatronics group of the University of Twente, the design of a 3D printed sensor for applications in a multirotor has been researched. This sensor is cantilever beam with strain gauges embedded in the structure. The details of this work will be further explained in chapter 2 and throughout this report.

[1] https://aerial-core.eu/

1.3 Project goals and Research questions

In this project, the integration of a 3D printed thrust sensor on a fully actuated hexarotor, the fiberthex, of the Aerial-CORE project is researched. Such a fully actuated UAV is capable of translating and rotating along x, y and z. Figure 1.1 shows the fiberthex during a flight. This UAV has a total span of 1.12 m (which includes the propellers) and weighs 2.5 kg.

Figure 1.1: Fibrethex - a fully actuated hexarotor with manipulator.

Throughout the report, design decisions and measurement setups will be based upon the parameters and the conditions of this UAV. This project consist of 2 phases: *Sensor design* and *System modelling*. For each of these phases objectives and research questions are formulated:

The **System Modelling** of the UAV includes the identification of the aerial platform with flexible arms. The goal is to include the flexibility in the arms into the model. Generating a model that requires as few parameters as possible while representing the system in a faithful way. This leads to the following research question:

- Can we relate the strain measured in the strain gauges on a multirotor UAV to the thrust force produced by the rotors?

The **Sensor Design** phase of this thesis is to design the body that the sensor should be integrated in. In this design the sensitivity, the arm deflection and the vibrations in the arms should be taken into consideration. For this phase, the following questions are formulated:

- Is there a compromise in flexibility between flight performance and sensor signal?
- What is the minimal relative resistivity change that we need to get a proper measure of the force? And what does this imply for the stiffness requirements of the sensor.

As for the **flight simulations**, it is interesting to see what influence the elasticity in the UAV has on the performance of the controller, raising the following research questions.

- With this minimum flexibility, can we use a controller that neglects this flexibility and be able to control the system and how does it compare to a rigid UAV with regards to flight performance?
- Is there a compromise in flexibility between flight performance and sensor signal?

1.4 Thesis Outline

This thesis will have the following construction :

1. Introduction

2. State of the art - A review on similar technology and an explanation on why this research is necessary.
3. Modelling - This chapter contains the modelling of the UAV with flexible arms, theory on how a strain sensor works and how this relates to the forces. It also discussed the simulation models.
4. Mechanical design & Prototyping - Discussing several sensor prototypes and the fabrication process is explained.
5. Sensor characterisation - An outline on the measurement setups used to determine the characteristics of the sensor.
6. Simulations - A comparison between the performance of a flexible and rigid UAV.
7. Discussion, Conclusion & Recommendations

2 State of the art

This chapter introduces some of the related works on the topic of this thesis and explains why there is a need for this research.

2.1 Thrust estimation

As mentioned in chapter 1, the current method of determining the thrust force of a multirotor is to compute it from the motor velocity. However, this assumes that the density around the UAV stays constant, which is often not the case. The density and pressure of the air changes often and is not uniform, especially not around a moving propeller.

In (27), an arm of a multirotor with motor and propeller have been attached to a Force-Torque sensor. This arm is then positioned in different environments where the airflow near the propeller is blocked. Additionally, a number of setups have been tested where the airflow of the measured propeller is interfered with the airflow of a second propeller in an arbitrary position.

This research showed that the largest difference in thrust force occurred when the propeller was positioned 200 mm above the floor. The propeller produced 9.51 % more thrust when compared to an open area. This extra thrust is produced by the air that is being trapped underneath the propeller, increasing the pressure and therefore increasing the thrust force. From the measurement next to a wall, a smaller increase of 3.69 % is measured.

The disturbance from a second propeller showed the opposite result. A negative effect on the thrust has been measured for both the scenarios where the propellers are placed vertically upward and vertically facing each other. This shows that even the thrust of a different motor in the UAV can have an effect on the flight performance.

These results show that the current method of estimating the thrust through the rotor velocity does not apply for circumstances in which the UAV is close to objects or near another multirotor UAV.

2.2 Physical interaction with UAVs

An example of situations where UAVs have a close encounter to flow restricting surfaces is in physical interactions with multirotor vehicles. In (26), a multirotor design has been proposed for environmental interactions. The UAV uses 3 propellers to maintain a hovering state and employs a fourth propeller to control the applied force on the inspected object. As can be seen in Figure 2.1, the propeller meant for interactions is very close to the end effector, which will therefore make it very hard to determine the exerted force from the motor velocity. To counteract that, the tip of the end effector is equipped with a force sensor to measure the applied force.

Another application of physical interactions with UAVs is the AEROARMS project (29). In this project, multiple UAVs have been developed for aerial manipulation in outdoor industrial inspection and maintenance. These manipulations are performed in a close range, as the end effector of the arms that are attached to the multirotor have a limited range. The research in (29) shows the application of the developed multirotors in an outdoor setting.

In aerial interactions, it is especially important to know the applied thrust force of each motor to be able to perform tasks that require contact with surfaces. The projects in (29) make the estimation of the thrust forces especially hard since not only the influence of the nearby surface causes a disturbance, but also due to the changing air pressure and temperature that have an effect on the accuracy of the thrust estimation.

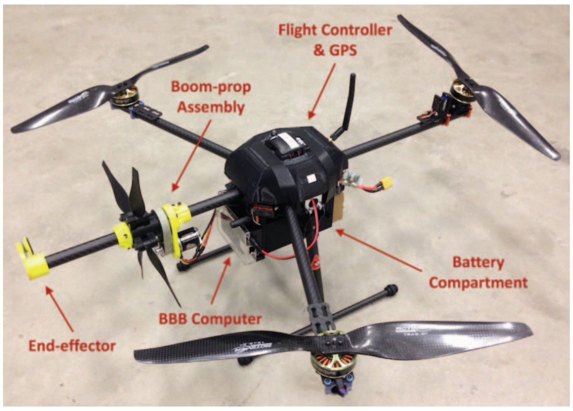

Figure 2.1: I-boom UAV designed for physical interactions (26).

2.3 Integrated thrust sensors

In order to measure the applied forces on the end effector of the aerial vehicles, a force sensor is often used. This allows for a control system to apply the correct magnitude of force that is required. However, not all applications of physical interactions have immediate contact with a surface, such as in (41) and (42). The end effector for these UAVs is a gripper, which makes it harder to integrate a force sensor in the manipulator. As a solution, a thrust force sensor has been developed by (10), to measure the thrust force of each propeller, see Figure 2.2. This sensor is a Microelectromechanical system (or MEMs) that fits in the interface between the motor and the arm of the multirotor. It is able to measure in 3 DoFs, which are the force along the z-axis and the torque around the x and y axes, assuming that the propeller rotates around the z-axis.

Figure 2.2: MEMs thrust sensor for micro UAVs by (10)

A newer sensor development for thrust sensing is based on the use of 3D printed sensors (Shenoy), which allows for a sensor that is integrated in the body of the UAV. In this research, a 3D-printed multirotor arm has been developed in which a force sensor is embedded. This force sensor consist of a strain gauge that has been produced from a piezoresistive filament (Proto-pasta). Applying strain to such a material changes the structure of the carbon particles and the networks that they form, which on its turn changes the resistance of the structure. When the strain is released, the particles go back to their original structure.

The 3D printed sensor design by (Shenoy) is shown in Figure 2.3a. The blue material is regular Polylactic Acid (PLA) and the black material is the carbon doped conducting PLA (proto pasta). The sensor contains two strain gauges, on the top and bottom of the beam. These strain gauges are designed as a meandering structure with two connection pads that act as an interface for copper wires. These would then be used to measure a voltage over the strain gauge. The thrust force on the tip of the beam is measured through the change in resistance of the strain gauges. When a force is applied to the end of the beam, the beam deflects and a strain is distributed over the entire beam. This strain is then measured by the gauges.

The beam of the sensor has a length of 200 mm, a width of 40 mm and is 5 mm thick. It has been printed with an infill density of 20 %, which is done to reduce the weight of the beam.

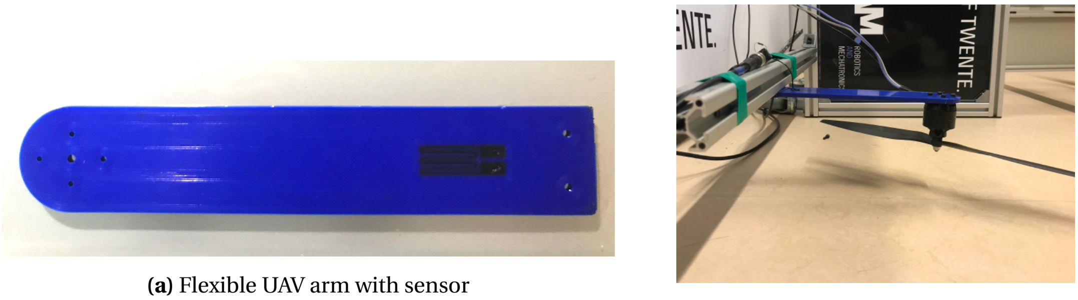

(a) Flexible UAV arm with sensor

(b) Measurement setup with motor and propeller for the developed sensor.

Figure 2.3: Proposed thrust sensor design by (Shenoy)

Figure 2.3b shows a measurement setup of the sensor where a propeller is attached to the tip of the arm which is positioned 50 mm above the floor. As can be seen in Figure 2.3b, the designed sensor already has a deflection when there is no thrust applied. However, when a thrust is applied, the beam is deflected even more. This causes the thrust vector of the propeller to deviate from the original alignment with the z-axis. This change in thrust orientation and flexibility has not been taken into account for in the model of the UAV.

2.4 Multirotor design

In (17), different multirotor designs have been reviewed with respect to their effects on task and system capabilities. It is a literature review on existing multirotor designs that is organized through the number of atomic actuation units (or AAU's). These AAU's are the mechatronic components that generate a thrust, which for most multirotors are a motor and propeller setup. The review of these multirotors starts with the UAV consisting of one single AAU and builds up to a total number of eight AAU's. Furthermore, the feasible force set of various UAVs has been visualized as in Figures 2.4b and 2.5b. These visualizations show how much translational force the UAV can exert from its center of mass (COM).

Figure 2.4a shows an example of a UAV design that has five AAU's by (2). It represents a traditional quadrotor design, but with an added actuation unit to allow for horizontal translation without the need to pitch or roll. This capability can easily be identified through the feasible force plot in Figure 2.4b. A traditional quadrotor would have a single line along the z-axis of the body frame and requires pitching or rolling to move in the xy-plane, whereas this UAV has a plane in which it can apply a translational force.

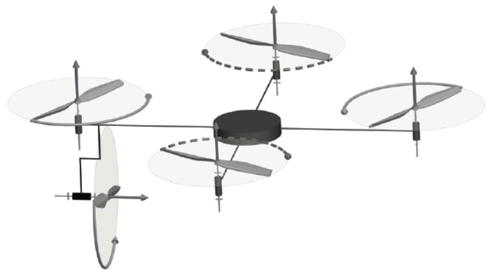

(a) Conceptual three-dimensional kinematic representation

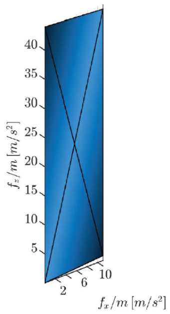

(b) Feasible force set.

Figure 2.4: An under actuated UAV with 5 rotors by (2)

Figure 2.5a shows a multirotor design by (44). It has seven atomic actuation units and is fully actuated. The added feasible force set in Figure 2.5b shows this as well for the translational forces from the COM of the vehicle. Each rotor on this multirotor is oriented differently, which enable the UAV to be fully actuated.

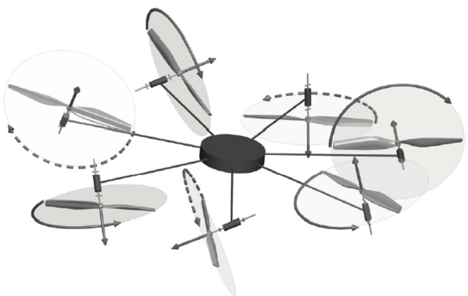

(a) Conceptual three-dimensional kinematic representation

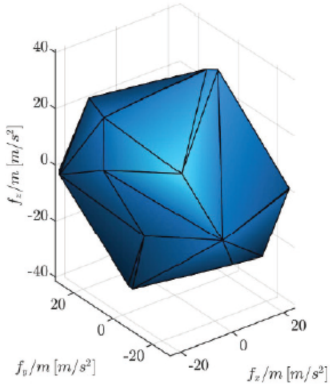

(b) Feasible force set.

Figure 2.5: An fully actuated hexarotor with tilted propellers by (44)

The paper (17) proposes a universal way to parameterize multirotor UAVs to homogenize the literature. The parametrization has been performed based on 3 abilities. The first is the ability to hover, which means how well the aircraft is able to stay in the air and in what orientations. The second ability is the trajectory tracking capability of the UAV. This ability is based upon the trajectory type and the number of degrees of freedom (or DoFs). Finally, the third ability describes the ability for a UAV to perform physical interactions. This ranges from no interactions at all, to the UAV being suitable for manipulation tasks. Table 2.1 shows an overview of these parameters. Additional to the abilities, the maturity of the multirotor design is determined for each design.

Hovering ability	
H.0	Hovering not possible.
H.1	Dynamic hovering (relaxed hovering).
H.2	Hovering in a single orientation.
H.3	Hovering in several orientations.
Trajectory tracking ability	
TT.1	Only three-dimensional position tracking is possible.
TT.2	Three-dimensional position and one-dimensional attitude (rotations along a single axis) tracking are possible.
TT.3	Three-dimensional position and two-dimensional attitude (rotations along two axes) tracking are possible.
TT.4	Three-dimensional position and three-dimensional attitude (rotations along all three axes) tracking are possible.
Physical interaction ability	
APhI.0	Not possible.
APhI.1	Suitable for tasks such as pushing/pulling.
APhI.2	Suitable fot carrying a load.
APhI.3	Suitable for manipulation tasks.
Maturity	
1	Theory.
2	Simulation of a simplified model.
3	Simulation with uncertainties and/or second order effects.
4	Prototype.

Table 2.1: Overview of the reviewed abilities of the UAVs.(17)

Relating this research to the objectives of this thesis, the research only shows configurations of rigid body UAVs. When it comes to flexibility in UAVs, the abilities that a rigid version would have will either be changed or not possible at all anymore. As this is paper is an review of the literature on multirotor configurations, it shows that there is very little research performed in flexibility in multirotor vehicles.

2.5 Conclusion

The current state of thrust force estimation in multirotor UAVs through a model on the rotor velocity has shown to be impractical for applications where the propeller is near an object or surface. For aerial operations that require physical interactions, this thrust measurement is important to compute the applied force on an end-effector. Research in thrust sensors has been performed an a start is made on the application of 3D-printed thrust force sensors. The 3D-printed sensor uses the deflection to measure the applied force by the rotor. This chapter shows that deflection is not considered in most UAV designs, therefore it shows that there is in fact a need for a flexibility analysis in UAVs if this type of sensor is equipped.

3 Modelling

This chapter discusses the behaviour and the physical properties of the sensor that will be designed and fabricated. Both the behaviour of the sensor and the effects that the proposed sensor designs will have on a multirotor UAV will be addressed.

3.1 Beam theory

In order to know how the sensor works, the physical properties of the sensor and the part it is placed upon should be discussed. Two types of designs are discussed in this chapter:

1. A cantilever beam, as in Figure 3.1, where the strain gauge and the motor are attached near the base and the free end respectively (referred to as sensor design 1).
2. A beam consisting of a flexible section and a stiff section, where the strain gauge is positioned on the flexible part and the motor attached at the end of the stiff part (referred to as sensor design 2).

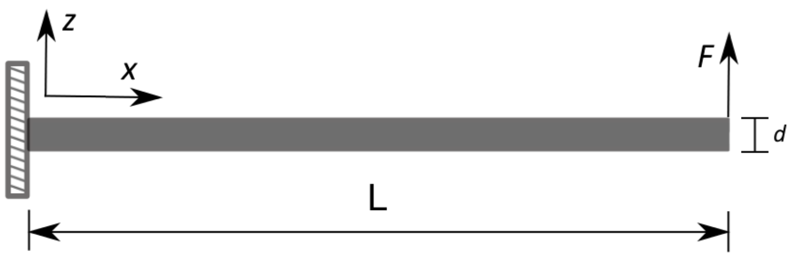

Figure 3.1: Side view of cantilever beam with length L, thickness d and applied thrust force F.

3.1.1 Cantilever Beam

In a cantilever beam as displayed in Figure 3.1, the relation between the deflection δ and moment of the applied thrust are described through the first Euler-Bernoulli (7) (16) equation 3.1:

$$\frac{d^2\delta}{dx^2} = \frac{M}{EI} \tag{3.1}$$

For a standard cantilever beam, the deflection at the point of x due to a force at the free end can be calculated with the following beam equation (7):

$$\delta(x) = \frac{Fx^2}{6EI}(3L - x) \tag{3.2}$$

Where E is the Young's modulus of the material, L is the total length and I is the second moment of inertia, that can be described by equation 3.3 (6).

$$I = \iint_R z^2 dA = \int_{-\frac{b}{2}}^{\frac{b}{2}} \int_{-\frac{d}{2}}^{\frac{d}{2}} z^2 dz dy = \int_{-\frac{b}{2}}^{\frac{b}{2}} \frac{1}{3}\frac{d^3}{4} dy = \frac{bd^3}{12} \tag{3.3}$$

In which b and d are the width and the thickness of the beam respectively. In this equation, the beam is oriented along the x-axis, as in Figure 3.1. Therefore the intersection of the beam is in the yz-plane. To derive the slope of the beam at any point, the derivative of Equation 3.2 should be taken, giving:

$$\beta(x) = \frac{d\delta(x)}{dx} = \frac{Fx}{2EI}(2L - x) \tag{3.4}$$

This is the slope at any point x on the beam, where $x = 0$ at the fixed end of the cantilever beam. The deflection and slope at the free end, where $x = L$, are then given by Equation 3.5a and 3.5b:

$$\delta_{\max} = \frac{FL^3}{3EI} \tag{3.5a}$$

$$\beta_{\max} = \frac{FL^2}{2EI} \tag{3.5b}$$

3.1.2 Strain

When the beam is flexed, a tension in the material of the beam is created. This tension stretches and compresses the material of the beam. The relative change in length on a section of the beam is called the *strain*. In order to determine the strain in the beam, a small angle approximation is used, which assumes that the curvature of the beam represents the curvature of a circle. A visual representation of this small angle approximation is presented in Figure 3.2. It is important to note that θ in Figure 3.2, has to be expressed in radians in the remainder.

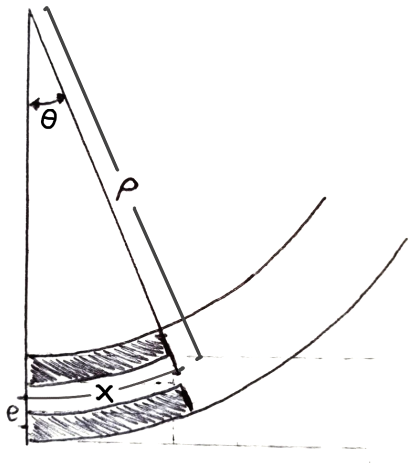

Figure 3.2: Side view of cantilever base with sensors on the top and bottom.

From this figure, it is clear that the following holds:

$$x = \rho\theta \Rightarrow \rho = \frac{x}{\theta} \Rightarrow \rho = \frac{x}{\beta(x)} \tag{3.6}$$

In the Euler-Bernoulli equation 3.4 the slope is used instead of the angle. Therefore $\beta = \tan(\theta)$ is used to transform the angle to a slope. But as $\theta \approx \tan(\theta)$, for θ going to zero, it can be stated that $\beta \approx \theta$ in equation 3.6. In Figure 3.2, e is the distance from the sensor to the center of the beam. Due to the flexural properties of a beam, there is no strain perceived along this center line. The difference in length between the center of the beam and the center of the strain gauge is denoted as Δx. Which implies the following:

$$\frac{x}{\rho} = \frac{\Delta x}{e} \Rightarrow \frac{\Delta x}{x} = \frac{e}{\rho} \Longrightarrow \frac{\Delta x}{x} = \frac{e\beta}{x} \tag{3.7}$$

Combining equations 3.4 and 3.7 gives the function that describes the strain at a certain point x:

$$\begin{aligned}\varepsilon(x) &= \frac{\Delta x}{x} = \frac{e \cdot \beta}{x} = \frac{eFx}{2EIx}(2L - x) \\ \varepsilon(x) &= \frac{eF}{2EI}(2L - x)\end{aligned} \tag{3.8}$$

Now to get the strain averaged over the entire strain gauge, the integral of the strain is taken in equation 3.9:

$$\varepsilon_{L_s} = \frac{1}{L_s}\int_0^{L_s} \varepsilon(x)dx = \frac{eF}{4EI}(4L - L_s) \tag{3.9}$$

3.1.3 Flexible hinge

For a design where the sensor is positioned in between carbon fibre rods, the equations are different. In this design, the first stiff part that is connected to the base of the UAV will be considered as rigid and therefore it can be visualized as grounded, as in Figure 3.3. In this figure, L_s is the length of the sensor and L_c is the length of the carbon rod that connects the sensor to the motor. As the thrust force of the propeller (in black) is applied at the free end of the stiff part, it is also translated as a force F and a moment M (in grey) at the other end of the stiff section, which is the connection to the flexible section at L_s. This is due to the rigid body dynamics of the system (45).

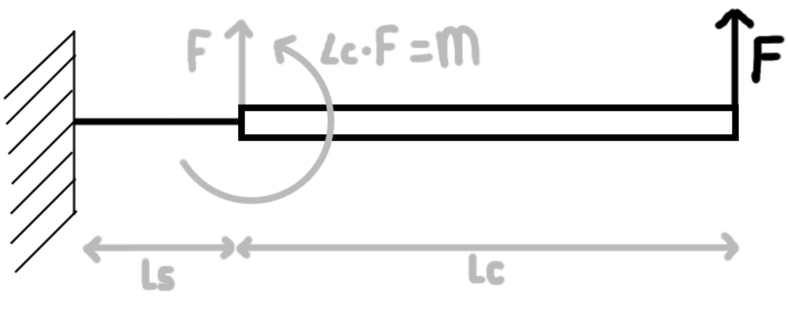

Figure 3.3: Side view of a beam design with base with flexible (L_s) and stiff part (L_c).

Using the first Euler-Bernoulli equation that relates the second derivative of the deflection to the sum of the total applied moment on the strain gauge part ($0 \leq x \leq L_s$):

$$\frac{d^2\delta}{dx^2} = \frac{M}{EI} = \frac{F(L_s - x) + FL_c}{EI} \tag{3.10}$$

Which leads to the following expressions for the slope and the deflection along the flexible part:

$$\begin{aligned}\frac{d\delta(x)}{dx} = \beta(x) &= \frac{Fx(2L_s + 2L_c - x)}{2EI} \\ \delta(x) &= \frac{Fx^2(3L_s + 3L_c - x)}{6EI}\end{aligned} \tag{3.11}$$

Then for the strain averaged over the entire sensor, equations 3.8 and 3.9 can be reused:

$$\begin{aligned}\varepsilon_{L_s} &= \frac{1}{L_s}\int_0^{L_s} \frac{e\beta(x)}{x}dx = \frac{1}{L_s}\int_0^{L_s} \frac{eF(2L_s + 2L_c - x)}{2EI}dx \\ \varepsilon_{L_s} &= \frac{eF(3L_s + 8L_c)}{8EI}\end{aligned} \tag{3.12}$$

As the motor is attached to the rigid part, the slope on the rigid part is equal to the slope at the end of the flexible section of the sensor (at $x = L_s$). This gives a slope of:

$$\beta(L_s) = \frac{FL_s(L_s + 2L_c)}{2EI} \tag{3.13a}$$

$$\delta(L_s) = \frac{FL_s^2(2L_s + 3L_c)}{6EI} \tag{3.13b}$$

Showing that, as with the slope of a cantilever beam, the slope of this sensor is solely dependent on the thrust force that is applied. The purpose of this design is to focus the strain, that would be distributed over the entire beam for the cantilever design, into the only section where the strain gauge is positioned. This allows for a higher signal output, with the same amount of deflection. It could then also be designed to have the same signal output of the sensor while requiring less deflection. An extra benefit is that this design can be modelled as a flexible hinge instead of flexible beam.This requires less processing power during simulations of such an arm, as there is no need to model a flexible body but rather rotational joint with a spring and damper.

3.1.4 Hinge location

In order to justify that sensor design 2 can actually be presented as a hinge, the point of rotation should be analysed. Figure 3.4 shows the flexible section of sensor design 2 when it is flexed. δ represents the deflection and x the position along the horizontal axis.

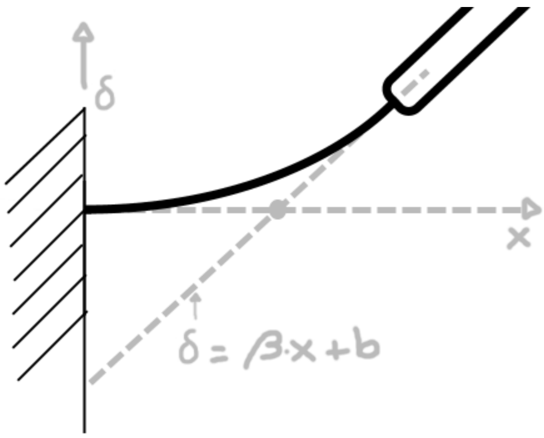

Figure 3.4: A close-up of the flexible section in sensor design 2.

The point of interest is the intersection between the line $\delta = 0$ and the dotted line which is an extension of the axis along the stiff rod. As this is a straight line, it can be described as $\delta = ax + b$. It is also known that the slope of the stiff part is equal to $\beta(L_s)$, which defines the line along the stiff part as follows:

$$\delta = \beta(L_s)x + b \tag{3.14}$$

Then b can be found from the fact that $\delta(L_s)$ is also known, giving the following expression for b:

$$b = \delta(L_s) - \beta(L_s)L_s \tag{3.15}$$

Resulting in an expression of the line along the stiff part:

$$\delta = \beta(L_s)x + \delta(L_s) - \beta(L_s)L_s \tag{3.16}$$

Then for the location of the joint, where $\delta(x) = 0$, the expression given in equation 3.17 defines the point of rotation.

$$x_{\text{joint}} = \frac{\beta(L_{\text{s}})L_{\text{s}} - \delta(L_{\text{s}})}{\beta(L_{\text{s}})} = \frac{\frac{FL_{\text{s}}^2(L_{\text{s}}+3L_{\text{c}})}{6EI}}{\frac{FL_{\text{s}}(L_{\text{s}}+2L_{\text{c}})}{2EI}} = \frac{(L_{\text{s}}+3L_{\text{C}})L_{\text{S}}}{3L_{\text{s}}+6L_{\text{c}}} \tag{3.17}$$

As Equation 3.17 is only depending on L_{s} and L_{c}, it is clear that the hinge location of sensor design 2 is fixed for any thrust applied to the sensor. This means that this design can be modelled as a rotational joint with a certain stiffness K.

3.2 Rotational stiffness

Now that the position of the hinge is known, the rotational stiffness of the elastic hinge can be derived. A schematic view of sensor design 2 is given in Figure 3.5 with the position of the hinge indicated as dot on the flexible section of the beam. In a rotational spring, the spring constant

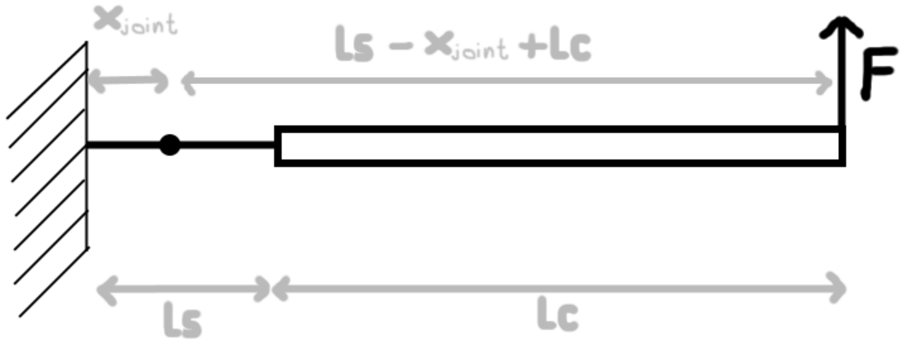

Figure 3.5: Sensor design 2 with the hinge position.

can be derived using the relationship between the applied torque τ and the resulting deflection angle β (5):

$$K = -\frac{\tau}{\beta} \tag{3.18}$$

The angle β is the angle at the end of the sensor $\beta(L_{\text{s}})$ and τ is the total momentum on the joint. The torque is the cross-product between the force and the distance between the action point of the force and the joint position, resulting in equation 3.19 (35).

$$\tau = \left(L_{\text{s}} - x_{\text{joint}} + L_{\text{c}}\right) \times F = -\left(L_{\text{s}} + L_{\text{c}} - \frac{(L_{\text{s}}+3L_{\text{C}})\,L_{\text{s}}}{3L_{\text{s}}+6L_{\text{c}}}\right) \cdot F \tag{3.19}$$

Combining Equation 3.18, 3.13a and 3.19 gives the expression for the rotational spring constant that models the flexible section of the sensor design as an elastic rotational joint:

$$K = \frac{\left(L_{\text{s}} + L_{\text{c}} - \frac{(L_{\text{s}}+3L_{\text{c}})L_{\text{s}}}{3L_{\text{s}}+6L_{\text{c}}}\right) \cdot F}{\frac{(L_{\text{s}}+2L_{\text{c}})FL_{\text{s}}}{2EI}} = \left(L_{\text{s}} + L_{\text{c}} - \frac{(L_{\text{s}}+3L_{\text{C}})\,L_{\text{s}}}{3L_{\text{s}}+6L_{\text{c}}}\right) \cdot \frac{2EI}{(L_{\text{s}}+2L_{\text{c}})\,L_{\text{s}}} \tag{3.20}$$

Which is, similar to the position of the point of rotation, not relying on the thrust force, but only on the dimensions of the design and the material properties.

3.3 Damping

When modelling an elastic rotational joint, it is important to model it as a mass-spring-damper system. If the damping is neglected, it is impossible for oscillations to dissipate in the system, which can make the system uncontrollable. In this case, the elastic joint is also modelled as a rotational mass-spring-damper system, having a systems equation of motion as given in 3.21 (40), where the assumption is made that there is no input to the system and therefore the right hand side of the equation is set to zero.

$$I\frac{d\theta^2 x}{dt^2} + c\frac{d\theta}{dt} + K\theta = 0 \tag{3.21}$$

Where I is the moment of inertia, c is the damping factor and K is the torsional spring constant. For a system with damping, often the damping ratio ζ is used, it is defined as the actual damping over the critical damping (Brown):

$$\zeta = \frac{c}{c_\mathrm{c}} \tag{3.22}$$

With the critical damping described as in equation 3.23.

$$c_\mathrm{c} = 2I\omega_\mathrm{n} \tag{3.23}$$

Where ω_n is the natural angular frequency in rad/s of the system. To get to the angular frequency, the natural frequency in Hz has to be converted using the following equation (9):

$$\omega_\mathrm{n} = 2\pi f_\mathrm{n} \tag{3.24}$$

In a second order system, as a mass-spring-damper system, ζ shows whether the system is underdamped ($0 < \zeta < 1$), overdamped ($\zeta > 1$) or critically damped ($\zeta = 1$). In the case that the system is underdamped, ζ can be derived by the logarithmic decrement of the signal, which is also called δ (Brown):

$$\zeta = \frac{\delta}{\sqrt{\delta^2 + (2\pi)^2}} \quad , \quad \delta = \ln\frac{x_1}{x_2} \tag{3.25}$$

With x_1 and x_2 being the absolute values of the peaks in the oscillations. In Figure 3.6 such an underdamped signal response is shown.

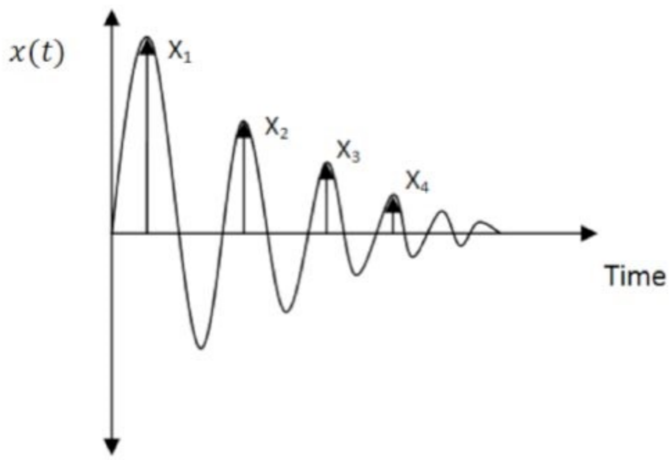

Figure 3.6: A signal response from an underdamped system. (19)

3.4 UAV Dynamics

When designing a multirotor with flexible arms, a model is to be made to review the effects of elasticity on the flight performance. In this section, the difference in dynamics of a conventional multirotor UAV and a multirotor that has elastic joints in the arms, are derived. To do so, some simplifications have been made:

- 2 dimensional model:
  - Only movement in xz-plane.
  - No pitch or yaw, only roll.
  - No effect of the motor torque on the system.
- The joints are modelled as an elastic hinge.

3.4.1 Rigid body dynamics

For traditional multirotor UAV, rigid body dynamics are used to model the behaviour of the drone. To start, the simplest model can be used to investigate the elastic properties. The simplest model in this case would be a 2D model, only existing in the xz-plane as displayed in Figure 3.7:

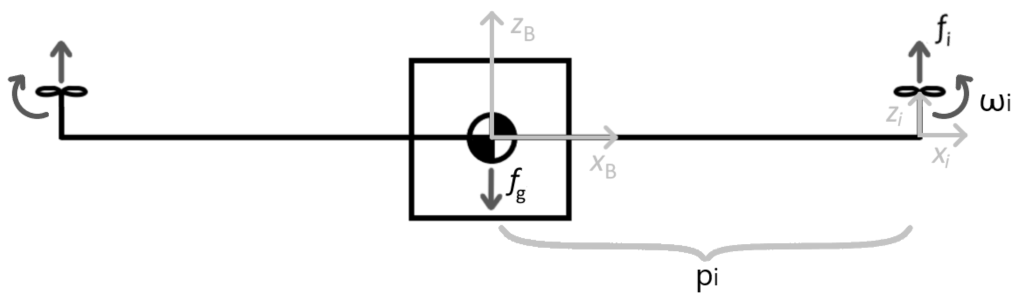

Figure 3.7: The schematic representation of a 2D multirotor

In this configuration, the thrust force generated by each propeller is derived by equation 3.26, where ω_i is the spinning velocity of the rotor and c_{f_i} is the lift constant of each propeller (17).

$$f_i = c_{f_i} |\omega_i| \omega_i \tag{3.26}$$

This model can only rotate around the axis perpendicular to the xz-plane, the drag forces produced by the propellers are neglected. In Figure 3.7, the body frame $\mathcal{F}_B = O_B, \{x_B, z_B\}$ is located in the center of mass and the propeller frame $\mathcal{F}_i = O_i, \{x_i, z_i\}$is located at end of the arm beneath the propeller. The gravitational force is noted as f_g.

To derive the dynamic behaviour of such a UAV, the Euler-Lagrange equation (14) is used:

$$\frac{d}{dt}\frac{\partial L}{\partial \dot{\mathbf{q}}} - \frac{\partial L}{\partial \mathbf{q}} = \mathbf{W}(\mathbf{q}, \mathbf{u}) \tag{3.27}$$

In this equation, the vector $\mathbf{q}$ represents the states of the system, which are the position and the orientation of the UAV in the world frame $\mathcal{F}_W = O_W, \{x, z\}$. $\mathbf{u}$ is the vector that holds the thrusts of the motors and $\mathbf{W}$ is the wrench that the inputs have on the system. L is the Lagrangian function (22) sums the kinetic, and subtracts the potential energy in the system:

$$L(\dot{\mathbf{q}}, \mathbf{q}) = T_{\text{translational}} + T_{\text{rotational}} - U_{\text{gravity}} \tag{3.28}$$

With $\mathbf{q}$ and $\dot{\mathbf{q}}$ defined as:

$$\begin{aligned} \mathbf{q} &= (\mathbf{p}_{\text{uav}}^{\text{T}}\ \phi)^{\text{T}} = (x\ z\ \phi)^{\text{T}} \\ \dot{\mathbf{q}} &= (\dot{\mathbf{p}}_{\text{uav}}^{\text{T}}\ \omega_y)^{\text{T}} = (\dot{x}\ \dot{z}\ \omega_y)^{\text{T}} \end{aligned} \tag{3.29}$$

With ϕ the rotation angle around the y-axis and ω_y being the rotational velocity around the y-axis. As the UAV can only fly in the xz-plane, the "y-axis" is not actually used. However, since a cross product between two vectors in the xz-plane results in a scalar value that moves around the axis that is perpendicular to the xz-plane, "y-axis" is used for convenience in the report. Furthermore, when working with a 2 dimensional UAV it is possible to state that $\frac{d\phi}{dt} = \omega_y$, as there is only one rotational state to take into account. For a 3 dimensional model this is not the case and more computations need to be performed to get from ϕ to ω_y. Filling in the kinetic and potential energies in equation 3.28 gives:

$$L(\dot{\mathbf{q}}, \mathbf{q}) = \frac{1}{2} m \dot{\mathbf{p}}_{\text{uav}}^{\text{T}} \dot{\mathbf{p}}_{\text{uav}} + \frac{1}{2} \dot{\phi}^{\text{T}} J_{\text{uav}} \dot{\phi} - m \mathbf{g}^{\text{T}} z \tag{3.30}$$

Here, m is the mass of the UAV, J_{uav} is the inertia matrix and $\mathbf{g} = (00g)^{\text{T}}$ with g as the gravitational acceleration. Then combining equations 3.27 and 3.30 gives the systems equations of dynamics (17):

$$\begin{bmatrix} m\ddot{\boldsymbol{p}}_{\text{uav}} \\ J\ddot{\phi} \end{bmatrix} + \begin{bmatrix} m\boldsymbol{g}z \\ {}^{\text{W}}\omega_{\text{B}} \times J^{\text{W}}\omega_{\text{y}} \end{bmatrix} = \mathbf{W}(\mathbf{q}, \mathbf{u}) \tag{3.31}$$

The wrench on the UAV $\mathbf{W}$ is composed of the forces and the torques on the body, seen from the world frame $\mathscr{F}_{\text{W}}$ as in equation 3.32.

$$\mathbf{W}(\mathbf{q},\mathbf{u}) = \begin{bmatrix} \mathbf{F}_W(\mathbf{q},\mathbf{u}) \\ \tau_{\text{W}}(\mathbf{u}) \end{bmatrix} \tag{3.32}$$

In this equation, the forces seen in $\mathscr{F}_{\text{W}}$ are composed of the forces in $\mathscr{F}_{\text{B}}$ fed through a rotation matrix ${}^{\text{W}}R_{\text{B}}$ that rotates from $\mathscr{F}_{\text{B}}$ to $\mathscr{F}_{\text{W}}$:

$$\begin{aligned} \mathbf{F}_{\text{W}}(\mathbf{q},\mathbf{u}) &= {}^{\text{W}}R_{\text{B}}\mathbf{F}_{\text{B}}(\mathbf{u}) \\ &= \begin{bmatrix} \cos(\phi) & -\sin(\phi) \\ \sin(\phi) & \cos(\phi) \end{bmatrix} \mathbf{F}_{\text{B}}(\mathbf{u}) \end{aligned} \tag{3.33}$$

Then to compute the forces seen in $\mathscr{F}_{\text{B}}$:

$$\begin{aligned} F_{\text{B}}(\mathbf{u}) &= \sum_{\text{i}=1}^{2} {}^{\text{W}}R_{\text{i}} f_{\text{i}} = \sum_{\text{i}=1}^{2} \begin{bmatrix} \cos(0) & -\sin(0) \\ \sin(0) & \cos(0) \end{bmatrix} \begin{bmatrix} 0 \\ f_{\text{i}} \end{bmatrix} \\ &= \sum_{\text{i}=1}^{2} \boldsymbol{I} \begin{bmatrix} 0 \\ f_{\text{i}} \end{bmatrix} = \sum_{\text{i}=1}^{2} \begin{bmatrix} 0 \\ f_{\text{i}} \end{bmatrix} \end{aligned} \tag{3.34}$$

The rotation matrix ${}^{\text{W}}R_{\text{i}}$ is the transformation from the propeller frame $\mathscr{F}_{\text{i}}$ to $\mathscr{F}_{\text{B}}$. Since there is no angle of the rotation between $\mathscr{F}_{\text{i}}$ and $\mathscr{F}_{\text{B}}$, the rotation matrix becomes the identity matrix $\boldsymbol{I}$. The torque on the body can be defined as in equation 3.35. This torque is defined around the y-axis:

$$\tau_{\text{B}}(u) = \sum_{\text{i}=1}^{2} p_{\text{i}} \times f_{\text{i}} \tag{3.35}$$

Here p_{i} is the distance between $\mathscr{F}_{\text{i}}$ and $\mathscr{F}_{\text{B}}$.

Since this model is a two-dimensional model, the xz-plane of both $\mathscr{F}_{\mathrm{B}}$ and $\mathscr{F}_{\mathrm{W}}$ are in the same plane. This means that the torque on the body τ_{B} is always in the same direction as the torque expressed in the world frame τ_{W}. Therefore there is no transformation required, leaving $\tau_{\mathrm{W}} = \tau_{\mathrm{B}}$.

The total system equations of dynamics becomes:

$$\begin{bmatrix} m\ddot{\boldsymbol{p}}_{\mathrm{uav}} \\ J\ddot{\phi} \end{bmatrix} + \begin{bmatrix} m\boldsymbol{g}^{\mathrm{T}} z \\ {}^{\mathrm{W}}\omega_{\mathrm{B}} \times J^{\mathrm{W}}\omega \end{bmatrix} = \begin{bmatrix} \sum_{\mathrm{i}=1}^{2} {}^{\mathrm{W}}R_{\mathrm{B}} \begin{bmatrix} 0 \\ f_{\mathrm{i}} \end{bmatrix} \\ \sum_{\mathrm{i}=1}^{2} p_{\mathrm{i}} \times f_{\mathrm{i}} \end{bmatrix} \tag{3.36}$$

3.4.2 Flexible joints

When expanding the rigid model from Figure 3.7 to a system where flexibility is introduced in the form of elastic joints, the system displayed in Figure 3.8 is acquired. In this figure, an extra frame $\mathscr{F}_{\mathrm{ji}}$ is added that represents the frame of the flexible hinge-joint of propeller i. β in this image, is the rotation angle between $\mathscr{F}_{\mathrm{i}}$ and $\mathscr{F}_{\mathrm{B}}$ expressed in radians. As seen in Figure 3.8, this system has 3 different bodies with each its own mass, and therefore the gravitational forces act upon each center of mass individually.

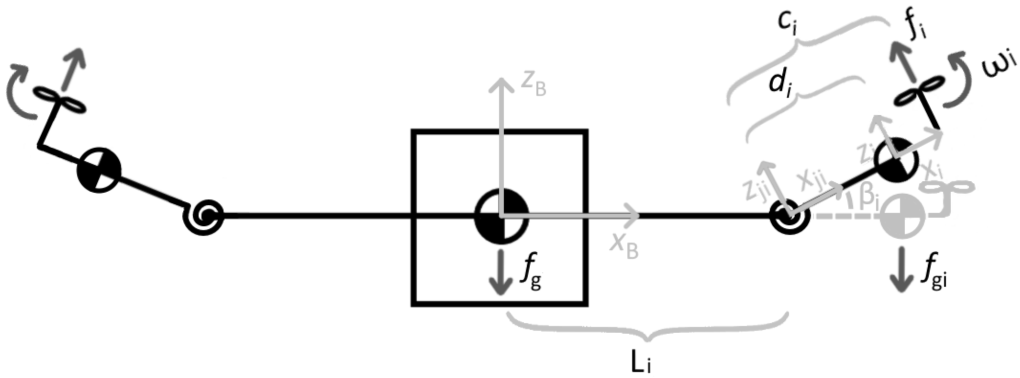

Figure 3.8: The schematic representation of a 2D multirotor with elastic joints

For this system, the same Euler-Lagrange equation can be used as presented in equation 3.27, but this time apart from having the wrench **W(q,u)** an extra damping term $\mathbf{D}(\dot{\mathbf{q}})$ gets added on the right hand side of the equation:

$$\frac{d}{dt}\frac{\partial L}{\partial \dot{\mathbf{q}}} - \frac{\partial L}{\partial \mathbf{q}} = \mathbf{W}(\mathbf{q},\mathbf{u}) + \mathbf{D}(\dot{\mathbf{q}}) \tag{3.37}$$

However, in this case two extra states are added: β_1 and β_2. Each representing the joint angle of their corresponding arms. Resulting in the state vectors $\mathbf{q}$ and $\dot{\mathbf{q}}$ as:

$$\begin{aligned} \mathbf{q} &= (\mathbf{p}_{\mathrm{uav}}^{T}\ \phi\ \beta)^{\mathrm{T}} = (x\ z\ \phi\ \beta_1\ \beta_2)^{\mathrm{T}} \\ \dot{\mathbf{q}} &= (\dot{\mathbf{p}}_{\mathrm{uav}}^{T}\ \omega_y\ \dot{\beta})^{\mathrm{T}} = (\dot{x}\ \dot{z}\ \omega_y\ \dot{\beta}_1\ \dot{\beta}_2)^{\mathrm{T}} \end{aligned} \tag{3.38}$$

The Lagrangian as presented in equation 3.28 now also becomes a bit different, since the potential energy in the system does not only consist of the gravitational forces, but also the potential energy stored in the elastic rotational joint (or spring). The Lagrangian (22) looks as follows:

$$L(\dot{\mathbf{q}},\mathbf{q}) = T_{\mathrm{translational}} + T_{\mathrm{rotational}} - U_{\mathrm{gravity}} - U_{\mathrm{elastic}} \tag{3.39}$$

The computed result of equation 3.39 can be found in equation 3.40.

$$
\begin{aligned}
L(\dot{\mathbf{q}},\mathbf{q}) = \frac{1}{2}m^{\mathrm{W}}\dot{\mathbf{p}}_{\mathrm{uav}}^{\mathrm{T}}\,{}^{\mathrm{W}}\dot{\mathbf{p}}_{\mathrm{uav}} + \frac{1}{2}\omega_{\mathrm{y}}J_{\mathrm{uav}}\omega_{\mathrm{y}} + \sum_{\mathrm{i}=1}^{2}\left(\frac{1}{2}m_{\mathrm{i}}{}^{\mathrm{W}}\dot{\mathbf{p}}_{\mathrm{i,com}}^{\mathrm{T}}\,{}^{\mathrm{W}}\dot{\mathbf{p}}_{\mathrm{i,com}} + \frac{1}{2}\omega_{\mathrm{i,com}}J_{\mathrm{i}}\omega_{\mathrm{i,com}}\right) \\
-\left(m\mathbf{g}^{\mathrm{T}}z + \sum_{\mathrm{i}=1}^{2}m_{\mathrm{i}}\mathbf{g}^{\mathrm{T}}p_{\mathrm{i,com}} + \sum_{\mathrm{i}=1}^{2}\frac{1}{2}K_{\mathrm{i}}\beta_{\mathrm{i}}^{2}\right)
\end{aligned}
\tag{3.40}
$$

In this representation of the Lagrangian: m_{i} is the mass of arm i; J_{i} is the inertia of each arm; K_{i} is the rotational spring constant of each joint and $\omega_{\mathrm{i,com}}$ and $\mathbf{p}_{\mathrm{i,com}}$ are formulated as below:

$$\omega_{\mathrm{i,com}} = \dot{\phi} + \dot{\beta}_{\mathrm{i}} \tag{3.41a}$$

$$\mathbf{p}_{\mathrm{i,com}} = {}^{\mathrm{W}}\mathbf{p}_{\mathrm{uav}} + {}^{\mathrm{W}}R_{\mathrm{B}}(\phi)\left(\begin{bmatrix} L \\ 0 \end{bmatrix} + {}^{\mathrm{B}}R_{\mathrm{i}}(\beta_{\mathrm{i}})d\right) \tag{3.41b}$$

Combining the Euler-Lagrange equation 3.37 and the Lagrangian 3.40 leads to the system equations of dynamics for the UAV with elastic joints (37):

$$\mathbf{M}(\mathbf{q})\ddot{\mathbf{q}} + \mathbf{C}(\mathbf{q},\dot{\mathbf{q}}) + \mathbf{G}(\mathbf{q}) = \mathbf{W}(\mathbf{q},\mathbf{u}) + \mathbf{D}(\dot{\mathbf{q}}) \tag{3.42}$$

Unlike the case for the rigid model, this model is far more complex; the computation of the equation above includes many operations between rotation matrices and variables. In this equation, $\mathbf{M(q)}$ is the inertia matrix with dimensions (5×5); $\mathbf{C}(\mathbf{q},\dot{\mathbf{q}})$ describes the centrifugal and the Coriolis forces; and $\mathbf{G}(\mathbf{q})$ contains the gravitational forces and the spring forces. The applied wrench to the system is defined similarly to the rigid system in 3.32, however in this case the torque on the joints is also included:

$$\mathbf{W}(\mathbf{q},\mathbf{u}) = \begin{bmatrix} F_{\mathrm{W}} \\ \tau_{\mathrm{W}} \\ \tau_{\beta_1} \\ \tau_{\beta_2} \end{bmatrix} = \begin{bmatrix} \sum_{\mathrm{i}=1}^{2} {}^{\mathrm{W}}R_{\mathrm{B}}{}^{\mathrm{B}}R_{\mathrm{i}}\begin{bmatrix} 0 \\ 1 \end{bmatrix} f_{\mathrm{i}} \\ \sum_{\mathrm{i}=1}^{2}(L_{\mathrm{i}} + {}^{\mathrm{B}}R_{\mathrm{i}}\begin{bmatrix} c_{\mathrm{i}} \\ 0 \end{bmatrix}) \times (\begin{bmatrix} 0 \\ 1 \end{bmatrix} f_{\mathrm{i}}) \\ -c_1 \cdot f_1 \\ c_2 \cdot f_2 \end{bmatrix} \tag{3.43}$$

The torque on the body τ_{B} (with again $\tau_{\mathrm{W}} = \tau_{\mathrm{B}}$) is also different from the rigid case. This is due to the fact that the position of the thrust with respect to the body frame $\mathscr{F}_{\mathrm{B}}$ changes with β and therefore the distance between $\mathscr{F}_{\mathrm{B}}$ and $\mathscr{F}_{\mathrm{i}}$ is not a constant anymore.

The damping term $\mathbf{D}(\dot{\mathbf{q}})$ in equation 3.42 is defined as:

$$\mathbf{D}(\dot{\mathbf{q}}) = \begin{bmatrix} 0 \\ 0 \\ 0 \\ -d\cdot\dot{\beta}_1 \\ -d\cdot\dot{\beta}_2 \end{bmatrix} \tag{3.44}$$

It can be seen that this damping term only has an influence on the joints in the UAV. d is the damping factor as described in section 3.3. When observing the propagation of the signals, the system equations dynamics are notated in the following manner:

$$\ddot{\mathbf{q}} = \mathbf{M}(\mathbf{q})^{-1}\left(-\mathbf{C}(\mathbf{q},\dot{\mathbf{q}}) - \mathbf{G}(\mathbf{q}) + \mathbf{W}(\mathbf{q},\mathbf{u}) + \mathbf{D}(\dot{\mathbf{q}})\right) \tag{3.45}$$

The matrices $\mathbf{W}(\mathbf{q},\mathbf{u})$ and $\mathbf{D}(\dot{\mathbf{q}})$ are computed as in equations 3.43 and 3.44 respectively. Through the Lagrangian in equation 3.40 the matrices in equation 3.45 have been computed with the use of the Matlab Symbolic toolbox (Mathworks).

3.5 UAV system model

In order to compare the flight performance of a single rigid body multirotor with a multirotor that incorporates elastic hinges, a model for both systems should be constructed.

Figure 3.9 shows the overview of the system model that is made in Simulink (Mathworks) and Matlab (Mathworks). The clock symbol at the left represents the time dependence of the system, which is fed into the trajectory planning block. Inside this block, a 9th order polynomial is constructed to create a smooth curve from the initial position p_{start} at t_{init} to the desired end position p_{end} at $t = T$, seen in equation 3.46. This smooth curve creates the reference trajectory for the UAV and has been designed in a previous work. Together with a reference position, a reference velocity and a reference acceleration are created in this block. These reference trajectories are then passed to the controller block.

$$\boldsymbol{p}_{\text{ref}} = \boldsymbol{p}_{\text{start}} + (\boldsymbol{p}_{\text{end}} - p_{\text{start}}) \cdot ((t^5 \cdot (126 \cdot T^4 - 420 * T^3 \cdot t + 540 \cdot T^2 \cdot t^2 - 315 \cdot T \cdot t^3 + 70 \cdot t^4)) / T^9) \quad (3.46)$$

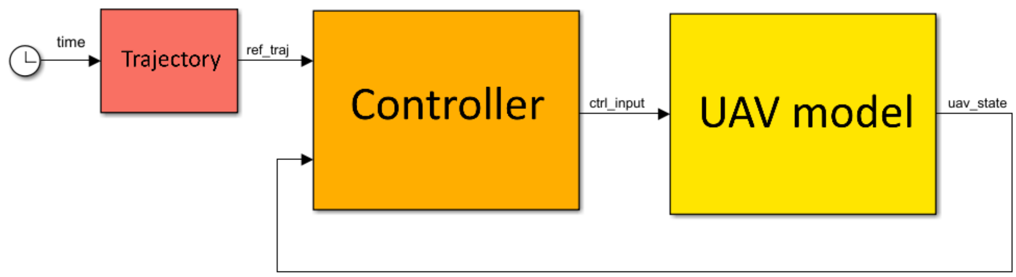

Figure 3.9: UAV system with trajectory, controller and UAV model

3.5.1 Controller

To ensure the consistency of the simulation results, a single controller will be used throughout this thesis. This controller is only given the model of a rigid UAV. This is to see whether the same controller can be used if 3D printed sensors are included. The controller that is used is a controller that has been used in the past on a Tilt-Hex drone, which is similar to the Fiberthex, a fully actuated hexarotor. The original controller is a Full-Pose Geometric controller that can track any feasible 6-D trajectory. It is designed to not be affected by singularities of local chart orientation representations, as can be read in (15). This controller computes a cylinder of feasible forces from the center-of-mass at hovering. This cylinder takes into account the minimal and maximum rotor velocities for the specific UAV.

The systems that this controller is applied to in this thesis is under-actuated from fully actuated. Even in the 2-D plane, this system is under-actuated. In order to use this controller, it has been restrained to only be able to act in the xz-plane. Furthermore, the radius of the feasible forces cylinder is set to zero, as both motors are oriented in the principal direction of the UAV. This lets the controller know that it cannot move in any other direction apart from the z-axis without rotating the UAV. Doing so, the controller implements only PD control in the position and attitude of the UAV, as can be seen in Figure 3.10. Further explanation on this controller can be found in (15).

The controller computes the position error with

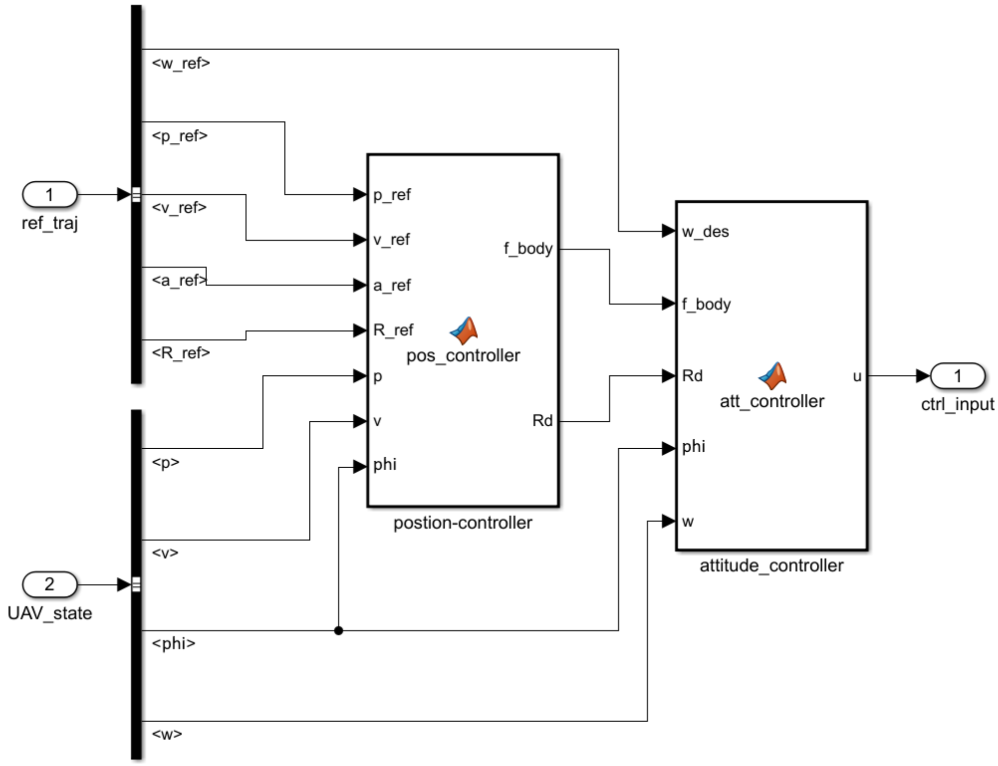

Figure 3.10: Controller used for both systems.

3.5.2 System dynamics

In Figure 3.11, the system of the rigid UAV is presented. The input $\boldsymbol{u}$ to this system is $|\omega_\mathrm{i}|\omega_\mathrm{i}$ which is the motor speed squared of each motor, given as input in a vector form. In the block "dynamics", this motor speed is first multiplied with the lift constant c_f to use it in the evolution of the system as stated in equation 3.36. Furthermore, the output of this block are the components of $\ddot{\mathbf{q}}$:

- The acceleration $\mathbf{a}$ (in x and z).
- The angular acceleration $\dot{\omega}_y$.

In Figure 3.11 $\dot{\omega}_y$ is denoted as "aw".

These are then propagated through integration blocks "$\frac{1}{s}$", to get back to the states which are fed back into the "dynamics" block. As noted in section 3.4.1, the integration of ω_y to receive ϕ can only be performed due to the fact that this system is a 2 dimensional system in the xz-plane, meaning that the "y-axis" will always point in the same direction.

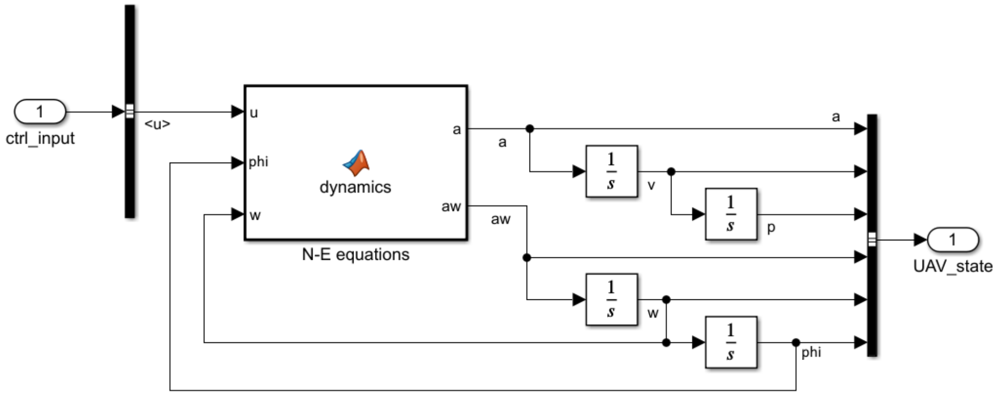

Figure 3.11: Dynamic model for the rigid UAV.

The system for the UAV with elastic hinges is represented in Figure 3.12. It can be immediately seen that the number of inputs to the "dynamics" block is increased. Due to the addition of the rotational spring and the rotational damper, the signals for β and $\dot{\beta}$ are required respectively to acquire the propagation of the states. Furthermore, an extra output is added, which is $\ddot{\beta}$.

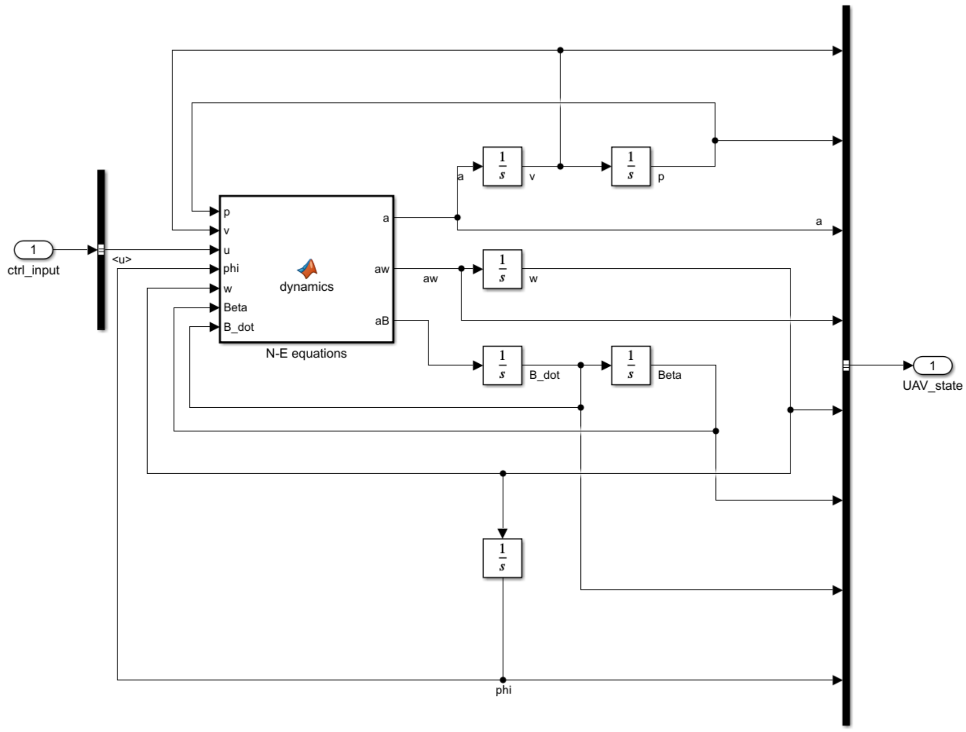

Figure 3.12: Dynamic model for the UAV with elastic joints.

3.6 conclusion

In this chapter, the relationship between the applied thrust force and the stain in the integrated strain gauges is determined for two sensor designs. Furthermore, the dynamics of a rigid and a flexible UAV have been derived for to create a model of the vehicles. Both these models are represented a 2D plane. The system equations of dynamics have been processed in Simulink (Mathworks) together with a controller to stabilize the models in simulations.

4 Mechanical design & Prototyping

In this chapter, the design of the Simulink and Matlab implementation of the rigid and flexible UAV will be explained. Furthermore, a controller is proposed and the different types of beams designs are discussed and compared.

4.1 Beam prototypes

As mentioned in chapter 3 , the choice has been made to proceed with 2 types of sensor designs:

- Design 1: a full cantilever beam.
- Design 2: two rigid sections with a flexible part in between.

Both designs use the strain gauge design that has been developed in a previous MSc assignment by Nikhil Shenoy (Shenoy).

In this MSc assignment, research is performed into the most suitable filament for this type of sensor, which has been concluded to be Proto-pasta (Proto-pasta). Proto Pasta is a type of PLA that contains carbon particles. This allows the material to conduct electricity and it appears to be very suitable for a strain gauge sensor. Furthermore, to keep uniform material density throughout the sensor, PLA (proto pasta) is used as the non-conducting material and functions as the main material for the beam/sensor designs.

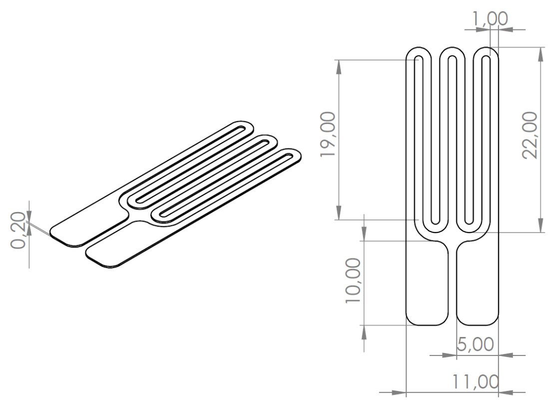

Figure 4.1: The previously developed strain gauge for 3D printing.

In Figure 4.1, a schematic drawing of this strain gauge is presented. The strain gauge design has a length of 22 mm long due to the rounded corners at the end. The sections that are designed to measure the strain, the straight lines, are 19 mm long. The width of the strip is 1 mm wide, but the total width of the strain gauge is 11 mm wide due to the 5 end-loops that the strip has. The thickness of the sensor is 200 μm.

As the strain on the strain gauge is oriented vertically to the sensor, being for the schematic on the right side in Figure 4.1, the curved sections (where the current through the gauge is perpendicular to the strain) are neglected when it comes to the equations. This means that the sensor length is taken to be L_s =19 mm.

In both sensor designs, this strain gauge is used without any alterations to the design so that the characteristics of the sensor ideally do not differ between the sensors.

4.1.1 Cantilever

Sensor design 1 has been designed as a cantilever beam with the strain gauge attached on both the top and the bottom near the base of the beam. As can be seen in Equations 3.9 and 3.3, assuming that the beam is uniform, there are 3 dimensions that can be chosen in this design: the length L, the width b and the thickness d. Since the strain gauges are placed on the top and bottom of the beam, the parameter e is set to be $e = b/2$. Furthermore, as the sensor is specifically designed to be placed upon the fiberthex, L will be set to L=308 mm. Which is the distance of the arm from the center of the motor to the point of attachment to the body of the UAV.

For the first prototype of sensor design 1, the minimum width of the beam has been chosen. Being the width of the strain gauge plus a small wall of 1 mm PLA to ensure that the strain gauge design does not deform or expand during the 3D printing process.

The second prototype of sensor design 1 is designed to be a square beam. The width and the height of the beam are equal. The length and width of design 1 are determined by the dimensions of the Fiberthex and the strain gauge. However, the height is free to choose. As can be seen in equation 3.3, the second moment of inertia is largely dependent on the height d of the design. To determine the height of the sensors, a maximum deflection at the end of the beam has been taken as 4 mm at a thrust force of 14 N by the propeller. Which is near the maximum amount of thrust that the propeller can supply in combination with the selected motor. Using this deflection, equation 3.5a is used to determine the height of both prototypes of sensor design 1. For the tall prototype, a width of b = 13 mm is used and for the prototype with a square intersection, a width of $b = d$ is used to calculate the height. The dimensions of these prototypes can be found in table 4.1. The tall and the square prototype of sensor design 1 are displayed in Figures 4.2 and 4.3 respectively (Solidworks).

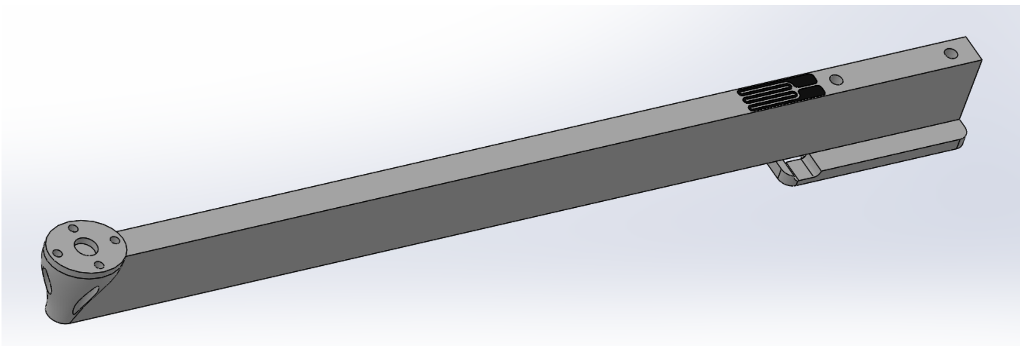

Figure 4.2: Prototype of sensor design 1 with minimum width.

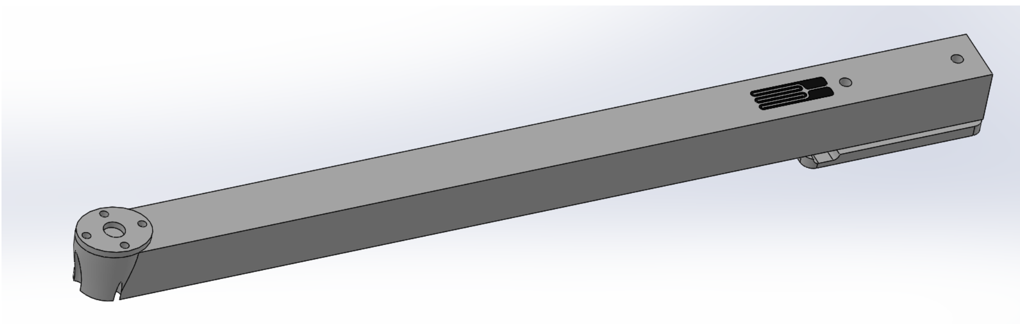

Figure 4.3: Prototype of sensor design 1 as a square beam.

Printability

However, due to the required length of these prototypes, it is not suitable to be printed with the available 3D printers at the laboratory of the Robotics and Mechatronics group (RaM) at the University of Twente (UTwente), due to their limited build-volumes. Therefore, miniature versions of the prototypes have been designed to be able to fit on a build plate of the available printers.

These miniature version are designed to perceive the same amount of strain in the strain gauge as the original sized prototypes, but with a maximum force of 3.5 N:

- A length of $\frac{1}{3}$-th the original length: $L = 102.67\,\mathrm{mm}$.
- The same width: $b = 13\,\mathrm{mm}$.
- A maximum exerted force of $\frac{1}{4}$-th the original maximum force: $F_{\mathrm{max}} = 3.5\,\mathrm{N}$.

By using these parameters and using the fact that the strain in the sensors should be the same amount, the height of both miniature sensors is determined. The dimensions of all cantilever beam models are stated in table 4.1. Additionally, a representation of one of the miniature prototypes is given in Figure 4.4.

Design:	1 tall	1 tall-m	1 square	1 square-m
width [mm]	13	13	24.4	24.4
height [mm]	30.1	8.5	24.4	6.9
length [mm]	308	102.7	308	102.7

Table 4.1: An overview on the dimensions of all prototypes of sensor design 1.

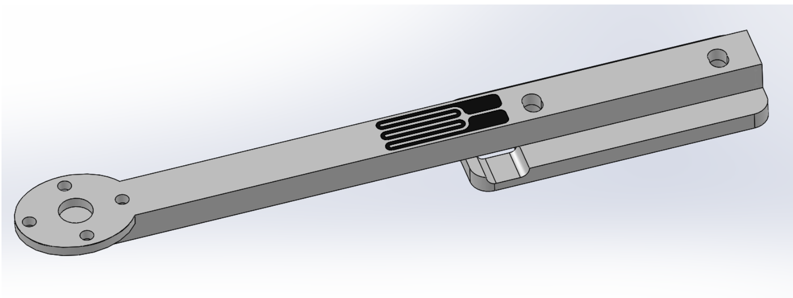

Figure 4.4: Miniature prototype of sensor design 1 with minimum width.

4.1.2 Flexible hinge

The second sensor design consists of both rigid and flexible sections. To confine with the design of the Fiberthex, carbon fibre tubes will be used as the rigid sections in the arm. These tubes have a diameter of 16 mm with a wall thickness of 1 mm.

The 3D printed sensor has been designed to make sure that the strain caused by the propeller is primarily distributed over the elongated sections of the strain gauges. This is the 19 mm long section of the strain gauge in Figure 4.1. To do so, this section is designed to be the thinnest part of the design. The other parts of the strain gauge are covered with non-conducting PLA, creating a thicker section that is less flexible.

The position of the sensor has been taken to be exactly in the middle of the total length of the arm. This can also be seen in Figure 4.5. The flexible section has a width b and a height d of

13 mm and as mentioned a length L_s of 19 mm. Due to the sensors placement in the middle of the total length of the arm, the distance of the rigid section to the position of the motor is:

$$L_c = \frac{L_{arm} - L_s}{2} = \frac{308 - 19}{2} = 144.5 \text{ mm} \tag{4.1}$$

An overview of the dimensions and parameters of this design are summarized in table 4.2:

Parameter	Value	Unit
L_s	19	mm
L_c	144.5	mm
b	13	mm
d	13	mm
e	6.5	mm
E	23E8	N/m^2

Table 4.2: The parameters of sensor design 2.

In order to put a current through the strain gauges, the connection pads need to be reachable. To do so, the connection pads of the strain gauges have a tower of Proto-pasta on them until they reach the surface of the surrounding PLA. This does add more resistance to the gauge, but since the pads are relatively large in surface (compared to the rest of the strain gauge), the added resistance should be minimal.

Furthermore, an interface between the sensor and the carbon fibre rods has been created. This interface consists of an extension of the PLA along the bottom side of the carbon rods, following the rounded curvature of the bottom side of the rods. To fasten the sensor design to the rods, 2 clamps on each side of the sensor have been used. These are then connected through screws and bolts to the bottom section of the sensor, with a distance of 40 mm between the clamps on both sides. Figures 4.5 and 4.6 give a clear render of this sensor:

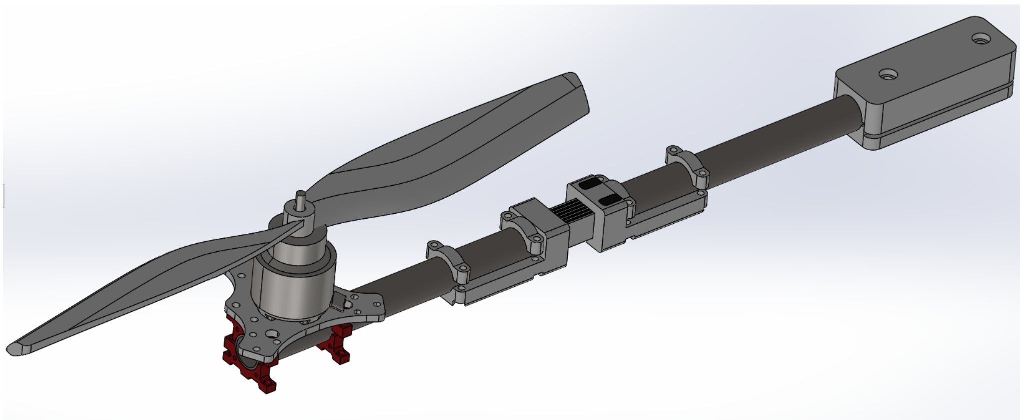

Figure 4.5: Prototype of sensor design 2.

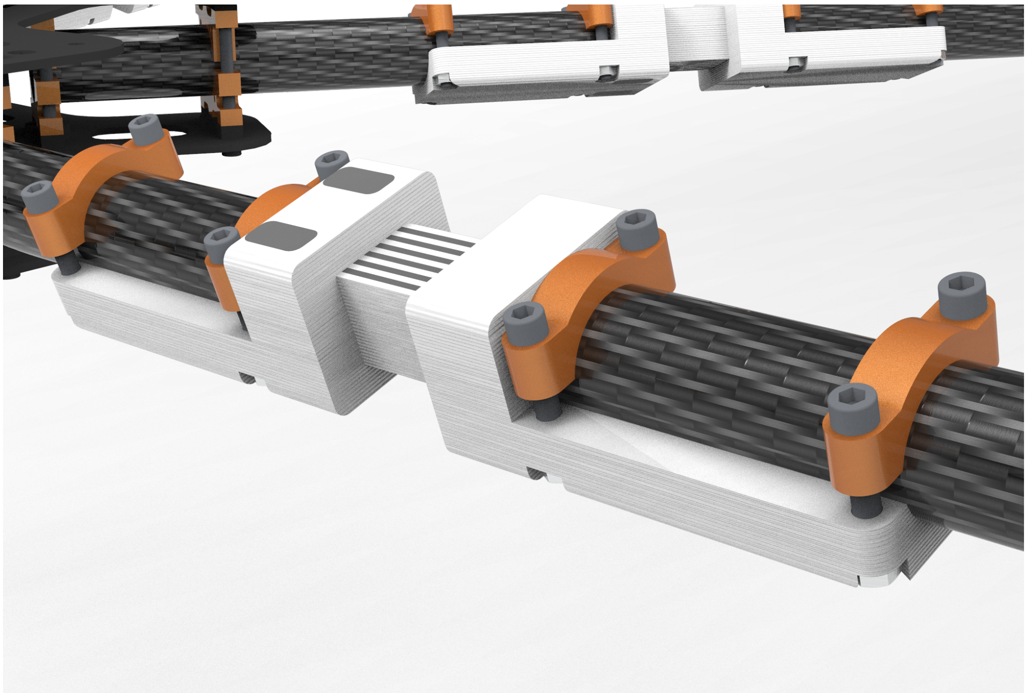

Figure 4.6: A close up render of sensor design 2 on the arms of a Fiberthex.

Using the parameters stated in table 4.2, the rotational stiffness K of the sensor can be determined for when it is modelled as a rotational hinge. Filling in the parameters, the stiffness K is determined with equation 3.20 to be $K = 288.48\,\mathrm{Nm/rad}$.

$$K = \left(L_\mathrm{s} + L_\mathrm{c} - \frac{(L_\mathrm{s} + 3L_\mathrm{c})\, L_\mathrm{s}}{3L_\mathrm{s} + 6L_\mathrm{c}}\right) \cdot \frac{2EI}{(L_\mathrm{s} + 2L_\mathrm{c})\, L_\mathrm{s}} \tag{3.20}$$

4.2 Fabrication process

In this section the fabrication process will be discussed. This section shows the configuration at which the models have been printed and the printing results.

4.2.1 Introduction

The materials that are used in this project are polylactic acid (PLA), conductive PLA from Proto-pasta and butene-diol vinyl alcohol (BVOH) (Verbatim). PLA is a stiff but durable plastic filament which is very suitable for 3D printing. Due to the fact that it is a non-brittle material, it is an appropriate material to produce a flexure sensor while having a stiff body. In (Shenoy), the choice of material is elaborated.

Proto-pasta is a type of PLA with carbon particles infused in the PLA. This gives the material piezoresistive properties, meaning that when this material is subjected to stress or strain the layout of the carbon particles changes. This changes the conductivity of the material.

The third material that is used is BVOH. It is a filament that, after printing, can be dissolved in water. This makes it a very suitable support material. When a part of the design is overhanging, this material can be printed underneath, the BVOH acts as a surface on which the material of the overhang can be printed.

In Figure 4.8 and 4.7, the printing layout of the prototypes are visualized. In both designs, extra towers have been added next to the bodies of the sensors. These towers are used to enhance the printing quality of the parts. During the printing process, every time the printer switches between materials (and thus between nozzles), a new layer of material is added to the tower before adding a new layer to the sensor body. This ensures that the printer will extrude the hot filament when it starts the next layer of the sensor body.

Additionally, at the very beginning of the print, a brim is added around the layout (sensor and towers). This brim has a similar function as the towers, with the only difference that the brim is only used at the very beginning of the printing process.

As stated above, both sensor designs have a strain gauge on the top and on the bottom of the body. For sensor design 1, the first layer that will be printed on the build plate also contains one of the strain gauges. This means that the bottom gauge is printed on a flat surface, and the top gauge is printed on a layer of PLA. In previous works (Shenoy), it shows that the smoothness of the build plate can cause the bottom strain gauge to have different dimensions than designed. Which will result in a different resistivity and resistance of the gauge. In (21), a method is proposed by providing an extra layer of support material below the sensor design to increase the similarity of the dimensions of both strain gauges. This on its term decreases the difference in electrical properties, such as the resistance of the gauges. In the fabrication of both designs, an attempt is made to print the prototype on a layer of BVOH. In Figure 4.8, the BVOH is displayed in purple. It can be seen that the strain gauge is elevated from the printing surface, therefore only in that location the layer of BVOH is added together with the locations to hold the nuts.

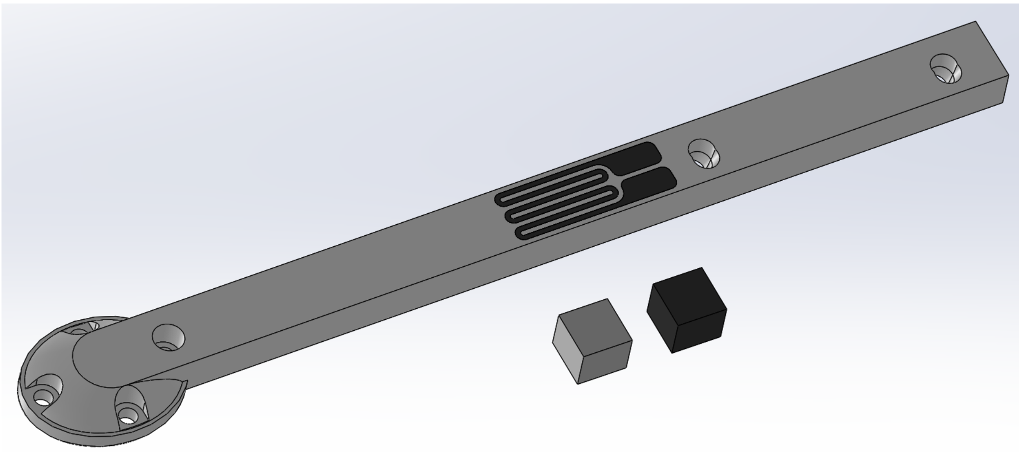

Figure 4.7: Printing layout of sensor design 1

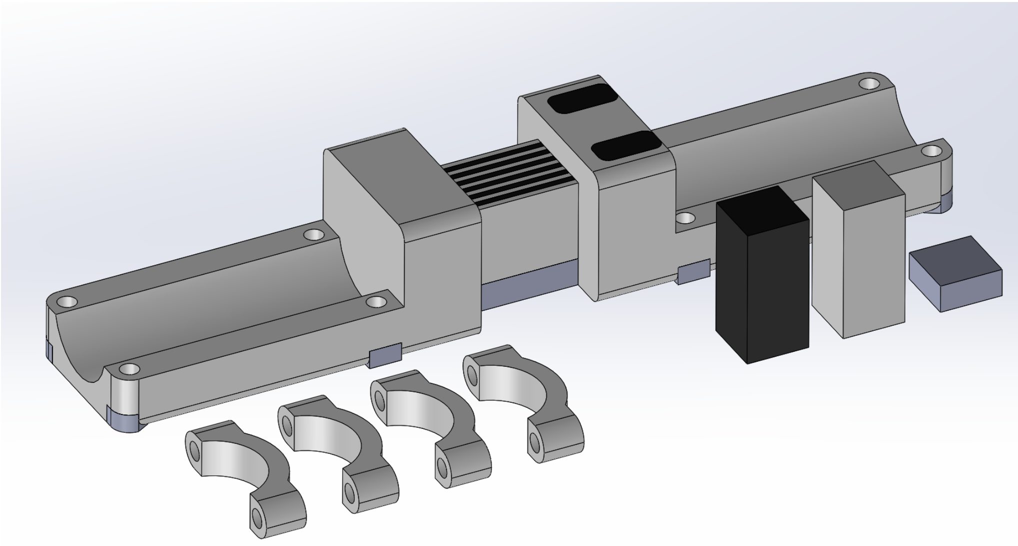

Figure 4.8: Printing layout of sensor design 2

3D printer

For printing multiple materials in a single print, a Diabase H-series printer has been used (Diabase). This is a printer that holds up to 5 different filaments with a separate extruder for each filament. This allows for multi-material printing without the risk of materials mixing in one extruder head. The build plate of this printer has a size of 420 × 170 mm and it is able to print up to a height of 200 mm. This printer has a heated bed, made from glass on which a wide strip Kapton tape is adhered. This is done to ease the process of removing the prints from the build plate.

For the parts that did not need to consist of multiple materials, the mounts, a Prusa i3 (Prusa) printer has been used. This printer is a smaller printer that is much easier in use, but it is only capable of printing a single material. This allows for fast prototyping of small parts. For these prints red PLA has been used. This printer has a spring steel sheet as a build plate, which makes it easier to remove the prints from the build plate.

4.2.2 Prints

This section shows the results and the errors which occurred during the fabrication process.

Samples

Since previous work has been done with the same printer and materials, the same printer parameters have been used for the first prints. These parameters can be found in table 4.3. Next to that, initial settings have been used for BVOH, which correspond with the recommended parameters by the producers of this filament.

	PLA	Proto Pasta	BVOH
Temp. °C.	210	205	210
heat bed °C.	60	60	60
Nozzle diameter mm	.4	.4	.4
Print speed mm/s	60	60	30
Flow rate %	90	110	100
extrusion width mm	.43	.43	.40
Layer height mm	.2	.2	.2

Table 4.3: Overview of the initial printer settings

Figure 4.9 shows one the very first results of the prints with BVOH. It can be seen that halfway during the first layer of PLA, the adhesion between the filaments failed and the layer of PLA peeled away. This is however not the case for the Proto-pasta. Different parameters have been tested, but this would not solve the bonding issue between the PLA and the BVOH. Therefore the decision was made to remove this initial layer of BVOH from the prototypes of sensor design 1.

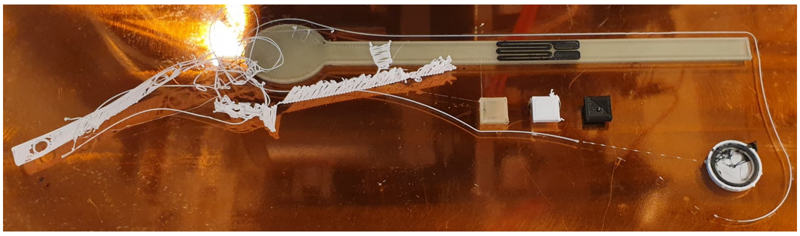

Figure 4.9: Initial print of design 1 with BVOH

Figure 4.10 shows more of the intermediate results.

After multiple attempts of printing the miniature version of sensor design 1, small prototyping samples have been created to decrease the time it took to tune the printing parameters. These prototyping samples can be seen in the lower right corner of Figure 4.10.

Figure 4.10: Initial printing results

Mounts

As mentioned earlier, the designs for the interface between the sensors and the ground have been printed on a Prusa i3 printer. These mounts are used to attach the sensor to a solid ground during measurements.

Since the bottom strain gauge of design 1 is placed immediately at the bottom surface of the beam, a hole had to be provided in the sensor mount for a wired interface with the strain gauge. This hole has a small slid to the side of the mount to feed the wires to the pads of the strain gauge, as seen in Figure 4.11a. Figure 4.11b shows a mount to attach a cylindrical carbon fibre rod to the ground. This design contains an upper part and a bottom part that interlock the carbon rod. Additionally, the mount is designed to drill 2 holes through the carbon rod, to ensure that the rod won't rotate around its longitudinal axis.

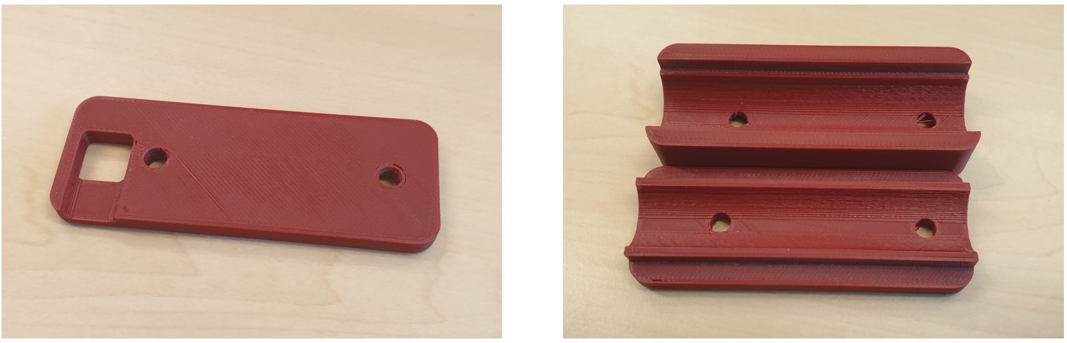

(a) Mount for sensor design 1 **(b)** Mount for sensor design 2

Figure 4.11: Base mounts for both designs

Final prints

The final prints are presented in Figures 4.12 and 4.13. After multiple trials, the printing parameters were found which produced a sensor of desired quality. These final parameters can be found in table 4.4. For the quality of the strain gauges, the most important parameters were the printing temperature and the flow rate of the PLA and the Proto-pasta. The printing temperature is the temperature at which the heating element in the extruder is set to melt the filament, whereas the flow rate of a material is the volume of the filament that passes the extruder with respect to the volume that is required in the design. By tuning these parameters, the junction between the PLA and Proto-pasta is clear and without any mixing of the materials.

	PLA	Proto Pasta	BVOH
Temp. C.	210	200	210
heat bed C.	60	60	60
Nozzle diameter mm	0.4	0.4	0.4
Print speed mm/s	60	60	60
Flow rate %	87	100	100
extrusion width mm	.43	.43	.43
Layer height mm	.2	.2	.2

Table 4.4: The most important printer settings.

As mentioned, the final prototypes of sensor design 1 have been on the build plate of the printer instead of a layer of BVOH. This was due to the adhesion issue between the PLA and the BVOH. However, the Diabase was able to print the prototype of sensor design 2 with the added BVOH underneath the section of the strain gauge. The success of this print is presumably due to the fact that the PLA around the strain gauge had to bridge a small section of BVOH before it was attached to PLA again. As sensor design 2 was not printed on a layer of BVOH over the entire bottom side but rather over a small section underneath the elongated section of the strain gauge (the black lines in Figure 4.13a).

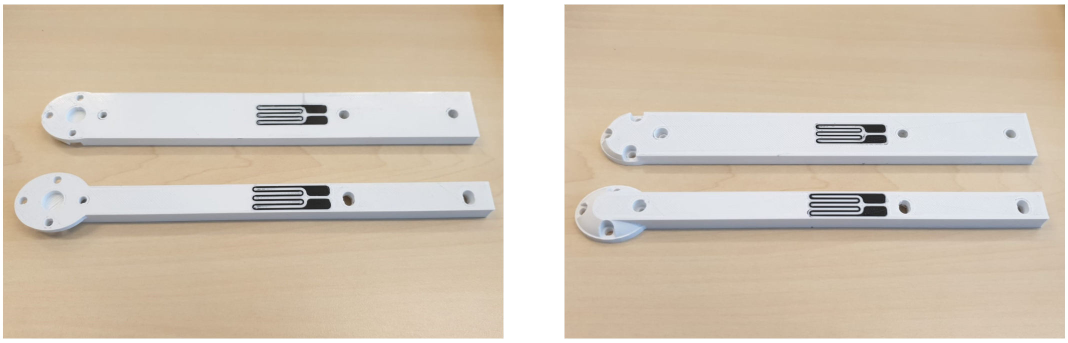

(a) Bottom **(b)** Top

Figure 4.12: Final prints of sensor design 1 - miniature versions

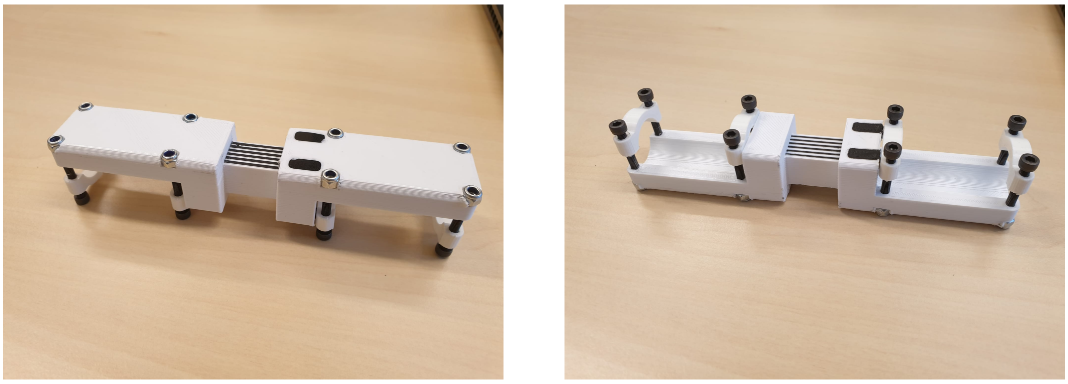

(a) Bottom **(b)** Top

Figure 4.13: Final print of sensor design 2

Connection interface

In order to use the sensor, a wired interface has been made to the strain gauges. Insulated copper wires are connected to the connection pads of the strain gauges. To do so, conducting silver epoxy (MGChemicals) has been used to act as glue. The epoxy needs a period of 24 hours of curing time, therefore hot glue has been used to secure the insulated part of the wires to make sure that the stripped copper does not move from the connector pads.

The result of the wired interfaces on the sensors is presented in Figure 4.14. After the epoxy has cured, the resistance of each strain gauge could be measured. These are shown in table 4.5. It can be clearly seen that for the strain gauges of sensor design 1, the resistance of the bottom strain gauges is up to double the resistance of the top gauge. However, for sensor design 2 this is not the case. The difference between the top and the bottom gauge is much smaller. The effects of the BVOH layer is clearly visible when comparing the resistances of the bottom gauges of each sensor.

When comparing the top gauges of each sensor, it is noteworthy to point out that the resistances of these gauges are very similar, even though the strain gauge of sensor design 2 has a much larger volume of Proto-pasta as the connector pad before it is connected to the strain gauge (as explained in section 4.1.2).

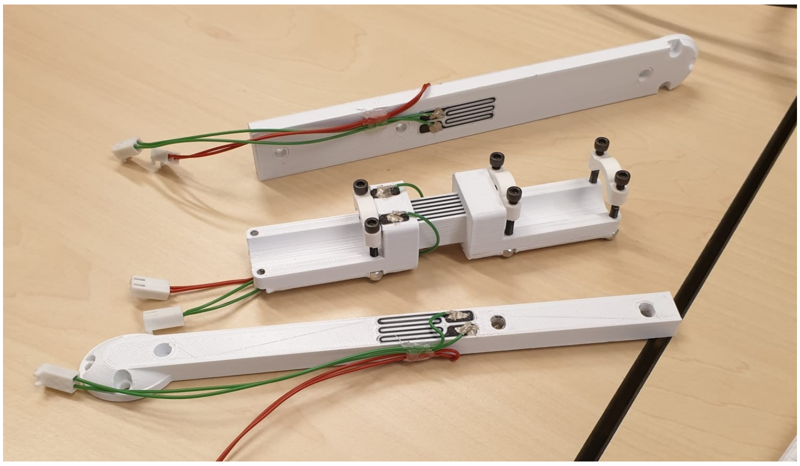

Figure 4.14: Final prototypes of the sensor designs with wired interfaces.

Design	1 - tall-m	1 - square-m	2
Bottom gauge kΩ	153.6	244.5	84.5
Top gauge kΩ	104.5	112.7	108.5

Table 4.5: Resistance of each strain gauge in the designs.

4.2.3 Conclusion

In this chapter, 2 types of designs have been modelled and prototyped. The materials that have been used to print these sensors are PLA, conductive PLA and BVOH. Miniature version have been made for Design 1 to fit on the build plate of the 3D-printer. It is clear that the quality of the prints is highly reliant on the printing parameters for each material. Furthermore, the design of the sensor is an important factor on the quality of the strain gauges in the sensor. Although the strain gauges in sensor design 2 have added material to the connection pads, the overall resistance of the gauges is equal or even lower than the resistance in comparison to the gauges in design 1.

5 Sensor characterisation

In this section, the characterisation of the sensors is discussed and an explanation on the measurement setup of the sensors is given.

5.1 Sensor readout

In order to determine the applied forces on the sensor designs from the strain gauges the properties of a strain gauge should be elaborated. A strain gauge is a type of resistor that is made of electrically conducting material that can stretch and compress. When this happens, the resistivity (or relative change in resistance) of the resistor changes. In strain gauges, this can be formulated as in equation 5.1. Where $\Delta R/R$ is the relative change in resistivity of the gauge, $\Delta L/L$ is the relative change in sensor length and GF is the *gauge factor* of the sensor. The gauge factor of a strain gauge is the sensor parameter that shows the relationship between the mechanical domain and the electric domain. This factor GF expresses the sensitivity of the sensor.

$$\frac{\Delta R}{R} = \mathrm{GF} \cdot \frac{\Delta L}{L} = \mathrm{GF} \cdot \varepsilon \tag{5.1}$$

To measure the change in resistance, a "readout" circuit is used. This circuit measures the change in resistance of the sensor, and thus the strain in the strain gauge.

The circuit that will be used in this application is a half- Wheatstone bridge circuit (13), as presented in Figure 5.1. This type of circuit allows for a differential measurement with two strain gauges. Which in this case are the top and bottom strain gauges on the sensor designs. With a half-Wheatstone bridge circuit the effect of temperature changes is minimized, as any change in temperature will result in an identical change in resistance in both strain gauges. Due to their placement in the Wheatstone bridge, the effect of temperature will be cancelled out (13). As voltage on the negative node of V_o is a fixed voltage, a potentiometer is used for the resistances R_1 and R_2. This potentiometer is then tuned before the measurement to set the initial output voltage V_o to 0 V when there is no force applied to the sensor. For this setup, a potentiometer of 200 kΩ has been used.

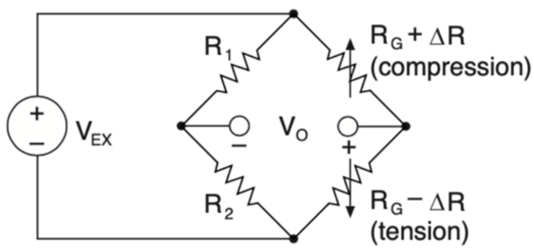

Figure 5.1: A half-Wheatstone bridge circuit for a differential measurement. (18)

In this circuit, the output voltage V_o is given by equation 5.2, where V_{EX} is the external DC voltage.

$$\frac{V_o}{V_{EX}} = \frac{-\Delta R/R}{2} = \frac{-\mathrm{GF} \cdot \varepsilon}{2} \Rightarrow \mathrm{GF} = \frac{-2 \cdot V_o}{\varepsilon \cdot V_{\mathrm{EX}}} \tag{5.2}$$

5.1.1 Gauge factor

Using the received equation to calculate the gauge factor GF in 5.2, the relationship between the measured voltage V_o and the strain ε is created. As there is a different relationship between the applied force on the sensor design and the strain for each design, there is a different relationship between the applied force F_{act} and the output voltage V_o.

Combining equations 5.2 and 3.9 gives this relationship for sensor design 1:

$$F_{\text{sens}} = -\frac{8 \cdot E \cdot I}{\text{GF} \cdot e \cdot (4L + L_{\text{s}}) \cdot V_{\text{EX}}} \cdot V_o \tag{5.3}$$

And combining 5.2 and 3.12 gives this relationship for sensor design 2:

$$F_{\text{sens}} = -\frac{16 \cdot E \cdot I}{\text{GF} \cdot e \cdot (3L_{\text{s}} + 8L_{\text{c}}) \cdot V_{\text{EX}}} \cdot V_o \tag{5.4}$$

5.2 Linear actuator setup

To verify the sensor model and the 3D printed sensor designs, a measurement setup is built that mimics the actuation of the propeller on the sensor. To simulate the thrust force on the sensor, a SMAC is used (SMAC) 5.2 a schematic representation is given of the measurement setup for sensor design 1. The multimeter that is used in this setup is the Keithley 2000 (Keithley). This is a bench multimeter with a resolution up to 0.1 µV and a sampling rate up to 50 Hz with this resolution. The external DC voltage of the Wheatstone bridge V_{EX} is supplied by an arduino UNO (Ardiuno) and has been set to 5 V.

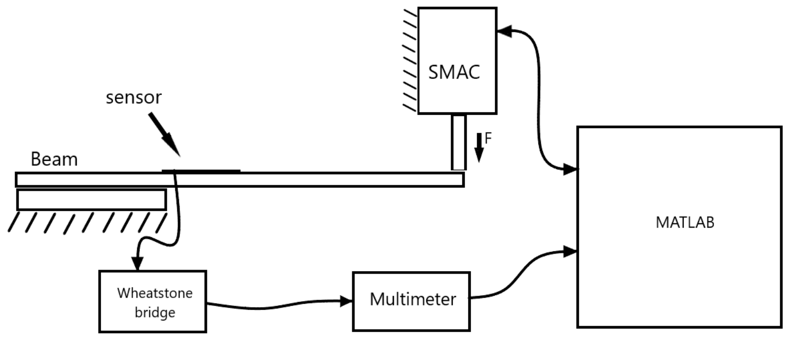

Figure 5.2: Schematic of the measurement setup with the SMAC

Due to the available materials and mounting configurations for the linear actuator, the measurement setup represents an inverted propeller setup, meaning that the simulated thrust is oriented downwards. Therefore, the sensors are all mounted in a flipped orientation. For each sensor prototype, the piston of the linear actuator is positioned to push along the same axis that the propeller would spin around. Considering that all prototypes have been designed to deflect a few millimeters at this location, the interface between the piston and the beams is not a fixed connection. Doing so, the piston gives an external force on the sensor.

For sensor design 2, an orange clip is mounted to make the interface more secure at the location of the propeller axis, since the cylindrical shape of the carbon fibre rod could create inconsistent contact with the tip of the piston.

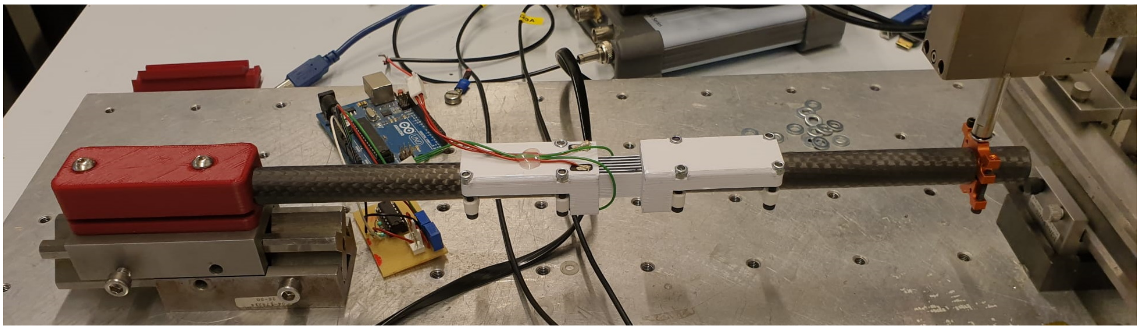

Figure 5.3: The measurement setup of sensor design 2 with the linear actuator

5.2.1 Design 1

As this measurement setup allows for a very accurate measurement of the output voltage as well as the applied force, it will be used to determine the gauge factor of both sensor designs. Using equation 5.3, the gauge factor for the prototypes of design 1 will be computed as follows:

$$\mathrm{GF}_{\mathrm{design1}} = -\frac{8 \cdot E \cdot I}{e \cdot (4L + L_s) \cdot V_{\mathrm{EX}}} \cdot \frac{V_o}{F_{\mathrm{sens}}} \tag{5.5}$$

To find this factor, the linear actuator exerts a force on the sensor in a sinusoidal waveform. As the prototypes of design 1 are miniature versions, this sinusoidal force goes from 0 to 3.5 N at a frequency of 0.2 Hz.

In Figure 5.4 and 5.5, the blue plots represent the exerted force by the linear actuator. The orange plot is the force as measured by the sensor, using the determined gauge factor GF. Throughout this report, this color indication will be used.
For design 1, the gauge factors are computed to be $GF = -4.7101$ and $GF = -4.8303$ for the miniature narrow and the miniature square designs respectively.

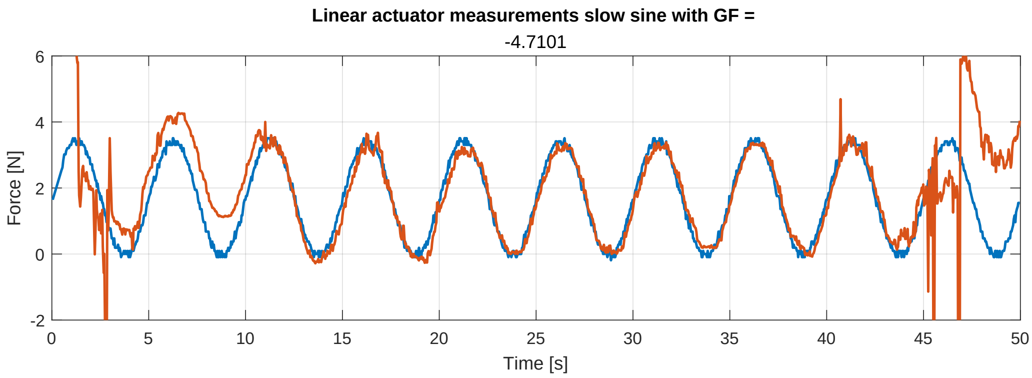

Figure 5.4: A measurement of a 0.2 Hz sine on the mini version of the narrow prototype of design 1

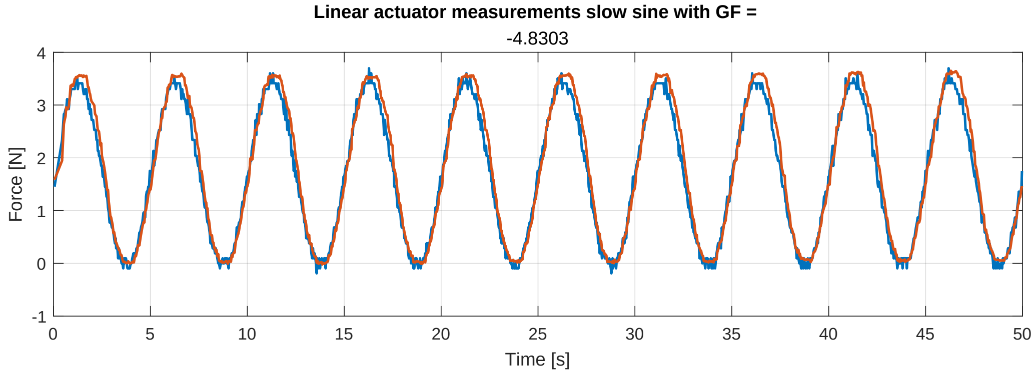

Figure 5.5: A measurement of a 0.2 Hz sine on the mini version of the square prototype of design 1

In Figure 5.4, it can clearly be seen that the sensor does not respond as expected. It seems that the sensor signal is very unreliable. This may be caused by a printing error in the strain gauge. In photo 4.12, the strain gauge does not seem to show any faults when compared to the original design of the strain gauge in Figure 4.1. However, the possibility that a printing error occurred beneath the surface of the print is still present.

Another explanation on the unusual behaviour could be a caused by the wired interface to the strain gauge with conducting epoxy. If the epoxy did not bond entirely to the connection pads of the strain gauge, the sensor can show unpredictable behaviour. The epoxy is a two component based synthetic resin, which needs to be mixed carefully. The epoxy might not conduct as expected if the components are not mixed properly.

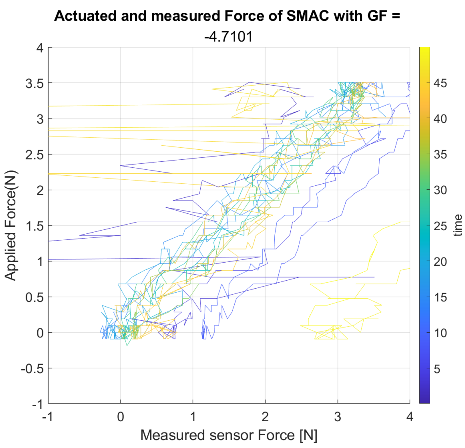

(a) Miniature of narrow design 1.

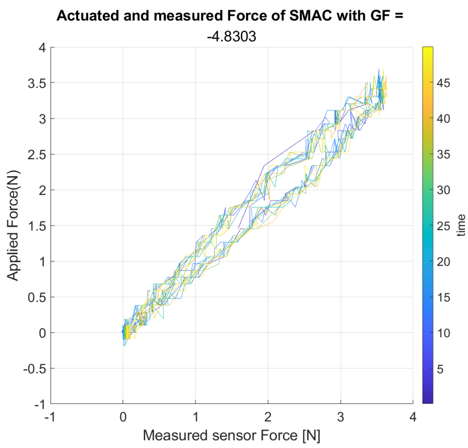

(b) Miniature of squared design 1.

Figure 5.6: Actuated force vs measured force for the prototypes of design 1.

Figure 5.6 shows the relationship between the actuation force and the measured force over time, where the time goes from 0 seconds in blue, to 50 seconds in yellow.

These figures allow to observe the amount of hysteresis of the sensors. When there is a difference between an approach from the lower bound to a value and an approach from the upper bound of the sensor data, the sensor exhibits hysteresis. This can visually be seen by the openness of the plots in Figure 5.6. As can be seen in both measurements, a small amount of hysteresis is visible. However, the hysteresis in 5.6b is centered around the imaginary diagonal line from 0 to 3.5 N and the difference between increasing and decreasing approach is relatively small. This shows that the sensors behave near linear.

5.2.2 Design 2

As the relation between the strain and the exerted force is different for sensor design 2 compared to sensor design 1, the calculation of the gauge factor is also different. Using equation 5.4, the gauge factor is computed as follows:

$$GF_{\text{design2}} = -\frac{16 \cdot E \cdot I}{e \cdot (3L_s + 8L_c) \cdot V_{\text{EX}}} \cdot \frac{V_o}{F_{\text{act}}} \tag{5.6}$$

Similar to the prototypes of sensor design 1, the gauge factor for this design is determined with a force applied to the sensor in a sinusoidal waveform from 0 to 12 N at 0.2 Hz. This signal is presented in Figure 5.7. The gauge factor that was found for sensor design 2 is $GF = -4.6741$. This value is expected as the same strain gauge is used as in the prototypes of design 1.

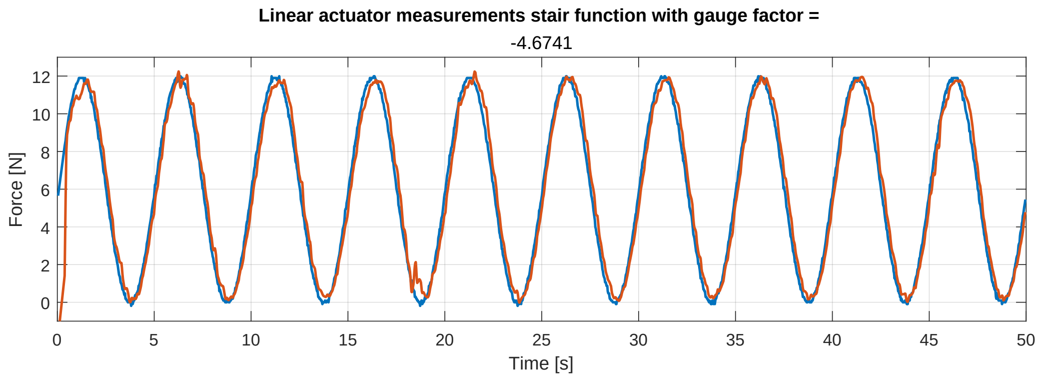

Figure 5.7: A measurement of a 0.2 Hz sine on design 2

In Figure 5.8, the same representation is plotted for design 2 as for design 1 in Figure 5.6. From this colour plot, it can be seen that design 2 shows reasonable linear behaviour, as with the squared prototype of design 1. However, this design shows more signs of hysteresis. As plot 5.8 is more opened up than plot 5.6b, there is a larger difference in the measured force when the applied force is decreasing than when the applied force is increasing.

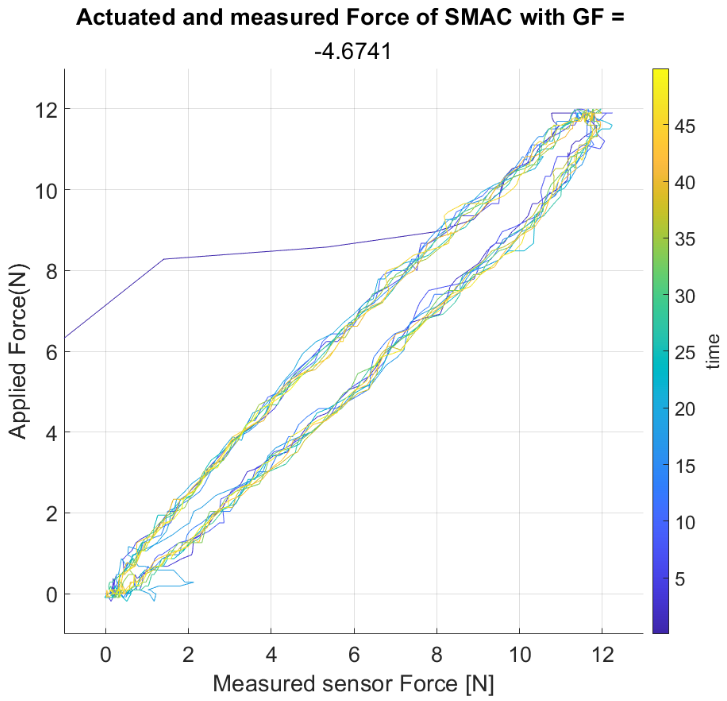

Figure 5.8: Actuated thrust force vs measured force over time on design 2

Since the SMAC actuator is able to measure not only the actuated force, but also the position of the tip of the piston in the linear actuator, Figure 5.9 shows the downward deflection of the tip of the sensor design.

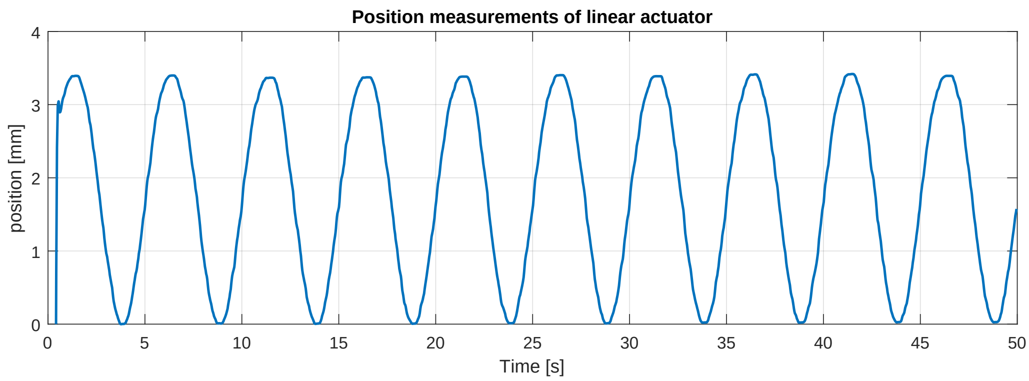

Figure 5.9: Position of the tip of the sensor during the linear actuator measurement

From Figure 5.9 the average deflection δ at a maximum force of 12 N is measured to be 3.4 mm. In the modelling section, the stiffness of the sensor is very important to the performance of the UAV. Equation 3.18 shows that the stiffness of the sensor is related by the torque τ on the sensor and the angle β.

$$K = -\frac{\tau}{\beta} \tag{3.18}$$

This angle can be calculated with the deflection of the tip of the sensor, as the length from the joint to the tip is also known. Doing so, the maximum angle at a force of 12 N is δ / L_c. Which is an angle of $\beta = 0.022$ rad. Furthermore, the maximum torque τ is defined by the cross-product between the arm L_c and the maximum force. This leaves a torque of $\tau = -1.85$ Nm. Combing the maximum angle with the maximum torque on the sensor, a stiffness of $K = 83.9$ Nm/rad is measured.

Comparing this with the designed stiffness of $K = 288.5$ Nm/rad, it is a lot lower than expected. However, the manufacturing process of a 3D printed sensor has a lot of room for errors. However, at the position where the end of the carbon fibre rod is pressed against the plastic of the sensor, there is a section that is more flexible than the section of the strain gauge. This is only the case when the thrust force of the propeller is smaller than the gravitational forces on the the motor.

As design 2 is the only design that is actually suitable to be used on the Fiberthex, more measurements have been performed to determine the characteristics of the sensor and the strain gauge. From the sinusoidal signal output, the signal-to-noise and distortion ratio (or SINAD) can be calculated. To do so, the Matlab function `snr()` is used, which compares the measured signal to a sinusoid that resembles the signal the most and then calculates the power of the noise in comparison to the power of the signal. The SINAD for this sensor is 24.61 dB.

Together with the `snr`, the function plots the Fast Fourier Transform of the signal to indicate the most important frequencies in the signal. As can be seen in Figure 5.10, the fundamental frequency is located around 0.2 Hz. Which is expected, as this is the frequency at which the linear actuator is operated.

Like Figure 5.10 shows at the top, the calculated SINAD ratio is 24.61 dB. However, in this measurement, some unusual errors have occurred that also have an influence on this calculation. An example of which can be seen at 6 s, 18 s and 22 s.

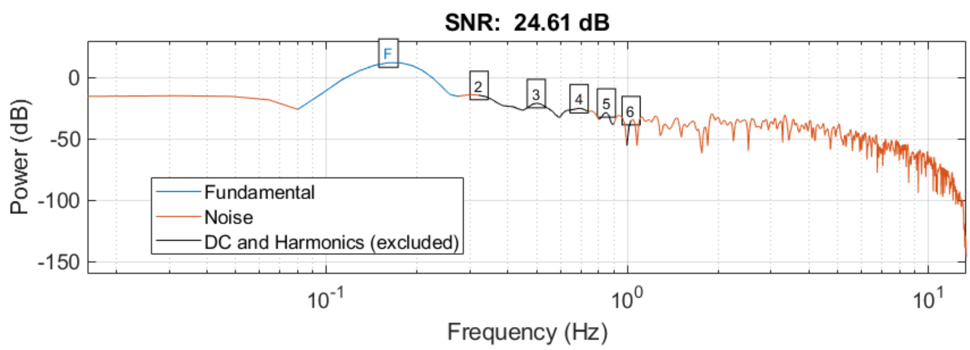

Figure 5.10: The SINAD ratio of the measurement of a 0.2 Hz sine on design 2

To validate this SINAD ratio, a measurement is performed without any actuation on the sensor. For a duration of 60 s the voltage over the Wheatstone bridge is measured. The result of this measurement is presented in Figure 5.11. The noise power is expressed in decibels and is determined by the root-mean-square of the signal.

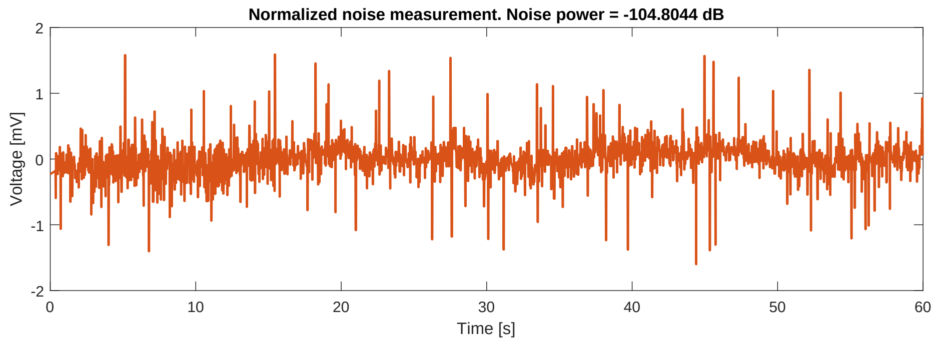

Figure 5.11: A noise measurement with Keithley 2000

As can be seen on top of the noise measurement the measured noise power is −104.8 dB. When processing the raw signal data from the sinusoidal measurement, the signal output of the Wheatstone bridge is also a sinusoidal signal that is ranged between 0 and 24.55 mV. Which has a root-mean-square of 15.4 mV or in decibels −41.7 dB.

Next, a measurement is performed to observe the response of the sensor. Figure 5.12 shows the measurement where the linear actuator starts to apply a sinusoidal force on the sensor at 0.1 Hz. After 4 periods, the period is decreased in time. The period goes through the sequence of: 10 ,8 ,6 ,4 ,2 ,1 ,0.67 ,0.5 and 0.4 seconds.

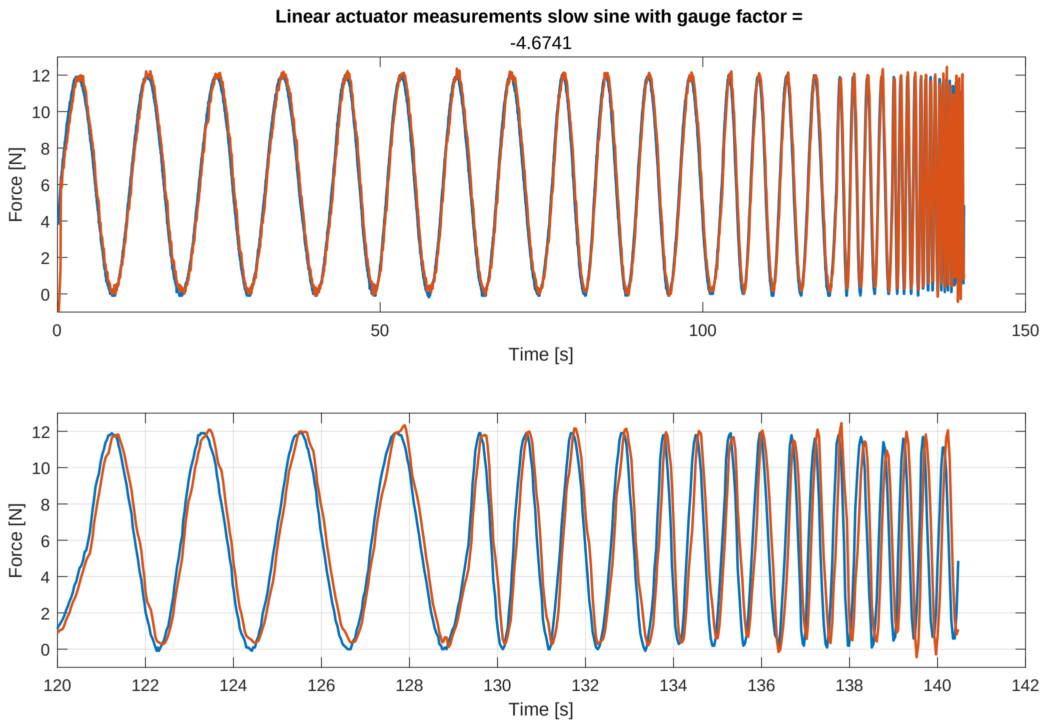

Figure 5.12: A measurement of a 0.2 Hz sine on design 2

On the bottom half of Figure 5.12, a closer look is given to the signal after 120 s. The faster the applied force changes, the more the hysteresis of the sensor becomes noticeable. Figure 5.13 shows this effect more clearly.

Another possible cause for this effect could be a delay between the actuated force and the measured force. As this is also less visible in a plot when the applied signal is slow (e.g. a sine of 0.2 Hz) and becomes more prominent with an increased bandwidth.

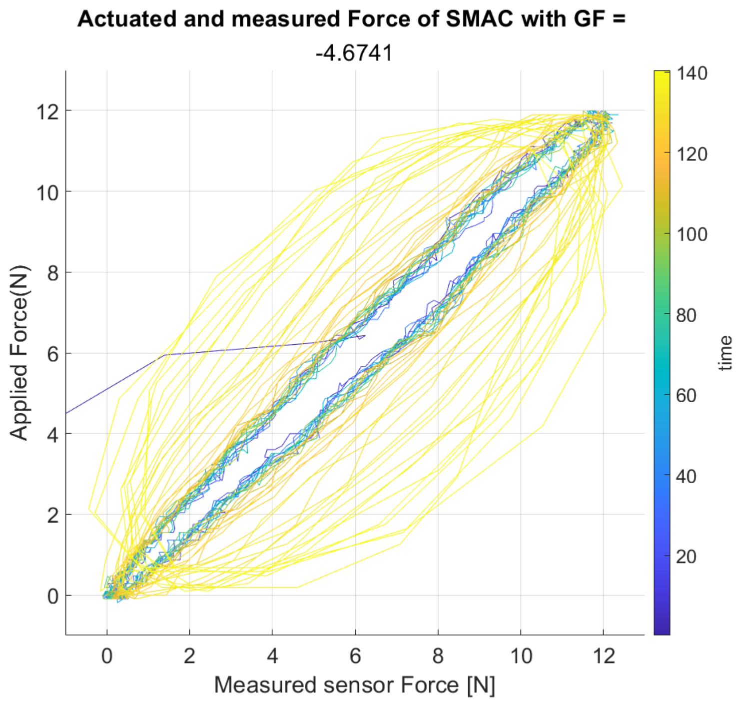

Figure 5.13: Actuated thrust force vs measured force over time on design 2

Because of the fact that the strain gauge and the beam structure are produced with plastics, the sensor is susceptible to creep. Which is the tendency of the material to relieve stress or strain within the material when it is under the influence of persistent mechanical forces. To show the effect of creep on the sensor, step measurements have been performed. The applied force starts at 2 N and every 5 seconds the force is increased with 2 N up to 12 N. When it reached 12 N, it decreases with the same step sizes to 2 N. The result of this measurement is presented in Figure 5.14.

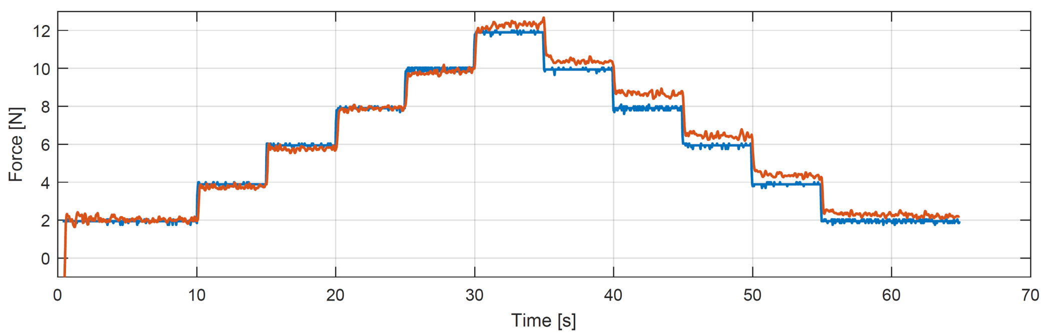

Figure 5.14: A stair measurement of design 2 from 2 to 12 N and back

During the period of time where the steps are increased, and the stresses in the material are build up, the effect of creep is negligible. However, when the applied force reaches 12 N, the creep is the sensor becomes noticeable. This is primarily caused due to the combination with the hysteresis in the sensor. It takes a while to settle at a certain value (creep) and it is a different value than the applied force (hysteresis). After the last decrement of the force, the creep in the strain gauges is clearly visible. The measured force is still dropping down to 2 N even though the applied force has not changed for 10 s.

5.3 Propeller setup

This section describes the measurement setup with a motor and a propeller attached, as seen in Figure 5.17.

Propeller characterisation

Interpreting any measurements on the sensor design with a motor and propeller attached, the propeller should first be characterised. For this characterization, the ATI mini-40 force torque sensor (ATI) is used as seen in Figure 5.15. This sensor can measure the forces in the x,y and z of its body fixed frame and the torques around these axes respectively. However, for this characterisation, only the force along the z-axis is measured. The goal in this measurement is to find the relationship between the rotational velocity of the propeller and the produced lift/thrust. The motor setup that will be used throughout this this project is a brushless direct current M3638 motor together with a 13 inch propeller with a pith of 4.5 degree pitch. The weight of this motor with the propeller attached adds up to be 120 g.

Figure 5.15: ATI mini-40 force torque sensor. (ATI)

For this characterisation, the speed of the motor is set to produce a stair-like pattern. The motor speed is set to go from 10 Hz to 90 Hz and back with 30 seconds in between every step. However, the idle speed of the motor is 16 Hz, so this is the starting and ending frequency instead of 10 Hz. The results of this measurement can be found in Figure 5.16:

With these measurements, a polynomial of $\omega$the motor speed is constructed to match the measured thrust force. A linear fit is performed with Matlab between the angular velocity of the motor ω and the measured thrust force F. The best fit turned out to be a 2nd order polynomial that is presented in equation 5.7. The computed thrust force is compared to the measured thrust force in the bottom section of Figure 5.16.

$$F(\omega) = 0.0016 \cdot \omega^2 - 0.0205 \cdot \omega + 0.24 \tag{5.7}$$

Propeller measurements

Now that the motor and propeller are characterize, the behaviour of the sensor can be observed when a motor is attached. To do so, claps (in orange in Figure 5.17) are attached to the carbon

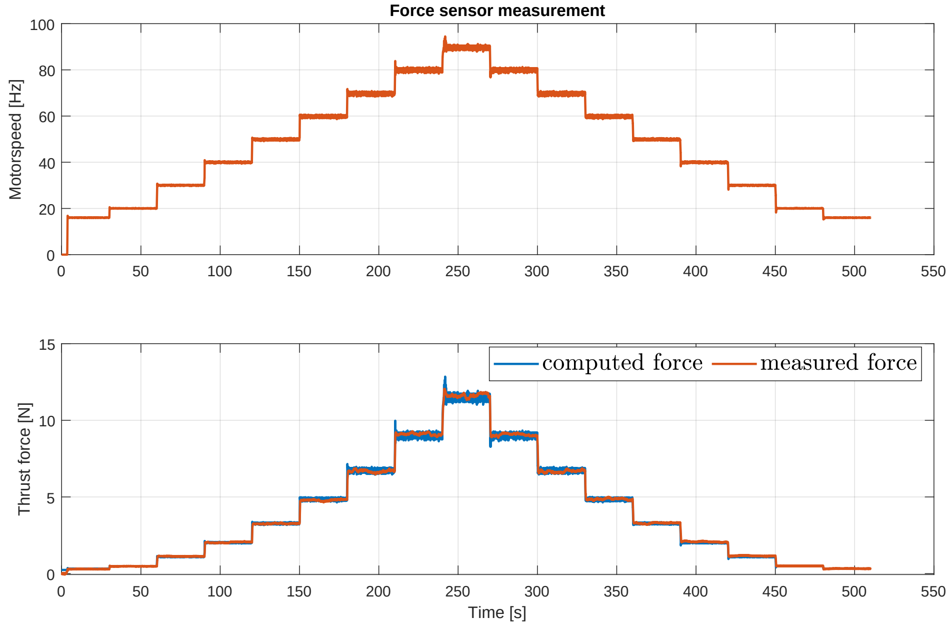

Figure 5.16: Characterization of the propeller

fibre rod to which a plastic plate is bolted. This plastic plate functions as the interface for the motor to be mounted to with two bolts. These bolts thread into the enclosure of the motor.

In order to control this motor speed ω, a Matlab script is used which communicates with a micro-controller. For this setup, a micro-controller is used that has been salvaged from an older fiberthex prototype. The motor speed is then controlled with an electronic speed controller (or ESC) that is connected to the micro-controller. This micro-controller (Openrobots) is operated through Ubuntu (Ubuntu).

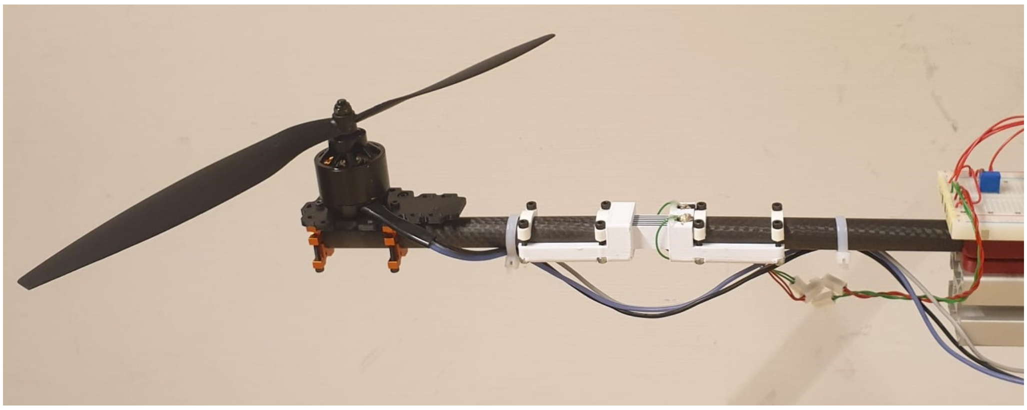

Figure 5.17: The measurement setup of sensor design 2 with a motor and propeller

Due to the fact that the Keithley multimeter is not supported on Ubuntu, a different instrument is used to acquire the sensor data. For all measurements where the motor is to be controlled, a Tie-pie HS5 oscilloscope has been used to measure the voltage over the strain gauges. This oscilloscope is also capable of providing a DC voltage. Therefore the external voltage to the Wheatstone bridge, that was provided by an arduino UNO (5 V), has now been replaced a

2 V supply from the oscilloscope. This scope also provides an analog amplification of a factor 50 and operates on a sampling rate of 10 kHz.

Now that the output voltage of the sensor is measured at high sampling rate and the weight of the motor is supported by the sensor, the natural frequency of the sensor can be determined by observing the impulse response of the sensor. Doing so will show a response similar to the signal of a mass-spring-damper system as proposed in Figure 3.6. In figure 5.18 the impulse response of the systems is visualized.

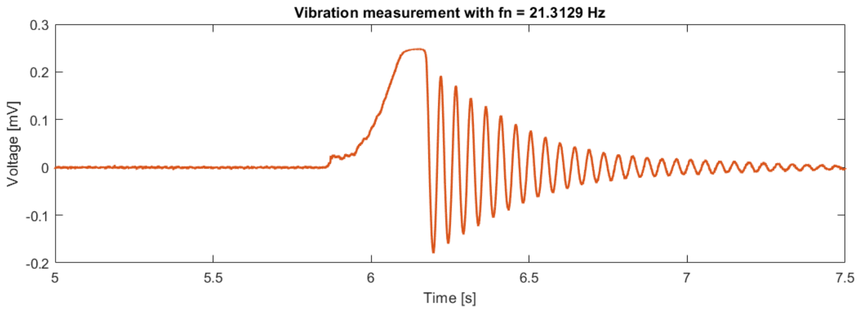

Figure 5.18: Close up on a vibration

With this response, a natural frequency of 21.3 Hz has been found. Furthermore, a logarithmic decrement of $\delta = 0.1094$ is measured from this response.

Using equation 3.25, the damping ratio of this system becomes $\zeta = 0.0174$ Next, the critical damping of the system is described as in equation 3.23, where K is the stiffness of the the rotational spring and m is the mass. As measured in section 5.2.2, the stiffness of the designed sensor is $K = 83.9$ Nm/rad. The mass is the total mass on the end of the sensor, which is $m = 0.13$ kg. This is not only the mass of motor and propeller, but also taking into consideration the mass of the attachment clips and the piece of carbon fibre rod. Combining equations 3.22, 3.23 and 3.24, the damping factor of the sensor is computed to be $c = 0.606$

To compare the behaviour of the sensor design with a propeller to the measurements of the linear actuator, the same thrust waveform is provided by the propeller. In order to provide a sinusoidal thrust force of 0.2 Hz, the motor speed has been inversely calculated to produce a clean sinusoid ranging between 0 and 11 N.

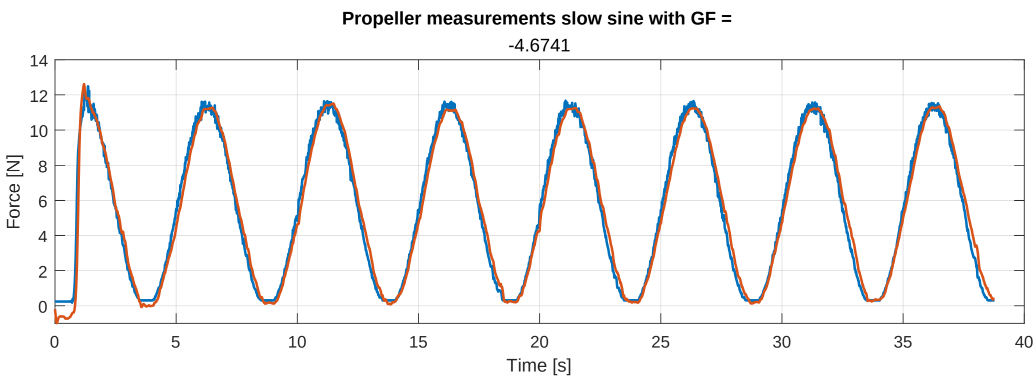

Figure 5.19: Propeller measurement with a sine of 0.2 Hz

The sensor response is visualized in Figures 5.19 and 5.20. As mentioned before, the motor speed cannot go lower than 16 Hz, therefore the bottom section of the sinusoid is cut off at a force of 0.33 N (see equation 5.7).

Comparing Figure 5.8 and 5.20, it shows that the sensor performs nearly identical in both the linear actuator setup and the propeller setup. Both figures present a similarly shallow ellipsoid shape, which indicates that the hysteresis in the sensor is not affected by the effects of the propeller.

Furthermore, the torsional effect of the rotating propeller does not seem to have an impact on the sensor measurements. This is an expected result, as both strain gauges in the sensor perceive the same amount of torque around the z-axis of the sensor design.

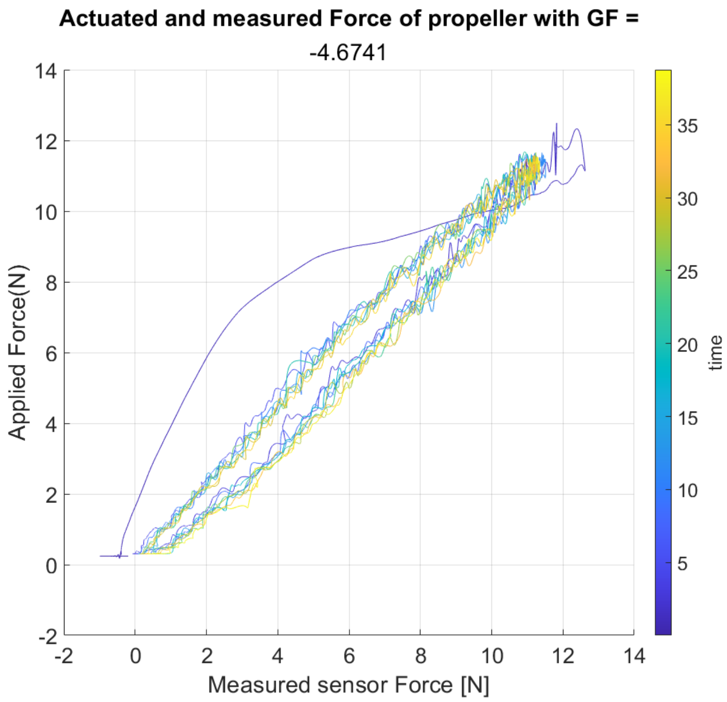

Figure 5.20: Actuated thrust force vs measured force over time

When also plotting the FFT of this measurement (Figure 5.21) with the same "snr()" function as before, an identical plot as in Figure 5.10 found. Again the fundamental frequency corresponds with the actuation frequency of 0.2 Hz and the power of the harmonics are much lower. However, this time the calculated SINAD is much higher when compared to the retrieved SINAD from the linear actuator measurement.

As mentioned, the influences of the environment have an influence on the performance of the sensor. The sensor has the potential to reach a SINAD ratio of 63.1 dB, therefore it is no surprise that the quality of this measurement is slightly higher than the measurements with the linear actuator.

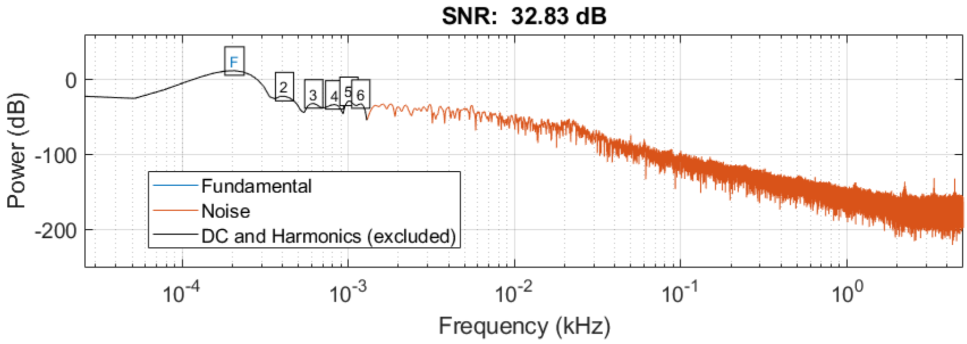

Figure 5.21: The SINAD ratio of the measurement with propeller

With the propeller attached to the sensor, the same measurement is performed where the period of the sinusoidal thrust input is decreased after 4 periods. Figure 5.22 shows the results of this measurement. From 0 to 35 s, the signal output gives a similar result to the same measurement with the linear actuator in Figure 5.12. The sensor seems to read the actuated force accurately. However, after 35 seconds, the sensor readings show a higher sensor reading after the increase to a frequency of 1 Hz, visible in the lower section of Figure 5.22. It also becomes clear that it is at this frequency, the motor seems to have trouble reaching the 12 N that it was able to provide at lower frequencies. This shows that the bandwidth of the sensor is larger than the bandwidth of the motor. Observing the signal after 40 seconds, the offset in measured force becomes larger. In Figure 5.23, this effect is especially visible once the plot turns green (which is after 35 s). This might be caused by the fact that the thrust does not reach a force of 0 N anymore, which releases the sensor from any strain. This introduces the creep into the sensor, as the stresses in the material are not released anymore. Once the measurement is finished, the signal slowly approaches 0 N.

Unfortunately, due to technical difficulties and time constraints, no stair measurements have been performed that delivered a quality that was good enough to analyse and draw conclusion from. These issues have been caused by interface issues between the strain gauge and the oscilloscope.

5.4 Conclusion

This chapter presented the characterisation of the produced sensor designs. An explanation has been given on the measurement setup. Experiments have been performed with a linear actuator on both sensor designs. Design 2 has also been subject to measurements with a motor and propeller attached to the arm of the sensor. Both sensor designs showed great promise to be integrated in a multirotor UAV. However, is also showed that the connection interface between the strain gauges and the wires needs to be extremely secure to be able to perform measurements with the sensor designs.

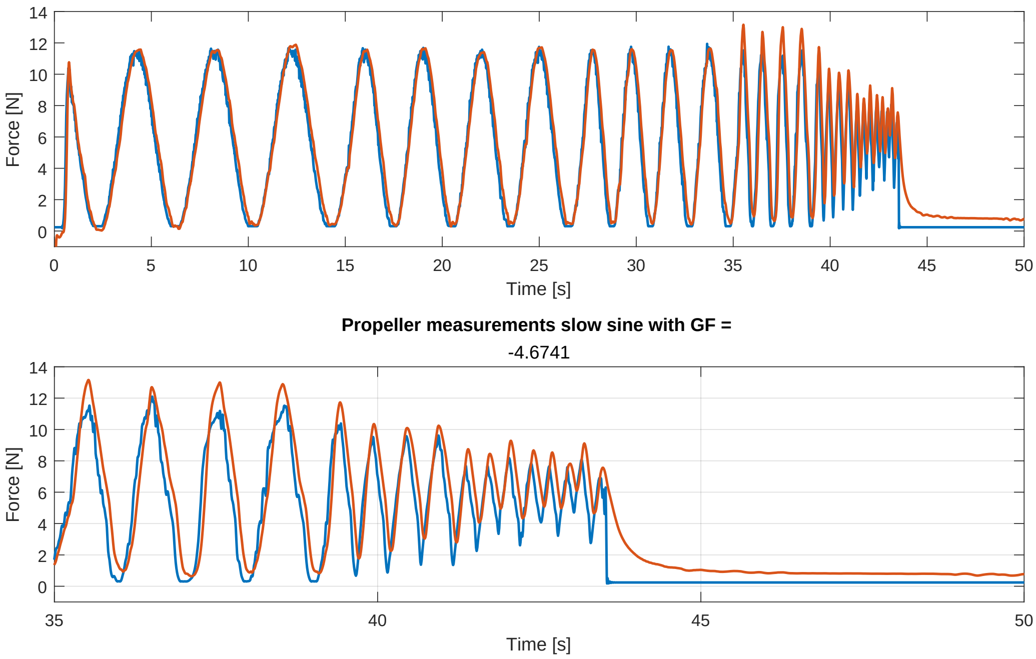

Figure 5.22: Propeller measurement of a sine with increasing frequency

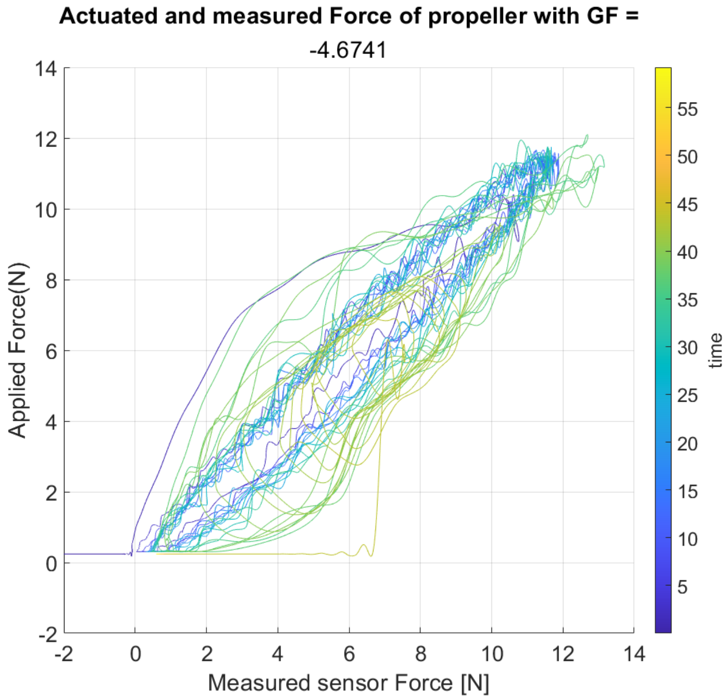

Figure 5.23: Actuated thrust force vs measured force over time of sine with increasing frequency

6 Simulations

In this chapter, the simulation results of the rigid and the flexible model are visualized and analysed.

6.1 Introduction

With the use of the models that have been created in sections3.4.1 and 3.4.2 together with the characterization of the sensors, resembling models have been created to research the behaviour of flexibility in a UAV. For the flight simulations, the 2 models are considered that have been modelled in section 3.4:

1. The rigid UAV model: this is the model as described in section 3.4.1. It is modelled as a single rigid body with two motors attached on either side. The body of this model is designed as a solid beam.

2. The flexible UAV model based on sensor design 2 as in section 3.4.2. This model has the characteristics of the produced sensor design. The sensor is modelled as a rotational spring-damper system, creating 3 rigid bodies that are connected to each other with the sensor design. On the two outer bodies, the propellers are modelled at the free end of the body, as seen in Figure 3.8.

The parameters of both these systems have been listed in table 6.1. These have been obtained through estimation and the characterization of the sensor design. In this table, the total width of the body is twice the arm length as determined in section 4. The location of the joint in the flexible model has been determined to through the fact that the sensor/flexible section (19 mm long) has been placed exactly in the middle of one arm. The inertia tensor of the bodies in the models have been derived with equation 6.1:

$$I = \frac{1}{12} m \left(h^2 + w^2\right) \tag{6.1}$$

Where m is the mass of the body, h is the height and w is the width. Furthermore, to make model less complicated, the computation of the thrust has been taken as in equation 3.26 instead of the obtained equation 5.7 in section 5.3.

Parameters	Rigid	Flexible	SI-units
Mass body	0.46	0.2	kg
Mass per arm	-	0.13	kg
Gravitational force 9.81	9.81	9.81	$\mathrm{m\,s^{-2}}$
Inertia tensor total body	0.0146	0.0016	$\mathrm{m\,s^{-2}}$
Inertia tensor per arm	-	0.00026	$\mathrm{m\,s^{-2}}$
Spring constant - joint	-	83.9	$\mathrm{N\,m\,rad^{-1}}$
Damping factor - joint	-	0.606	-
Total width body	616	616	mm
Distance hinge-motor	-	154.2	mm
Distance com-hinge	-	153.8	mm
Propeller lift coefficient	$12.5 \cdot 10^{-4}$	$12.5 \cdot 10^{-4}$	-

Table 6.1: The system parameters of each model

The models of the rigid UAV and the UAV with flexible hinges are both observed while following a trajectory. In Figure 6.1, these trajectories have been visualized. In each of the trajectories, the UAV starts at a hovering state then moves to a desired position. These trajectories are as follows:

- **Trajectory 1:** The UAV moves 1 meter up from its initial hovering position. Due to the symmetric design of the models, both UAVs should be able to do so without any rotation required.
- **Trajectory 2:** The UAV moves 1 meter to the right of its initial hovering position. This is a more advanced move for both models, as the UAVs need to rotate to create a force along the x-axis.
- **Trajectory 3:** The UAV moves 1 meter up and to the right to create a diagonal movement from its initial hovering position. Similar to the second trajectory, this movement also requires the UAV to rotate to move in the horizontal plane.

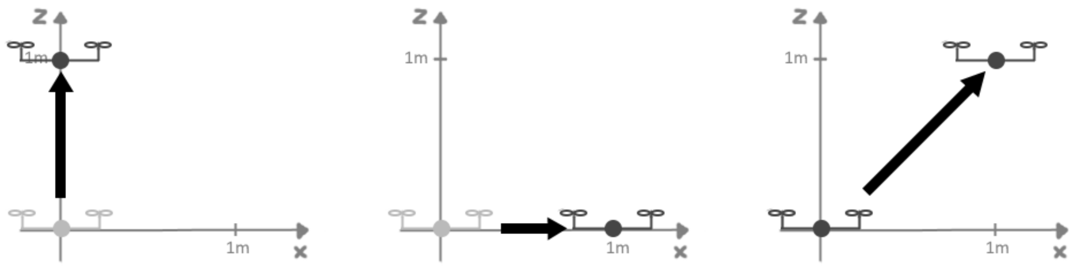

(a) Trajectory 1: A translation along the z-axis.

(b) Trajectory 2: A translation along the x-axis.

(c) Trajectory 3: A translation along the both the x- and z-axis.

Figure 6.1: The three simulation trajectories.

In order to visualize the simulation data, the position error between the created trajectories and their actual flight paths will be plotted. Furthermore, the difference between the flight path of the flexible UAV is compared to the flight path of the rigid UAV. Additionally, the error in the applied thrust force of the flexible model with respect to the rigid model is plotted to analyse the behaviour of this vehicle.

These errors are computed as relative errors and will be expressed in percentages. This means that the position error is calculated as $100 * (p_{\text{f}} - p_{\text{traj}})/p_{\text{traj}}$. Where p_{f} is the position of the flexible model and p_{traj} is the position of the trajectory at that same time instance. However, when the initial position of the the UAV is at (0,0), this error becomes infinitely high as there is a division by zero. Since all trajectories only involve movement in the positive direction of the x and z-axis, the initial hovering position of the UAVs is set be at (1,1).

6.2 Flight stability

This section shows the flight simulations of the error in flight paths between the rigid model and the flexible models. As there is very little room in the legends of the plots for proper signal denotation, abbreviations have been used to distinguish the different signal. An explanation on these abbreviations is presented in table 6.2.

Abbreviation	Elaboration
ex-r	error in x, for the rigid model
ez-r	error in z, for the rigid model
ex-f	error in x, for the flexible model
ez-f	error in z, for the flexible model
ex-fr	error in x, for the flexible model w.r.t. the rigid model
ez-fr	error in z, for the flexible model w.r.t. the rigid model
ef1-fr	error in thrust force left, for the flexible model w.r.t. the rigid model
ef2-fr	error in thrust force right, for the flexible model w.r.t. the rigid model

Table 6.2: Elaboration on the legends of the simulation plots.

Trajectory 1

Comparing the flight of the models to their trajectories in figure 6.2, it can be seen that the rigid model follows the trajectory closely. Is has a slight offset from the trajectory in z, but the controller is able to slowly compensate this behaviour. The flexible model has a less consistent error in z when compared to the rigid model. This is expected, as there is a mass-spring-damper system involved, which causes a delay in the displacement of the center of mass with respect to the position of the motors. Regarding the error in x, both models have a negligible error in the order of 10^{-8}%.

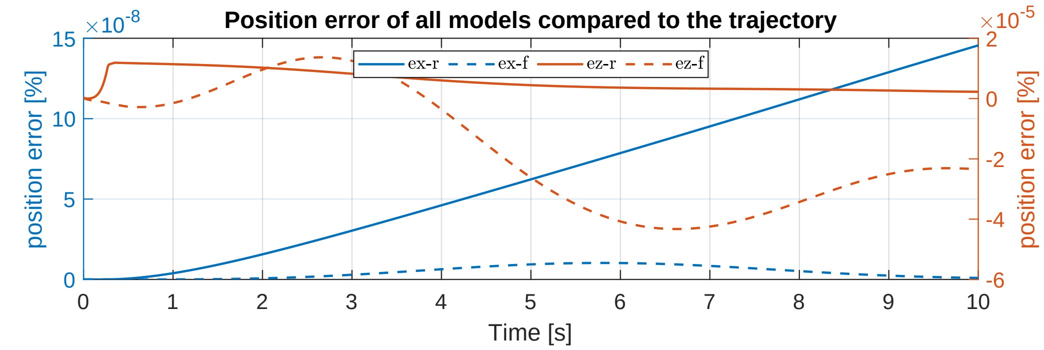

Figure 6.2: Position errors between the models and their trajectories

Due to the fact that the rigid model had very little errors with respect to the trajectory, the relative position errors between the Figure 6.3 shows the same information as in plot 6.2.

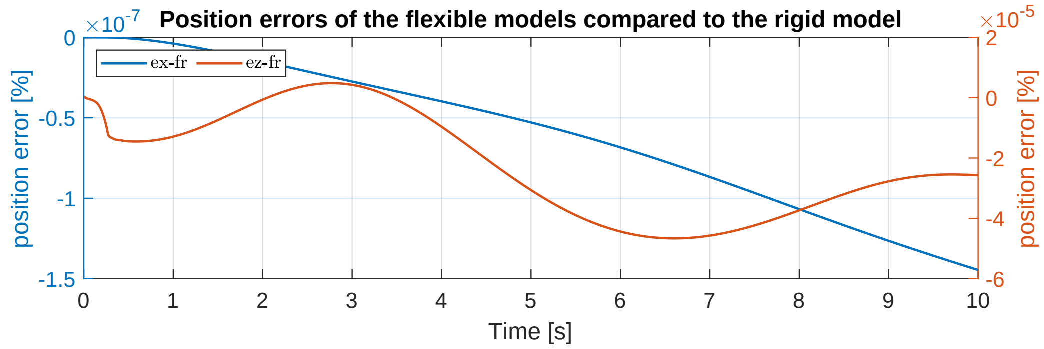

Figure 6.3: Position errors of the flexible model with respect the rigid model - trajectory 1

When comparing the thrust applied by the flexible model to the rigid model in Figure 6.4, there is only an error of nearly $2 \cdot 10^{-4}$%. The error in both motors is practically identical. Which is as expected, as the z-axis of world frame $\mathscr{F}_W$ and the z-axis of the body frame $\mathscr{F}_B$ are aligned in the initial hovering state, adding that both UAVs are symmetric around this axis.

From Figure 6.4, it can be seen that the flexible model requires a consistently larger thrust than the rigid model. This is expected, as the thrust of the motor is slightly pointed inwards, which causes the motors to produce less upward force than when the motors are exactly aligned with the z-axis of the body frame $\mathscr{F}_W$.

Remarkable is that there is a small upward spike in the thrust error in the first 0.5 s of the measurement, even though there is no spike in the position error w.r.t trajectory for the flexible model. An explanation for this is that there is a delay between the applied thrust and the upward motion caused by the flexibility in the arms of the UAV. Therefore the controller tries to apply more thrust without seeing results on the position of the body of the UAV.

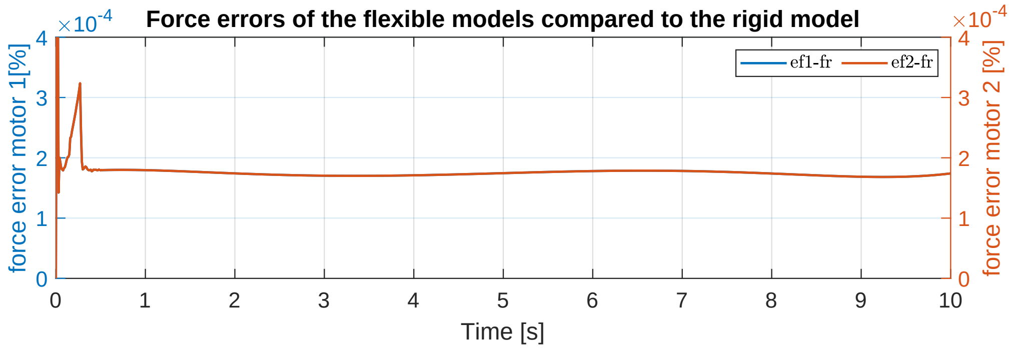

Figure 6.4: Thrust force errors of the flexible model with respect the rigid model - trajectory 1

Trajectory 2

For trajectory 2, both models show similar behaviour when it comes to the position errors with respect to the trajectory. Compared to the trajectory errors in Figure 6.2, the errors are much larger for the second trajectory in Figure 6.5. This is reasonable, due to the fact that the UAVs are under-actuated and cannot produce any immediate force along the x-axis. Because of this under actuation, the models need to rotate in order to produce any horizontal forces, resulting in a position delay.

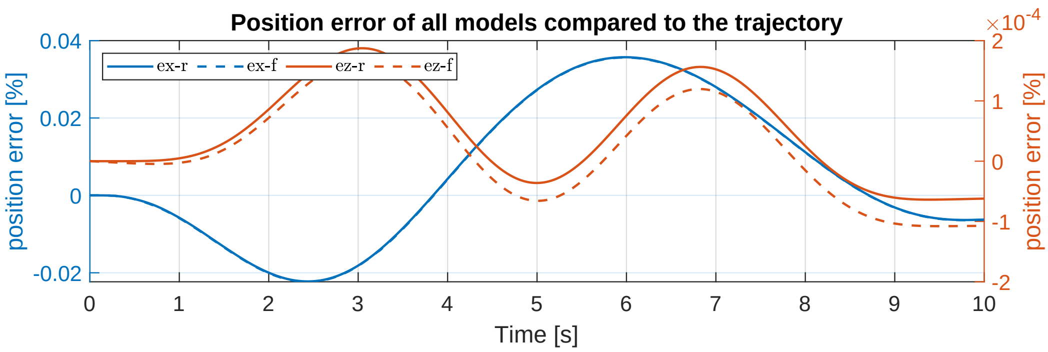

Figure 6.5: Position errors between the models and their trajectories

For plot 6.6, small vibrations in the position error in x of the flexible model w.r.t the rigid model become visible. As these are not visible in the position error with respect to the trajectory, it is most likely that these are caused by the controller that is dealing with the delays in mechanical system of the UAV. Since the sensor design has a natural frequency of 21.3 Hz and the model is based upon a mass-spring-damper system with the same characteristics.

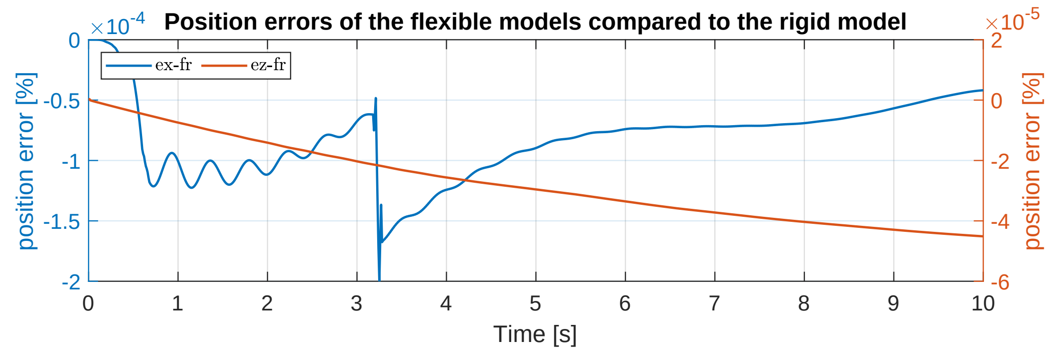

Figure 6.6: Position errors of the flexible model with respect the rigid model - trajectory 2

For the force error in this trajectory, it can be seen that the error in motor 1 is inverted in motor 2, making the absolute error the same. As motor 1 and 2 are the left and right motor respectively, it is interesting to see that the left motor produces less thrust and the right motor more thrust in the flexible model when compared to the rigid model. This is caused by the orientation of the motors in the flexible design. As these are already tilted slightly inwards when hovering, the adjustments for rotations are different. The combination of the rotation and the objective to still compensate for gravitational forces creates this behaviour.

The 3 spikes within 1 s of the simulation are the feedback of the controller to stop the increasing position error in x in the first second of plot 6.6. When examining Figure 6.7 closely, it can be confirmed that the oscillations in the position error plots are indeed caused by the controller. Since the thrust force is the controllers input to the system dynamics.

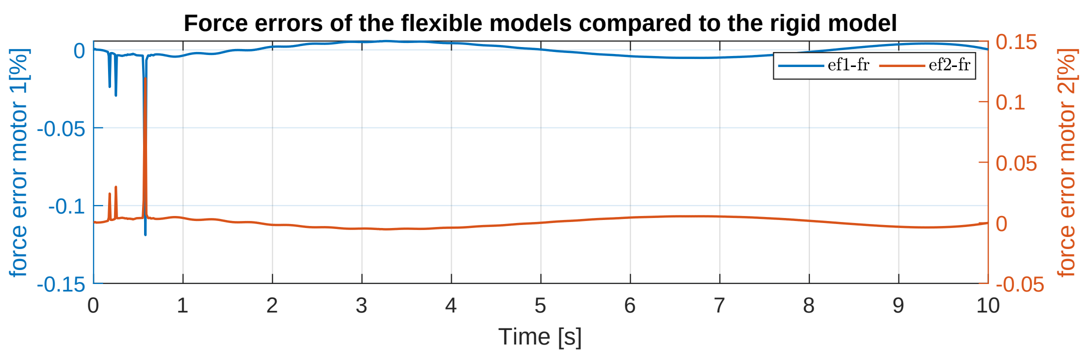

Figure 6.7: Thrust force errors of the flexible model with respect the rigid model - trajectory 2

Trajectory 3

Figure 6.8 shows the trajectory errors of a diagonal motion up and to the right, going from (1,1) to (2,2) in the world frame $\mathscr{F}_W$. It can be seen that both models show a similar amount of error to the trajectory in both x and z. After 2.5 s, a distinct change in the trajectory errors of the flexible model is visible. After which it starts to follow the curvature of the rigid UAV.

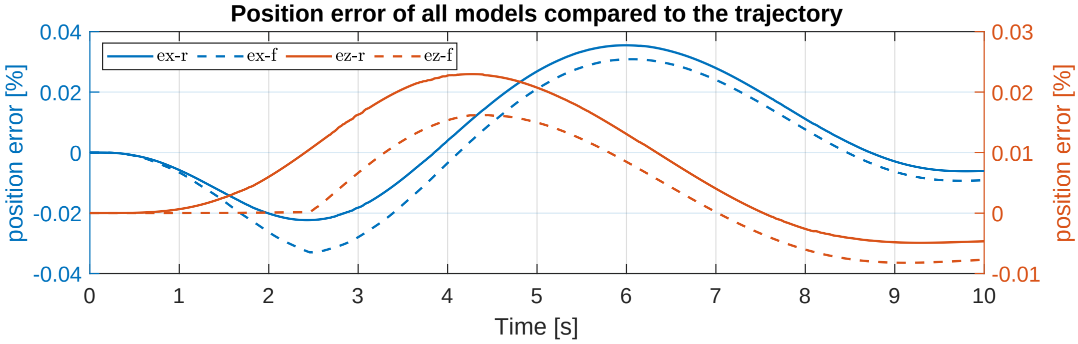

Figure 6.8: Position errors between the models and their trajectories

Figure 6.9 shows this abrupt change in the position error clearer between the models. In contrary to trajectory 2, there are no oscillations visible in the position error of the flexible model. However, in Figure 6.10 it is still visible that the controller shows signs of oscillations. These are gradually dissipating in the signal when the becomes smaller.

As can be seen in the force error plot of this trajectory, the instance of the abrupt change is caused by a spike in the thrust force. This spike is positive for the left motor and negative for the right motor. This shows that the controller used this spike to correct for the drifting trajectory error in x. Unfortunately, this correction also introduced a trajectory error in z, as can be seen in Figure 6.8. The thrust force also shows more spike within the first second of the simulation, but the origin of these are unknown.

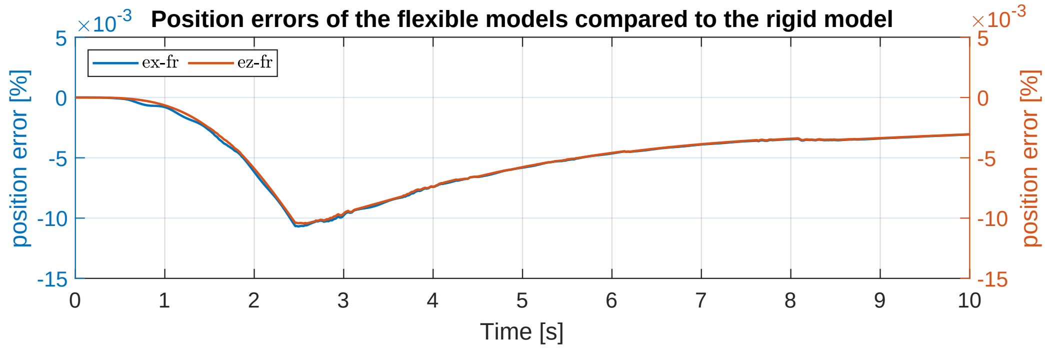

Figure 6.9: Position errors of the flexible model with respect the rigid model - trajectory 3

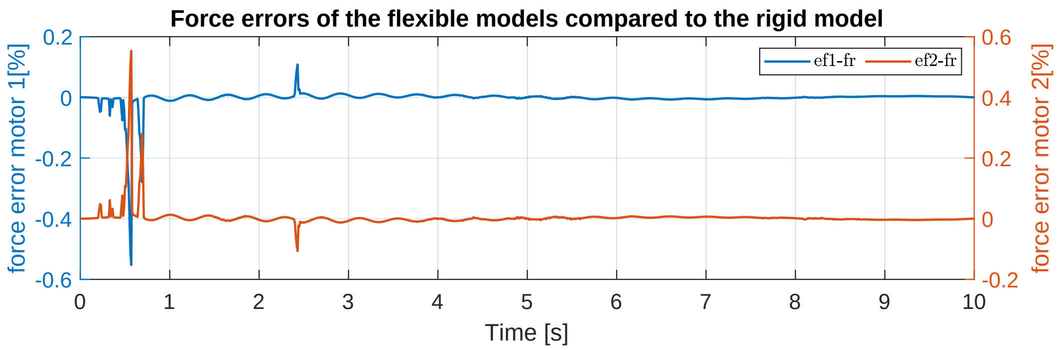

Figure 6.10: Thrust force errors of the flexible model with respect the rigid model - trajectory 3

In these simulations, it has become clear that the controller is capable of controlling the UAV with integrated flexible sensors as is designed in this thesis. The simulations of this flexible model show that the flexible model requires more thrust than the rigid UAV, but the force errors are less than 0.5 % and in the case of only vertical manoeuvres as small as 3×10^{-4} % of the thrust that a rigid UAV is required. The controller also shows signs of oscillations when dealing with the mass-spring-damper system in the UAV, but it is able to suppress these oscillations over time.

To have a look at the limits of the controller, more simulations have been performed in which the stiffness and the damping in the joints have been adjusted. These simulations have been performed along trajectory 3, as this is the trajectory where the largest errors occur in both x and z, see Figure 6.8. Figure 6.11 shows the position states of a simulation with the flexible UAV where the stiffness is lowered to $K = 0.4\,\mathrm{N\,m\,rad^{-1}}$, which is the lowest value before failure. The damping factor in this plot is unchanged at $c = 0.606$.In this plot, it can be seen that the oscillation in the position states are extremely large and seem to be just stable enough. The frequency of the oscillation is also much lower than the oscillations in the sensor model.

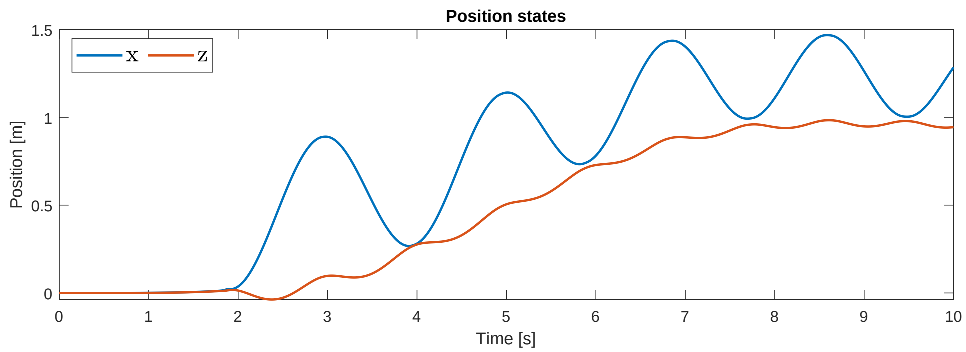

Figure 6.11: The flexible UAV with the lowest stiffness before failure.

Figure 6.12 shows a similar simulation, but with a stiffness of $K = 83.9\,\mathrm{N\,m\,rad^{-1}}$ (similar to the sensor model) and with a damping that is lowered to $c = 0.18$. This is the lowest damping factor before the system could recover itself. As with in plot 6.11, oscillations are visible in the position states. However, the frequency of these oscillations is much higher than the oscillations in the sensor model. As expected when lowering the damping factor, the system is underdamped and marginally stable. It could even be said that this system is in fact unstable, as the position state in x does not seem to converge.

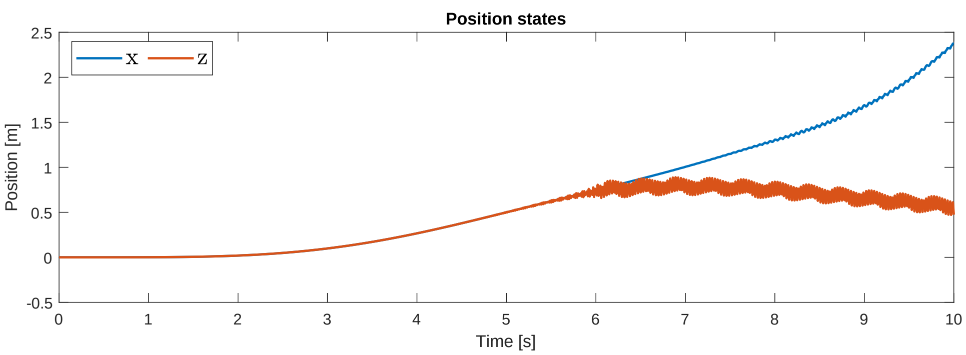

Figure 6.12: The flexible UAV with the lowest damping before failure.

6.3 Observability

In section 3.1.1, the force-strain relationship in the sensor is based upon the Euler-Bernoulli (7) equation 3.2. In order to determine the distribution of the strain throughout the beam, the condition has been made that one end of the beam is fixed and the other end of the sensor is free to move, creating a cantilever beam. Doing so, any stress or strain caused by a force upon the free end of the beam are distributed along the beam. When designing the sensor for a multirotor, this same assumption is made that one side of the sensor is fixed, while the other side of the sensor has the thrust force acting upon. This is also used in the measurements setups for the characterization with both the linear actuator and the propeller, where one side of the sensor is clamped, see Figures 5.3 and 5.17.

When the UAV is flying, there is no ground that sensors are connected to. This means that there is no guarantee that the strain produced by one propeller is only distributed over the arm on that side of the propeller.

Equation 3.13a shows the behaviour of the joint angles with respect to the applied force when one side of the sensor is fixed. It can be seen that the relationship between the applied force F and the joint angle β is linear, as all other elements in this equation are parameters.

Figures 6.13, 6.14 and 6.15 show in blue the exerted force by the propeller and in orange the behaviour of the corresponding joint angle β for each motor and each trajectory:

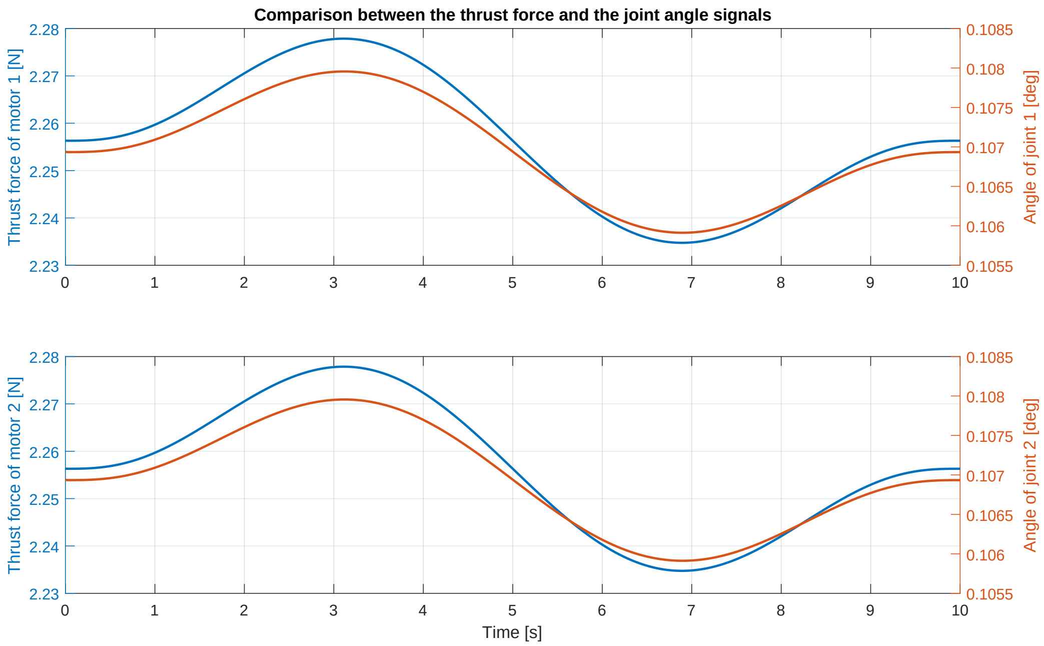

Figure 6.13: Model 2, Trajectory 1 - Thrust forces compared to their corresponding joint angles.

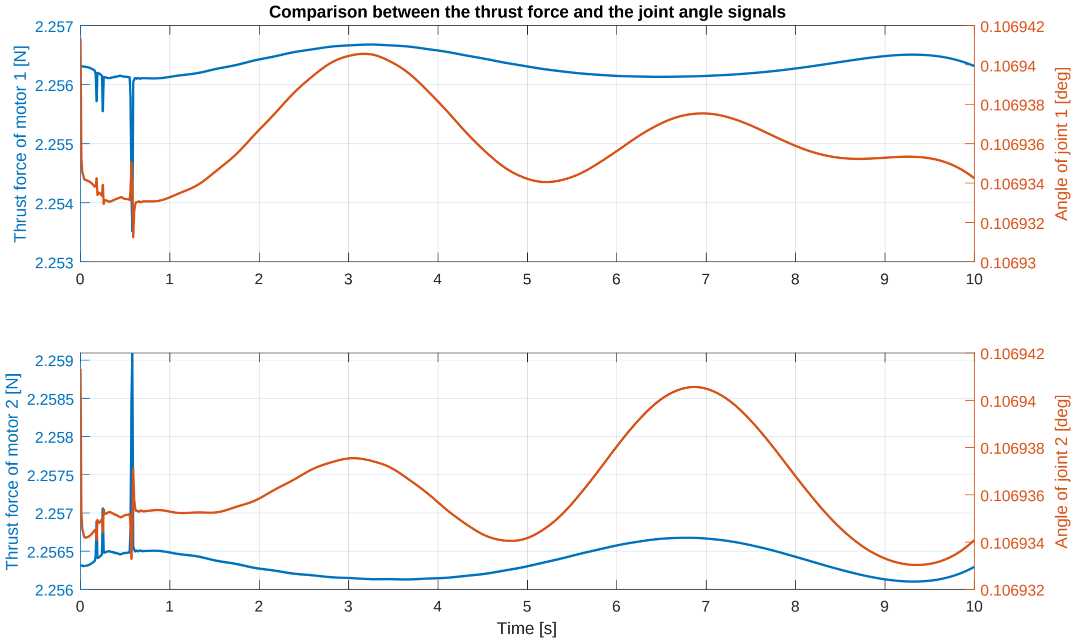

Figure 6.14: Model 2, Trajectory 2 - Thrust forces compared to their corresponding joint angles.

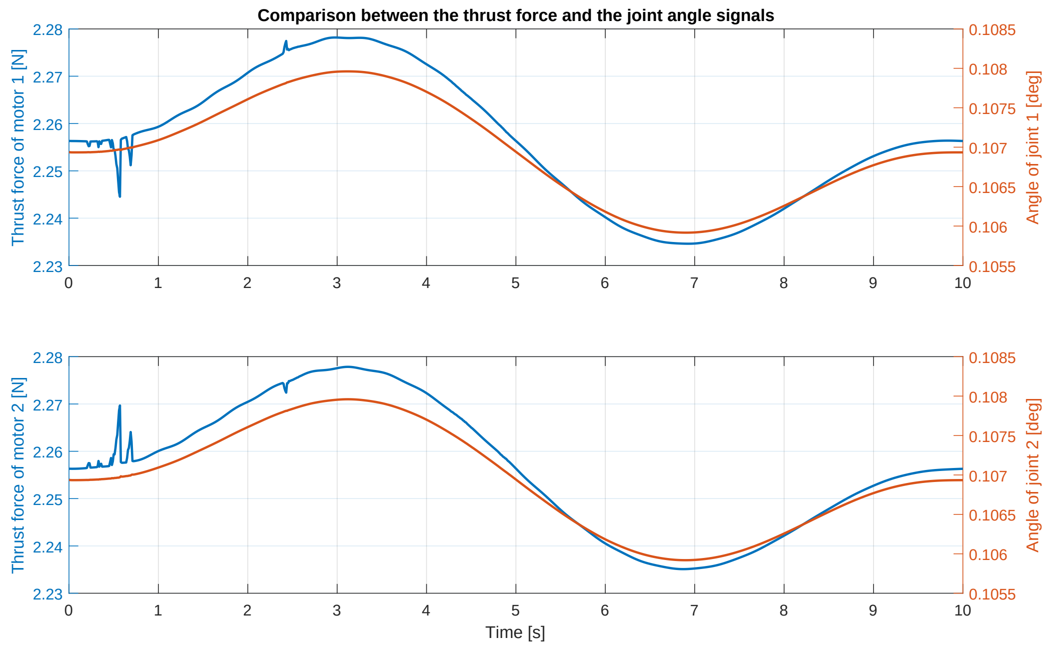

Figure 6.15: Model 2, Trajectory 3 - Thrust forces compared to their corresponding joint angles.

When observing the applied forces and their corresponding joint angles of trajectories 1 and 3, this relationship seems indeed to be linear. These trajectories show a sinusoidal type of signal for the forces and the joint angle follows this signal very carefully, with the peaks and the valleys lined up with the applied forces.

However, when observing the signals from trajectory 2 in Figure 6.14, this same linearity does not hold. As trajectory 2 is the movement along the positive side of the x-axis, the UAV has to rotate to move horizontally. This is also visible in the force signals. To create a force vector to the right, motor 1 a slightly higher force than motor 2. Then to make the UAV stop at (1,0), motor 2 produces a larger thrust than motor 1. These are the 2 peaks that are visible in the plot. Additionally, spikes are visible in all signals within the first second of the simulation. These spikes are in the opposite direction when comparing them between the two sides of the UAV. These spikes are caused by an error in the controller and will therefore not be discussed in this section on the observability.

When looking at the signal of the joints, the peaks of the applied forces do not seem to match with the peaks that are visible in the joint angles. Only at the largest peak in the applied force, a peak is visible in the in the corresponding joint angle.

This shows that the applied thrust force can not be measured through linear computations.

6.3.1 Empirical findings

As an exploration on the thrust measurements of the flexible model simulations, the sum of the forces has been plotted to see if the sum of the forces does indeed carry the total weight of the motors. And as the correlation between the thrust and the joint angle is linear when one side of the sensor is clamped, the sum of the joint angle has also been plotted. In addition, out of curiosity, the difference in forces and the difference in joint angles have also been plotted for each trajectory. These plots are shown in Figures 6.16, 6.17 and 6.18.

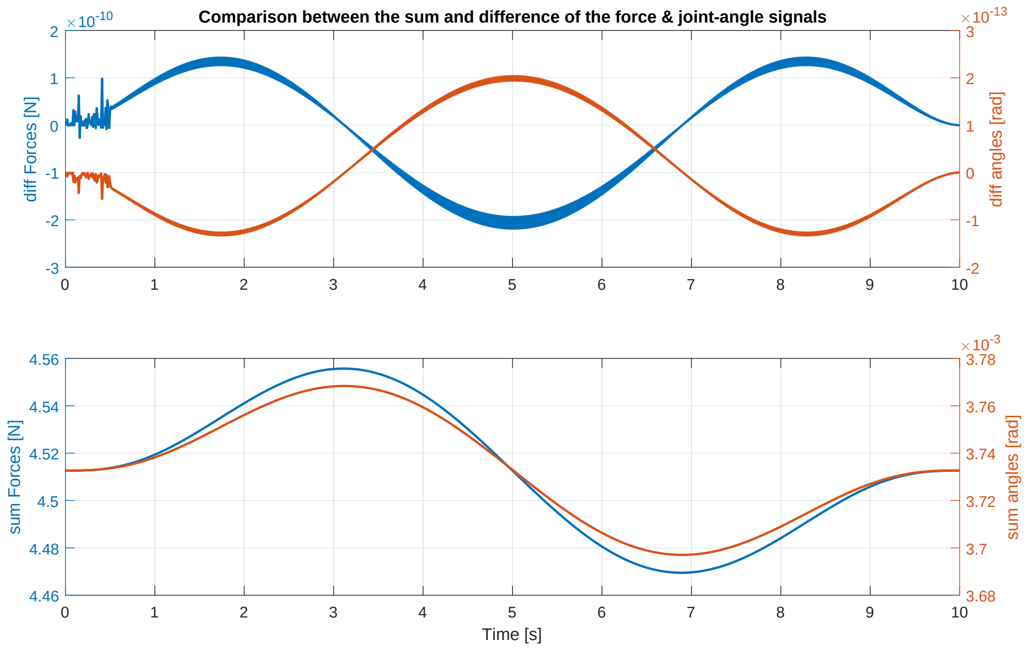

Figure 6.16: Empirical observations trajectory 1

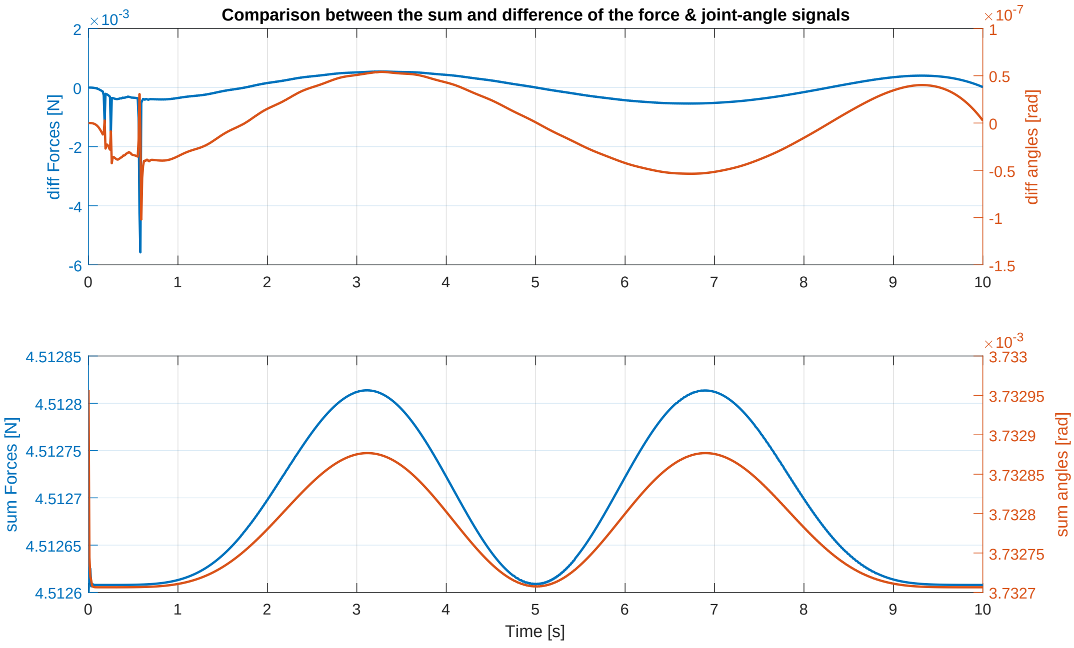

Figure 6.17: Empirical observations trajectory 2

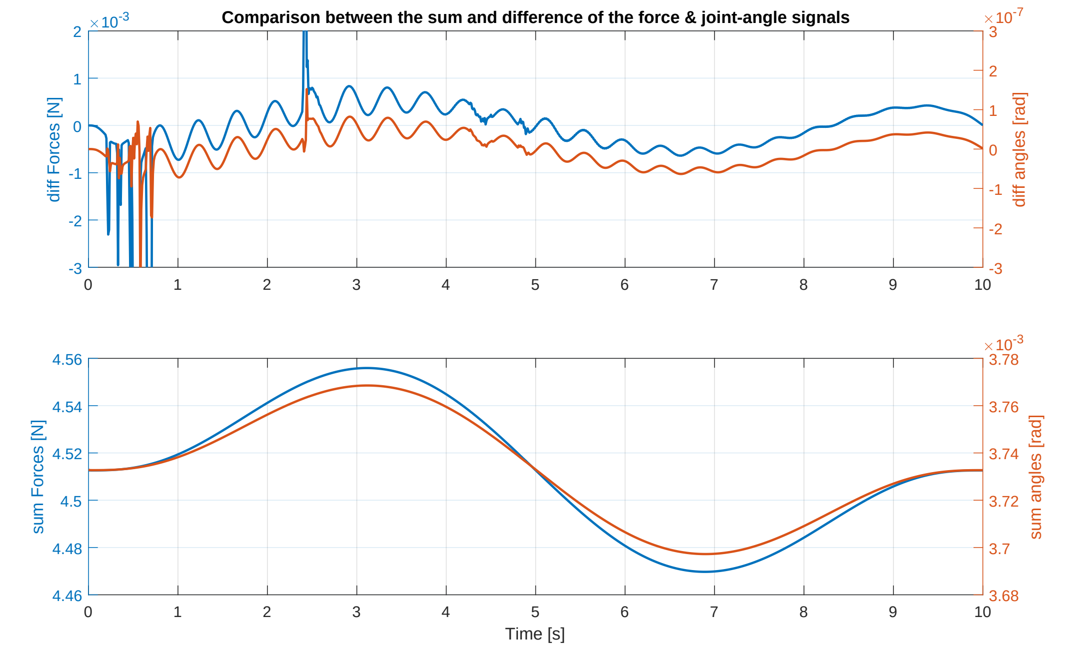

Figure 6.18: Empirical observations trajectory 3

Through this empirical research, it can be seen that the sum of the forces indeed starts and ends near $0.46 \cdot 9.81 = 4.5126$ N, which is the needed force to compensate the gravitational force on the UAV. Especially in Figure 6.17 it can be seen that the required force is slightly higher than 4.5126 N. This is an expected result, since the motors have a small angle inwards, which requires the model to produce a larger thrust.

Especially for trajectory 2, it is interesting to observe that with the computations of summing and taking the difference in the signals, a linear relationship is visible between the computed signals of the forces and joint angles. This same relationship is also visible for trajectories 1 and 3. Even though the difference in thrust forces and the difference in joint angles in Figure 6.16 give an inverted signal response, the power of the signals are small enough to be neglected and render them as 0 N and 0 rad.

With the evidence that the summation of the joint angles has a linear relationship to the summation of the thrust forces and the same holds for subtracting the signals, equations 6.2 and 6.3 should hold:

$$F_1 + F_2 = f_\text{F} \quad \& \quad \beta_1 + \beta_2 = f_\beta \quad \text{where} \quad f_\text{F} = a \cdot f_\beta + b \tag{6.2}$$

$$F_1 - F_2 = g_\text{F} \quad \& \quad \beta_1 - \beta_2 = g_\beta \quad \text{where} \quad g_\text{F} = c \cdot g_\beta + d \tag{6.3}$$

Which lead to:

$$\begin{aligned} F_1 + F_2 &= a\beta_1 + a\beta_2 + b \\ F_1 - F_2 &= c\beta_1 - c\beta_2 + d \end{aligned} \tag{6.4}$$

In these equations, f and g are functions that indicate the sum and the difference of the signals respectively; a, b, c and d are scalars; and F and β represent the force of the motors and the joint angles.

As the functions in 6.4 are 2 equations and 2 unknown variables, it should be possible to compute the unknown thrust forces from the measured joint angles with the equations in 6.5:

$$\begin{aligned} F_1 &= \frac{a+c}{2} \cdot \beta_1 + \frac{a-c}{2} \cdot \beta_2 + \frac{b+d}{2} \\ F_2 &= \frac{a-c}{2} \cdot \beta_1 + \frac{a+c}{2} \cdot \beta_2 + \frac{b-d}{2} \end{aligned} \tag{6.5}$$

As it was in Figure 6.14 that the joint angles did not present a linear relationship to the thrust forces, it is with this trajectory that the values of a and b have been determined. With a linear fit between the signals form Figure 6.17 the values of the parameters have been found as stated below:

$$\begin{aligned} a &= 1.19 \cdot 10^3 \\ b &= 5.28 \cdot 10^{-2} \\ c &= 9.97 \cdot 10^3 \\ d &= -1.29 \cdot 10^{-5} \end{aligned} \tag{6.6}$$

Combining the parameters in 6.6 with the equations in 6.5 the thrust forces are computed through the joint angles. In Figures 6.19, 6.20 and 6.21 these computed forces are compared with the force that is actually applied by the controller. This comparison is plotted as a relative error.

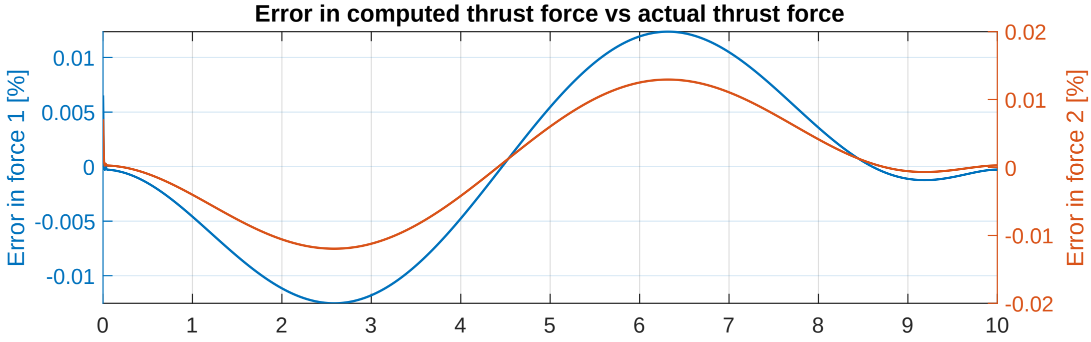

Figure 6.19: Error between the computed force and the actuated force on trajectory 1

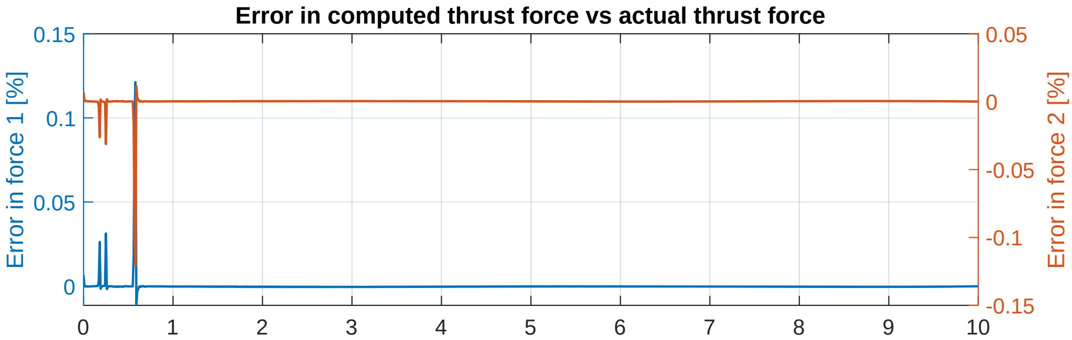

Figure 6.20: Error between the computed force and the actuated force on trajectory 2

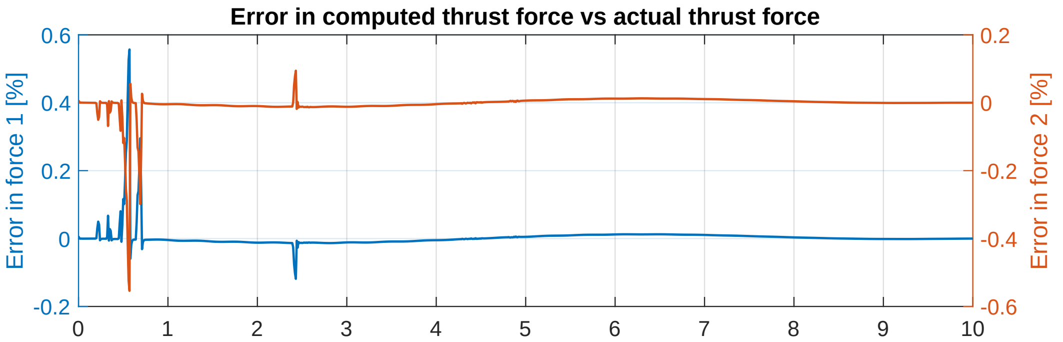

Figure 6.21: Error between the computed force and the actuated force on trajectory 3

From these plots, is can be observed that the computed force is within an accuracy of 0.5 % of the applied thrust force. This value is much lower for the scenarios with no abrupt behaviour from the controller. The maximum error of 0.5 % is caused by the thrust spikes in the simulation that are not perceived as intense in the joint angle, as can be seen in Figure 6.15. However, due to the fact that this is an empirical finding and the parameters for the computation have been determined on simulations this method does not produce a robust method of measuring the thrust through the joint angles.

When looking into the systems equations of dynamics of the flexible UAV it is structured as shown in equation 3.42:

$$\ddot{\mathbf{q}} = \mathbf{M}(\mathbf{q})^{-1}\left(-\mathbf{C}(\mathbf{q},\dot{\mathbf{q}}) - \mathbf{G}(\mathbf{q}) + \mathbf{W}(\mathbf{q},\mathbf{u}) + \mathbf{D}(\dot{\mathbf{q}})\right) \tag{3.42}$$

This equation shows the evolution of the states in $\boldsymbol{q}$, which are the position $\boldsymbol{p}$, the orientation ϕ and the angle of the joints $\boldsymbol{\beta}$. This means that the evolution of $\boldsymbol{\beta}$ is described in the last 2 elements of $\ddot{\mathbf{q}}$. After a lot of processing and simplifications on $\ddot{\boldsymbol{\beta}}$, the following expression has been found:

$$\ddot{\boldsymbol{\beta}} = g(\beta_1,\beta_2)\boldsymbol{F} + X(\beta_1,\beta_2,\phi,\dot{\beta}_1,\dot{\beta}_2,\omega_y) \tag{6.7}$$

Equation 6.7 shows that for the evolution of the joint angles, the force is only multiplied by a function that only relies on β_1 and β_2. Indicating that the force is in fact related to both the joint angles. Unfortunately, it was not possible within this thesis to investigate further into the relationship of the force and the joint angles.

Before being able to implement this equation, the Lagrangian as in equation 3.40 and the Euler-Lagrange equation in 3.37 have been computed with the use of the Matlab symbolic toolbox (Mathworks). Due to the compliance in the arms of the UAV 2 extra rotation matrices were added into the Lagrangian. Throughout the computation of the Euler-Lagrange equation, these rotation matrices were multiplied and differentiated many times, causing a g in equation 6.7 to consist out of hundreds of trigonometric computations of β_1 and β_2. Due to the fact that this discovery was made near the end of this thesis, it has not been possible to pursue this exploration any further.

6.4 conclusion

This chapter presented the simulation results of both a rigid and a flexible UAV that have been subjected along three different trajectories. A comparison in flight performance is made and flight paths have been evaluated with the initial trajectories. An observability analysis had been performed on the flexible UAV to discuss the relationship between the joint angles and the thrust forces. Through an empirical research a new relationship has been found between the thrust force and the joint angles, which is caused by the dynamics of the UAV.

7 Discussion, Conclusion & Recommendations

7.1 Discussion

In the introduction of this thesis, several research questions have been set to answer during this project. In the phases of modelling, designing, prototyping and simulating a flexing thrust sensor, the answers to most of these questions have been given. This chapter goes over each specific question and elaborates on the acquired results.

Can we relate the strain in strain gauges on a multirotor UAV to the exerted forces?

Due to the fact that the sensor design has been based upon a condition that one side of the sensor is fixed to the ground, the characterization of the sensor is not performed with the conditions of a flying UAV. In the characterization, the relationship between the angle of the deflecting section in the sensor has been related to the applied thrust by the motor and the propeller. This relationship appears to be a linear dependency.

To validate on whether this linearity holds up in a flying UAV, the signals of both the thrust and the joint angles plotted for multiple trajectories. In these simulations, it showed that the linear relationship does not hold for all trajectories. Through the method of empirical research, a relationship between the joint angles and the thrust force has been found that shows that the thrust can only be measured through a computation of both the joint angles.

This shows that the strain that one motor introduces in the system is distributed over both the flexible joints, creating a co-dependency of the thrust forces and the joint angles.

To come back to the research question on whether the strain in the strain gauges on a multirotor can be related to the exerted forces. The answer would be yes, the strain can be related to the thrust force. In section 6.3.1, it is shown that the thrust force can be measured through the sensor with an accuracy of at least 0.5 %. However this is only achieved through experimental work. A start has been made on the prove of this relationship, but more investigation is required to produce concrete proof of this relationship.

What is the minimal resistivity that we need to get a proper measure of the force? And what does this imply for the stiffness requirements of the sensor.

Regarding the minimal resistivity that is needed to get a proper measure of the force, the definition of "proper measurement" should be elaborated. For analog sensors, the quality of a measurement is defined by the SNR of the measurement. In audio applications a rule of thumb is to define a "proper" SNR to be 25 dB. Which implicates that the SNR in voltage of the sensor should be 12.2, meaning that the signal signal output voltage of the sensor is at least 12.2 times bigger than the noise voltage level. From the noise measurement of the sensor in Figure 5.11, the rms power of the noise is -104.8 dB. This implies that the rms voltage output of the sensor should $25 - 104.8 = -79.1$ dB, which is $3.67 \cdot 10^{-4}$V. This voltage is the root-mean-square of the output signal of the sensor. Multiplying this by $\sqrt{2}$, gives the maximum value of a sinusoidal output of the sensor, giving $V_o = \sqrt{2} \cdot 3.67 \cdot 10^{-4} = 4.84 \cdot 10^{-4}$V.

Using equation 5.2, the minimum resistivity can be calculated to have a "proper" measure of the thrust force. Using $V_{EX} = 5$ V and $V_o = 4.84 \cdot 10^{-4}$V, a resistivity of $\Delta R/R = 1.94 \cdot 10^{-4}$ is calculated for the sensor at the peak of a sinusoidal measurement.

In order to translate this to a stiffness, multiple assumptions on the parameters of the sensor design are made:

- The maximum force applied to the sensor is 12 N.
- The dimensions of the strain gauges stay unmodified.
- The length of the flexible section is 19 mm.

- The width b and height d of the flexible section are equal.

This leaves only the width b to be determined.

By combining these assumptions together with equations3.12, 3.3 and 5.1, the following equation is constructed:

$$\frac{\Delta R}{R} = \frac{-3GF\,(3L_s + 8L_c)\,F_{\max}}{4Eb^3} \Rightarrow b = \sqrt[3]{\frac{-3GF(3L_s + 8L_c)F_{\max}}{\Delta R/R \cdot 4E}} \tag{7.1}$$

Filling in all parameters in equation 7.1, a width of $b = 49$ mm is found. Combining this value with the equation for the rotational stiffness in 3.20, leaves a stiffness of $K = 6209$ Nm/rad to be the minimum stiffness requirement for the sensor to have a proper measurement of the thrust force. This assumes that the strain gauge design does not change.

With this minimum flexibility, can we use a controller that neglects this flexibility and be able to control the system?

The minimum flexibility of the sensor (or maximum stiffness) is defined by a stiffness of $K = 6209$ Nm/rad. Comparing this to the actual produced stiffness of $K = 83.9$ Nm/rad, the maximum stiffness is a much higher than the produced sensor. This shows that the produced sensor is much more flexible than the minimum flexibility and as the fabricated sensor design is still controllable by a control system that assumes a rigid system, it is safe to say that a UAV with the minimum amount of flexibility to get a proper force measure is indeed controllable with this same controller.

How does this UAV with flexibility compare to a rigid UAV with regards to flight performance?

When looking at the performance of the flexible UAV compared to a rigid UAV in section 6.2, it can be seen in the plots with the trajectory errors (Figures 6.2, 6.5 and 6.8) that in most trajectories the flexible model performs similar to the rigid model in the trajectory errors in x and z. However, in Figures 6.3, 6.6 and 6.9, the flexible model shows less stable behaviour. Due to the mass-spring-damper systems in the UAV, the controller is struggling more to stabilize the position of the flexible model. This shows up in the force output as an oscillation. Due to the low frequency of ± 2.5 Hz, this oscillation is not caused by the natural frequency of the mass-spring-damper system, but rather by the controller that tries to deal with the delay between the motor position and the center of mass of the UAV.

Overall, the flexible model has a maximum position error in x and z of -0.01 % when compared to the rigid model. When comparing the thrust errors due to the small deflection in the arms, a maximum error of 0.1 % force is applied by the flexible model.

Is there a compromise in flexibility between flight performance and sensor signal?

Regarding the compromise between the sensor signal and the flight performance, it has been shown that there is a range in which the UAV is able to fly and the received sensor signal is good enough for measurements. This range is defined by the stiffness of the sensor. The upper bound of the sensor stiffness is specified by the minimum resistivity requirement of the sensor to achieve a signal-to-noise ratio of at least 25 dB. This maximum stiffness is$K = 6209$ Nm/rad.

The lower bound of this range is defined by the flight performance of the UAV. Meaning that this lower bound is the minimum joint stiffness with which the UAV is still able to fly. In Figure 6.11, the lowest possible stiffness of $K = 0.4$ Nm/rad has been found at which the UAV is still able to perform the manoeuvre of trajectory 3. This simulation assumes that all other parameters in the system of the flexible UAV are unaffected, including the damping factor. Furthermore, a similar simulation has been performed with which only the damping factor has been lowered. This simulation can be found in Figure 6.12, where the lowest damping factor at which the oscillations in the UAV were marginally stable was at $c = 0.18$. This shows that for the lower bound of the compromise between the flight performance and the sensor signal is not only determined by the stiffness of the sensor, but also the damping factor of this system.

7.2 Conclusion

In the current literature, there was very little known on flexibility in multirotor UAVs. This research provides an analysis on the application of a 3D printed thrust sensor for multirotor aerial vehicles which measure the thrust force through the principle of strain and deflection. Two types of multirotor arms have been prototyped which each holds two strain sensors: a cantilever beam design (design 1) and design that consists out of rigid beams with a flexible section (design 2). Both these prototypes have been printed and a characterization of the sensors have been performed with a linear actuator. Due to the limitations of the available printer, only design 2 has been able to be produced at a full scale. The characterization of this sensor has therefore been expanded to measurements with a propeller.

The sensor was able to produce a SNR of 24.6 dB with the linear actuator and a SNR of 32.8 dB with the propeller measurements. Furthermore, the sensor can be modelled as a rotational joint with a stiffness of 83.9 Nm/rad and a damping factor of 0.606. Each arm is modelled as a mass-spring-damper system with a measured natural frequency of 21.3 Hz.

With these properties, a two dimensional model has been made of a rigid and a flexible UAV. Simulations have been performed with a controller that assumes a single rigid body UAV for both the models to observe the performance of a UAV with flexibility in the arms. A maximum position error of -0.01 % for the flexible model has been found when compared to the position of the rigid model. This position error has been found largest for a trajectory what required the UAV to translate in both x and z of the world frame. Due to the small position error between the models, the trajectory error of the models is virtually identical. This shows great promise in the stability of the UAV with the integrated sensor.

For the observability of the thrust force through the joint angles, an empirical research showed that the dynamics of the UAV causes the torque of both thrust forces to contribute to the evolution of each joint angle. This showed that the used Euler-Bernoulli model in chapter 3 does not hold up for aerial vehicles.

7.3 Recommendations

This section will discuss the future work that could be performed as an extension to this assignment. This not only includes further progressions on the already designed sensor and simulation models, but also the sidetracks that have been encountered during the process of this MSc thesis.

7.3.1 Sensor position

For sensor design 2, the position of the sensor on the arm of the UAV is chosen to be exactly in the middle of the arm. This position is merely chosen to be beneficial in terms of production of the sensor. Due to the fact that the sensor was placed in the middle of the beam, the section of the sensor that clamps the carbon fibre rod could be mirrored on the other side. However, the influence of this placement has not been researched in this thesis. When moving the position of the sensor, the distance between the joint and the thrust vector changes. This increases the torque on the sensor, which increases the angular deflection β and eventually increases the strain on the sensor.

A recommendation is to assess the effects of the position of the sensor along the arms of the multirotor UAV. This could also include a study in a placement configuration where the sensors are placed at different positions along each arm of the multirotor.

7.3.2 Hysteresis compensation

In the production of sensor design 2 in section [fab], layers of BVOH were used to increase the similarity between the strain gauges. This has been previously done in (21) to oppress the presence of hysteresis in the produced sensor. Furthermore, a hysteresis compensation method has been designed to predict the hysteric behaviour of the strain gauges. This compensation increases the precision of the designed sensor, as the model of the sensor is more extensive. Figure 7.1 shows an example of this compensation method applied on a linear actuator measurement of sensor design 2. In which a sinusoidal force is applied to the end of the sensor.

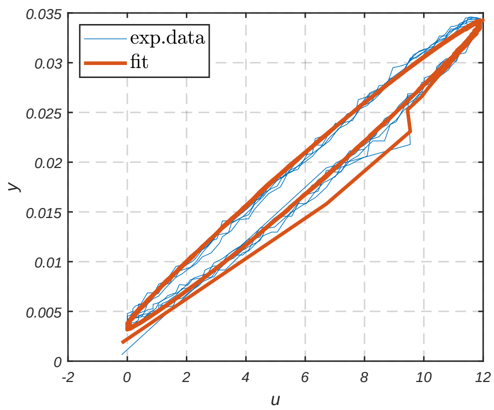

Figure 7.1: Actuated thrust force vs measured voltage with hysteresis estimation.

In Figure 7.1, the blue line is the sensor output and the orange line is the fit from the compensation method. This method uses a modified power law model to create a fitting curve to the training/measurement data. This method shows great promise to be able to produce a 3D printed sensor that can perform accurate measurements. Therefore a recommendation is to apply this method on the existing and future iterations of this sensor design.

As mentioned, to create two identical strain gauges, layers of BVOH (Verbatim) have been added below the bottom strain gauge in the printing process. Another way to ensure this the identicality of the strain gauges is to design the sensor such that the strain gauges are not on the surface of the structure, but rather a few layers deep. This does require a strict monitoring during the printing process to ensure the quality of the strain gauges.

7.3.3 3D UAV model

A further recommendation is to expand the created two dimensional model of the flexible UAV to one that represents a fully actuated multirotor, as the Fibrethex. The current model as created in 3.4.2 is the simplest model to evaluate the flight performance of the UAV. The expansion also includes observing the effects on the sensor of an orientation where the thrust vector has a fixed radial angle, meaning that the thrust vector is not aligned and opposite to the gravitational force.

Bibliography

[Aerial-CORE] Aerial-CORE (), Aarial-core.
https://aerial-core.eu/

[2] Albers, A., S. Trautmann, T. Howard, Trong Anh Nguyen, M. Frietsch and C. Sauter (2010), Semi-autonomous flying robot for physical interaction with environment, in *2010 IEEE Conference on Robotics, Automation and Mechatronics*, IEEE, , Singapore, pp. 441–446, ISBN 978-1-4244-6503-3, doi:10.1109/RAMECH.2010.5513152.
http://ieeexplore.ieee.org/document/5513152/

[Ardiuno] Ardiuno (), Arduino Uno Rev3.
http://store.arduino.cc/products/arduino-uno-rev3

[ATI] ATI (), ATI Industrial Automation: F/T Sensor mini40.
https://www.ati-ia.com/products/ft/ft_models.aspx?id=mini40

[5] Baumgart, F. (2000), Stiffness — an unknown world of mechanical science?, *Injury*, **vol. 31**, pp. 14–84, ISSN 00201383, doi:10.1016/S0020-1383(00)80040-6.
https:
//linkinghub.elsevier.com/retrieve/pii/S0020138300800406

[6] Beer, F. P. (Ed.) (2013), *Vector mechanics for engineers. Statics and dynamics*, McGraw-Hill, New York, 10th ed edition, ISBN 978-0-07-339813-6.

[7] Bernoulli (2021), Euler–Bernoulli beam theory, page Version ID: 1055704452.
https://en.wikipedia.org/w/index.php?title=Euler%E2%80%93Bernoulli_beam_theory&oldid=1055704452

[Brown] Brown (), Dynamics and Vibrations: Notes: Free Damped Vibrations.
https://www.brown.edu/Departments/Engineering/Courses/En4/Notes/vibrations_free_damped/vibrations_free_damped.htm

[9] Cummings (2006), *Understanding Physics*, Wiley India Pvt. Limited, ISBN 978-81-265-0882-2, google-Books-ID: rAfF_X9cE0EC.

[10] Davis, E. and P. Pounds (2016), Direct Thrust and Velocity Measurement for a Micro UAV Rotor., p. 8.

[Diabase] Diabase (), Desktop CNC Machines | Diabase Engineering | Longmont.
https://www.diabasemachines.com

[DJI] DJI (), DJI - Official Website.
https://www.dji.com/nl

[13] Ekelof, S. (2001), The genesis of the Wheatstone bridge, **vol. 10**, no.1, pp. 37–40, ISSN 0963-7346, doi:10.1049/esej:20010106.
https://digital-library.theiet.org/content/journals/10.1049/esej_20010106

[14] Fox, C. (1987), *An introduction to the calculus of variations*, Dover Publications, New York, ISBN 978-0-486-65499-7.

[15] Franchi, A., R. Carli, D. Bicego and M. Ryll (2018), Full-Pose Tracking Control for Aerial Robotic Systems With Laterally Bounded Input Force, **vol. 34**, no.2, pp. 534–541, ISSN 1941-0468, doi:10.1109/TRO.2017.2786734, conference Name: IEEE Transactions on Robotics.

[16] Gere, J. M. and S. Timoshenko (1991), *Mechanics of materials*, ISBN 978-1-4899-3124-5, oCLC: 883381340.

[17] Hamandi, M., F. Usai, Q. Sablé, N. Staub, M. Tognon and A. Franchi (2021), Design of multirotor aerial vehicles: A taxonomy based on input allocation, **vol. 40**, no.8-9, pp.

1015–1044, ISSN 0278-3649, doi:10.1177/02783649211025998, publisher: SAGE Publications Ltd STM.
https://doi.org/10.1177/02783649211025998

[18] Instruments, N. (1998), Strain Gauge Measurement – A Tutorial.

[19] Jovanović, M., A. Simonovic, N. Lukić, N. Zorić, S. Stupar and S. Ilić (2014), EXPERIMENTAL DETERMINATION OF ACTIVE STRUCTURE DAMPING RATIO USING DIFFERENT CONTROL STRATEGIES IN SYSTEM OF ACTIVE VIBRATION CONTROL.

[Keithley] Keithley (), Keithley Instruments & Products | Tektronix.
https://www.tek.com/en/products/keithley

[21] Kosmas, D., M. Schouten and G. Krijnen (2020), Hysteresis Compensation of 3D Printed Sensors by a Power Law Model with Reduced Parameters, in *2020 IEEE International Conference on Flexible and Printable Sensors and Systems (FLEPS)*, IEEE, Manchester, United Kingdom, pp. 1–4, ISBN 978-1-72815-278-3, doi:10.1109/FLEPS49123.2020.9239580.
https://ieeexplore.ieee.org/document/9239580/

[22] Lagrange, J. L. (1811), *Mécanique analytique*, Ve Courcier, google-Books-ID: Q8MKAAAAYAAJ.

[Mathworks] Mathworks (), MATLAB - MathWorks.
https://www.mathworks.com/products/matlab.html

[Mathworks] Mathworks (), Simulink - Simulation and Model-Based Design.
https://www.mathworks.com/products/simulink.html

[Mathworks] Mathworks (), Symbolic Math Toolbox.
https://www.mathworks.com/products/symbolic.html

[26] McArthur, D. R., A. B. Chowdhury and D. J. Cappelleri (2017), Design of the I-BoomCopter UAV for environmental interaction, in *2017 IEEE International Conference on Robotics and Automation (ICRA)*, pp. 5209–5214, doi:10.1109/ICRA.2017.7989611.

[27] Menezes, R. (2019), Embedded thrust estimator design of a brush-less direct current motor used in multi-rotor., *Robotics and Mechatronics*, p. 68.

[MGChemicals] MGChemicals (), Silver Conductive Epoxy.
https://www.mgchemicals.com/products/adhesives/electrically-conductive-adhesives/silver-conductive-epoxy/

[29] Ollero, A., J. Cortes, A. Santamaria-Navarro, M. A. Trujillo Soto, R. Balachandran, J. Andrade-Cetto, A. Rodriguez, G. Heredia, A. Franchi, G. Antonelli, K. Kondak, A. Sanfeliu, A. Viguria, J. R. Martinez-de Dios and F. Pierri (2018), The AEROARMS Project: Aerial Robots with Advanced Manipulation Capabilities for Inspection and Maintenance, **vol. 25**, no.4, pp. 12–23, ISSN 1070-9932, 1558-223X, doi:10.1109/MRA.2018.2852789.
https://ieeexplore.ieee.org/document/8435987/

[Openrobots] Openrobots (), Overview - tk3-mikrokopter - Openrobots.
https://git.openrobots.org/projects/tk3-mikrokopter

[proto pasta] proto pasta (), Back-to-basics White PLA.
https://www.proto-pasta.com/products/back-to-basics-white-4043d-pla

[Proto-pasta] Proto-pasta (), Electrically Conductive Composite PLA.
https://www.proto-pasta.com/products/conductive-pla

[Prusa] Prusa, J. (), Original Prusa i3 MK3S+ | Original Prusa 3D printers directly from Josef Prusa.
https://www.prusa3d.com/category/original-prusa-i3-mk3s/?gclid=CjwKCAiA6Y2QBhAtEiwAGHybPce9a7pQO_

iwEcVDKTPwI8eNe9ELHgbCNTZsF1E4GFd4z08QYeithBoC9VYQAvD_BwE

[RaM] RaM (), Robotics and Mechatronics.
https://www.ram.eemcs.utwente.nl/

[35] Serway, R. A. and J. W. Jewett (2004), *Physics for scientists and engineers*, Thomson-Brooks/Cole, Belmont, CA, 6th ed edition, ISBN 978-0-534-40842-8.

[Shenoy] Shenoy, N. (), Design, fabrication and evaluation of a 3D printed thrust sensor for application in drones, *Robotics and Mechatronics*, p. 99.

[37] Siciliano, B. (Ed.) (2009), *Robotics: modelling, planning and control*, Advanced textbooks in control and signal processing, Springer, London, ISBN 978-1-84628-641-4 978-1-84628-642-1, oCLC: ocn144222188.

[SMAC] SMAC (), SMAC Corporation.
https://www.smac-mca.com/

[Solidworks] Solidworks (), 3D CAD Design Software | SOLIDWORKS.
https://www.solidworks.com/home-page-2021

[40] Steidel, R. F. (1989), *An introduction to mechanical vibrations*, Wiley, New York, 3rd ed edition, ISBN 978-0-471-84545-4.

[41] Suarez, A., G. Heredia and A. Ollero (2018), Physical-Virtual Impedance Control in Ultralightweight and Compliant Dual-Arm Aerial Manipulators, **vol. 3**, no.3, pp. 2553–2560, ISSN 2377-3766, 2377-3774, doi:10.1109/LRA.2018.2809964.
https://ieeexplore.ieee.org/document/8302932/

[42] Suarez, A., A. E. Jimenez-Cano, V. M. Vega, G. Heredia, A. Rodriguez-Castaño and A. Ollero (2017), Lightweight and human-size dual arm aerial manipulator, in *2017 International Conference on Unmanned Aircraft Systems (ICUAS)*, pp. 1778–1784, doi:10.1109/ICUAS.2017.7991357.

[43] Tognon, M. and A. Franchi (2017), Dynamics, Control, and Estimation for Aerial Robots Tethered by Cables or Bars, **vol. 33**, no.4, pp. 834–845, ISSN 1552-3098, 1941-0468, doi:10.1109/TRO.2017.2677915, arXiv: 1603.07567.
http://arxiv.org/abs/1603.07567

[44] Tognon, M. and A. Franchi (2018), Omnidirectional Aerial Vehicles With Unidirectional Thrusters: Theory, Optimal Design, and Control, **vol. 3**, no.3, pp. 2277–2282, ISSN 2377-3766, 2377-3774, doi:10.1109/LRA.2018.2802544.
http://ieeexplore.ieee.org/document/8281444/

[45] Tsai, L.-W. (1999), *Robot analysis: the mechanics of serial and parallel manipulators*, Wiley, New York, ISBN 978-0-471-32593-2.

[Ubuntu] Ubuntu (), Ubuntu PC Besturingsysteem.
http://ubuntu.nl/

[UTwente] UTwente (), Universiteit Twente (UT) | Enschede | High Tech Human Touch.
https://www.utwente.nl/

[Verbatim] Verbatim (), BVOH-filament van Verbatim 1,75 mm - Natuurlijk | Verbatim Online Sho, section: Verbatim BVOH filament 1.75mm.
https://www.verbatim-europe.nl/nl/prod/verbatim-bvoh-filament-175-mm--transparent-55903/